

UC Davis

UC Davis Electronic Theses and Dissertations

Title

Quantification and Computation in Long Axial Field of View Positron Emission Tomography

Permalink

<https://escholarship.org/uc/item/19v3b9hf>

Author

Leung, Edwin

Publication Date

2021

Peer reviewed|Thesis/dissertation

Quantification and Computation in Long Axial Field of View Positron Emission Tomography

By

EDWIN KIN SAN LEUNG

DISSERTATION

Submitted in partial satisfaction of the requirements for the degree of

DOCTOR OF PHILOSOPHY

in

Biomedical Engineering

in the

OFFICE OF GRADUATE STUDIES

of the

UNIVERSITY OF CALIFORNIA

DAVIS

Approved:

Ramsey D. Badawi, Chair

Simon R. Cherry

Jinyi Qi

Cameron C. Foster

Committee in Charge

2021

Abstract

The emergence of long axial field-of-view (FOV) total-body positron emission tomography (PET) systems has enabled a broad range of new applications previously not feasible due to the limited axial coverage. The 40-fold increase in system sensitivity across the entire adult human (compared to shorter, conventional PET systems) of the 194 cm long EXPLORER total-body PET scanner has enabled 1) reduction of scan time, 2) reduction of radiation dose, 3) improved dynamic range of radiotracer, 4) improved image quality, 5) system-level kinetic modeling of the human body, and more. However, the technical challenges stemmed from total-body PET systems are not thoroughly investigated. The global quantification of radioactivity in humans is not well studied since prior PET systems did not possess the necessary axial coverage to encompass the entire living human. The absolute quantification of regional tissue radioactivity concentration is a critical parameter of interest across various clinical and research applications and can be affected by a complex interplay of factors including scanner calibration, data correction, and image reconstruction. The increase in axial acceptance angle offered by total-body PET systems, while improves system sensitivity, can also make scatter correction more challenging. In addition, the high data rates caused by the large axial extent of the system impose significant computational and data storage burdens on the supporting infrastructure.

The goal of this work is to establish the quantitative performance baseline for long axial FOV PET systems using the EXPLORER total-body PET scanner, as well as to develop a computational foundation to address the high data rates imposed by such systems as well as its derivatives. To that end, we comprehensively assessed the quantitative accuracy of the EXPLORER scanner using a wide variety of phantoms as well as in healthy humans. Our results overall indicated that the quantitative performance achieved with the EXPLORER scanner was uniform across the axial FOV and provided the accuracy necessary to support a wide range of imaging applications spanning from low-dose studies to dynamic imaging with commonly used image reconstruction frame lengths.

Next, we investigated the relationship between ^{18}F -fluorodeoxyglucose (^{18}F -FDG) image signal-to-noise ratio (SNR) and noise-equivalent count rate (NECR) in total-body PET using the EXPLORER scanner. To estimate the complex scatter distributions observed in total-body PET systems, we developed a Monte Carlo scatter correction framework for total-body PET that utilizes continuous water

density materials as the attenuation input. We discovered that the use of time-of-flight NECR (TOF-NECR) as a count rate performance metric over conventional non-TOF NECR at radioactivity levels beyond peak non-TOF NECR may be more suitable for assessing the count rate performance of PET systems with TOF capabilities.

To address the massive single event data rates imposed by total-body PET systems, we developed a high-performance, software-based coincidence processor capable of processing EXPLORER list-mode single event data in near real-time using several computational nodes.

Finally, we developed a simulation framework and performed a scanner sensitivity study of the NeuroEXPLORER (NX) scanner, the next-generation dedicated brain PET/CT scanner. The simulation results showed that the increase in solid angle coverage of the NX scanner over both the HRRT-D and Biograph Vision scanners can lead to approximately a 2-fold increase in peak system sensitivity, as well as an approximate 5-fold increase in total system sensitivity.

Overall, this work took a first dive into tackling new questions in total-body PET that were not examined in detail previously and established the quantitative and computational foundations for future total-body PET research and its derivatives requiring quantitatively accurate and high-throughput capabilities.

Acknowledgements

To start, I would like to quote a sentence from the thesis of my advisor, Dr. Ramsey Badawi:

*“A scientific PhD thesis may appear to be the work of one person, but in fact it represents the efforts of a whole **team**, and there are **many** key players without whom the thesis could not be produced.”*

I thank Dr. Ramsey Badawi and Dr. Simon Cherry for the opportunity to be involved in a once-in-a-lifetime project and their mentorship. I also thank Dr. Jinyi Qi, Dr. Cameron Foster, and Dr. Abhijit Chaudhari for serving on my dissertation and/or qualifying exam committees. It goes without saying that I am grateful for all five of them for their faith in me in completing this work.

I thank my co-authors for their engagement and guidance during this extensive PhD journey. All of this would not have been possible without their patience and support.

In addition, I thank our academic and industry collaborators at Yale University and United Imaging Healthcare for their part in massively elevating the importance of this work.

I also thank the former and current EMIC, MIPET, Radiology, and BME folks for their continuous support in making this work possible.

Last but most certainly not least, I thank my friends and family for their love and constant encouragement that I can finish this work.

To future students – I hope you find this dissertation helpful, and I wish you an incredible journey :)

This work was supported by NIH R01 CA170874, R01 CA206187, R01 CA249422, and the UC Davis Research Investment in Science and Engineering Program.

Contents

Abstract	ii
Acknowledgements	iv
Contents	v
List of Figures	viii
List of Tables	xi
Chapter 1 – Background and Significance	1
Fundamentals of Positron Emission Tomography (PET).....	1
The basic physics of PET	2
Positron emission and annihilation	2
Positron range.....	3
Non-collinearity	3
Annihilation photon interactions with matter	3
PET detectors	5
Scintillator	5
Photodetector.....	6
Readout electronics	7
Block detector	7
Coincidence event generation	8
Energy window.....	9
Time window	9
Geometric window	10
Coincidence policy.....	10
Coincidence event types.....	11
PET data representation.....	14
List-mode	14
Sinogram.....	14
Michelogram	15
Single-slice re-binning (SSRB)	16
PET data corrections	17
Normalization	17
Attenuation Correction	18
Dead-time correction.....	19
Randoms Correction	20
Scatter correction.....	21
Decay correction	23
Dose calibration	23
PET image reconstructions	23
Monte Carlo PET simulations	24
Modern PET technologies	25
Time-of-flight (TOF) PET	25
Depth-of-interaction (DOI) PET	26
Performance and quantification in PET	27
Spatial resolution	28
Count rate performance.....	28
Sensitivity.....	29
Quantitative accuracy and image quality.....	29
Time-of-flight resolution	30
PET/CT co-registration accuracy.....	30
Energy resolution	30
Applications in PET	30
Biology of ¹⁸ F-FDG.....	31
Dynamic PET imaging	32
Limits on conventional PET imaging	33

Emergence of total-body PET	34
Current challenges in total-body PET imaging	35
Project aims	35
Chapter 2 – Quantitative accuracy in total-body PET using the EXPLORER PET/CT scanner	37
Introduction	37
Methods	39
System parameters	39
Image reconstruction	40
Accuracy of count rate corrections	41
Uniform phantom	41
Regional bias and variability	42
Dynamic quantification in humans	43
Results	44
Count rate dependent quantitative accuracy	44
Uniform phantom	45
Triple NEMA IQ phantom	47
Human subjects	48
Discussion	49
Conclusion	52
Chapter 3 – Relating ¹⁸F-FDG image signal-to-noise ratio to time-of-flight noise-equivalent count rate in total-body PET using the EXPLORER scanner	54
Introduction	54
Methods	56
Derivation of NEC expressions for list-mode coincidence data	56
System parameters	57
Uniform phantom	58
Human subjects	58
Data processing	59
Image reconstruction	60
Results	60
Uniform phantom	60
Human subjects	61
Discussion	64
Conclusion	67
Acknowledgement	68
Appendix	68
Chapter 4 – Development and performance evaluation of a high-performance, software-based coincidence processor for total-body PET	78
Introduction	78
Methods	80
Computational requirements	80
Data compression and format	81
Design of the software-based coincidence processor	84
Test data	90
Coincidence processing performance evaluation	91
Storage type	92
Overall performance	92
Results	93
Poisson validation	93
Storage type	94
Number of files	95
Discussion	96
Conclusion	99
Chapter 5 – Monte Carlo sensitivity study of the NeuroEXPLORER dedicated brain PET scanner	100
Introduction	100

Methods	100
Simulation software and data processing	100
Scanner geometries	101
Digitizer parameters	104
Sensitivity	104
Line source sensitivity	105
Point source sensitivity	105
Uniform brain sensitivity	105
Results	106
Line source sensitivity	106
Point source sensitivity	107
Uniform brain sensitivity	108
Discussion	109
Conclusion	110
Chapter 6 – Conclusion and future work	111
Summary and next steps	111
The practical future of total-body PET	115
References	118

List of Figures

Figure 1-1. Positron range and non-collinearity effects from a positron emission.....	2
Figure 1-2. A visual example of a coincidence processor, shown with four total energy-qualified singles in the time window (in 2-D, 3-D views and time domains, respectively). (a) Three potential coincidences (coincidence pairs 1-2, 1-3 and 1-4) in the primary, fixed time window (τ_{fixed}). (b) Coincidence pair 1-2 is rejected by the geometric window. (c) Coincidence pair 1-3 is rejected by the variable time window (τ_{13}), while coincidence pair 1-4 is accepted by the variable time window (τ_{14}). Note: the asterisk (*) denotes the reference single event. Also, coincidence pairs 2-3 and 2-4 are not considered in the time window opened by 1 (τ_{fixed}) but will be considered in the time window opened by 2.....	11
Figure 1-3. Types of coincidence events. Red lines indicate incorrectly assigned LORs.	13
Figure 1-4. Types of scattered coincidence events. S_{xy} denotes the number of times each of the 2 annihilation photons scattered.	13
Figure 1-5. (Left) A projection profile of an image at angle ϕ . (Right) A sinogram.....	15
Figure 1-6. Relationship between an LOR and a Michelogram (portrayed as a 4-D sinogram).....	16
Figure 1-7. Determining the location of the annihilation event along the LOR (in green). (Left) ground truth. (Center) Without TOF information, where every bin along the LOR is given equal weights. (Right) With TOF information, where the bins closer to the annihilation event is given heavier weights.	26
Figure 1-8. DOI effects on event localization. (Left) Ground truth, where the location of energy depositions in both scintillator crystals are known. (Center) Without DOI, where the width of the LOR is large. (Right) With DOI, where the width of LOR is small due to improved localization of energy deposition in both scintillator crystals.	27
Figure 1-9. (Left) A glucose molecule. (Right). An ^{18}F -fluorodeoxyglucose molecule.	31
Figure 1-10. A 3-compartment model of ^{18}F -FDG.	32
Figure 2-1. Range of count rates encountered by the EXPLORER scanner (throughout the PET acquisition) in various clinical and research tasks. The count rates were estimated based on the NEMA NU 2-2018 NECR performance assessment using an extended, 175 cm NU 2 scatter phantom. Note: the activity at peak NECR is 528 MBq, and “p.i.” stands for post-injection.	39
Figure 2-2. The position and activity of each phantom in the triple NEMA IQ phantom assessment.....	43
Figure 2-3. The relative true error of the standard 70 cm NU 2 scatter phantom.	44
Figure 2-4. The relative true error of the extended 175 cm NU 2 scatter phantom. The shaded blue region represents the average activity throughout an clinical ^{18}F -FDG scan (~300 MBq injected; scan begins at 120-min post-injection).	45
Figure 2-5. Axial uniformity of the EXPLORER scanner. (Left) The y-axis ranged from 0 to 1.1. (Right) The y-axis ranged from 0.92 to 1.08. The normalization factor was based on the ROI average of the central 90% slices.	46
Figure 2-6. The global activity bias of the uniform phantom. The shaded blue region corresponds to the average activity throughout an EXPLORER clinical ^{18}F -FDG scan (~300 MBq injected; scan begins at 120-min post-injection).	46
Figure 2-7. Bias (mean \pm SD) of the background ROIs in the 3 IQ phantoms. The error bars indicate the standard deviation (SD) of the mean bias of the 324 background ROIs analyzed for each IQ phantom. The blue shaded region represents the average activity throughout an EXPLORER clinical ^{18}F -FDG scan (~300 MBq injected; scan begins at 120-min post-injection).	47
Figure 2-8. VOI biases of the (left) 37 mm hot sphere and (right) background of the 3 rd IQ phantom. Each label on the x-axis represents the acquisition time point and the average frame duration of the re-sampled dataset, ordered based on the fraction of total counts of the 1 st 30-min scan (as shown on the upper x-axis). Mean VOI biases are shown for all datasets using black asterisks. In the case of shorter time-frame re-sampled datasets, the mean was calculated on the 30 re-sampled dataset images, and box plots were included to show the variations among the 30 datasets.	48
Figure 2-9. Activity bias of the (top) human subjects, and (bottom) uniform phantom using the 66-frame reconstruction framing protocol. The vertical dashed lines correspond to the time points where the frame duration changed.	49
Figure 2-10. Activity bias of 14 human subjects using the 66-frame reconstruction framing protocol. The injected ^{18}F -FDG activity ranged from 337 – 397 MBq.	52
Figure 3-1. The non-TOF NECR and TOF-NECR of the uniform phantom.	61

Figure 3-2. The image SNR ² of the uniform phantom, plotted against (left) non-TOF NECR, and (right) TOF-NECR.....	61
Figure 3-3. The non-TOF NECR and TOF-NECR of human subjects, plotted against (top) activity concentration, and (bottom) activity.....	62
Figure 3-4. The adjusted SNR ² of the human subjects, plotted against (top) non-TOF NECR, and (bottom) TOF-NECR. A linear fit was performed on each human subject, and the mean R ² values for SNR ² vs. non-TOF NECR and TOF-NECR of all 14 human subjects were 0.98 (min: 0.91) and 0.98 (min: 0.94), respectively.....	63
Figure 3-5. The SNR ² of the human subjects, plotted against (top) non-TOF NECR, and (bottom) TOF-NECR. A linear fit was performed on each human subject, and the mean R ² values for SNR ² vs. non-TOF NECR and TOF-NECR of all 14 human subjects were 0.97 (min: 0.90) and 0.98 (min: 0.94), respectively.....	64
Figure 3-6. The optimal (left) activity concentration, and (right) activity vs. BMI when TOF-NECR = 3000 kcps for the 14 human subjects.....	67
Figure 3-7. HU probability distribution in the CT image volume of a healthy adult human subject.....	69
Figure 3-8. A general overview of converting a CT image into a SimSET material index map.....	70
Figure 3-9. The linear attenuation coefficient vs. photon energy plots for the (Left) SimSET brain material, and (Right) SimSET bone material, with respective fitted water density materials. The region highlighted in green shows the energy range between the LLD of the EXPLORER scanner (430 keV) and 511 keV.....	71
Figure 3-10. (Left) A 3-D rendering of the 3 x 3 grid phantom. (Right) The 3 x 3 grid phantom.....	72
Figure 3-11. (Left) The 3 x 3 grid phantom, surrounded by wax blocks. (Right) A schematic representation of the 3 x 3 grid phantom, where only the corners of the grid are filled with ¹⁸ F-FDG.....	73
Figure 3-12. (Top) A cross-sectional representation of the 3 x 3 grid phantom. (Bottom) A representative PET projection of the 3 x 3 grid phantom, assuming perfect PET data corrections.....	74
Figure 3-13. Count and scatter fraction biases of individual organs between the default SimSET materials and the continuous water density materials. Data courtesy of Dr. Zhaoheng Xie and Dr. Xuezhu Zhang.....	75
Figure 3-14. Scatter fitting (w/o surrounding wax) in the projection space, in the detector block level.....	76
Figure 3-15. Scatter fitting (w/ surrounding wax) in the projection space. (Left) Scatter fitting in the detector block level. (Right) Scatter fitting in the detector crystal level.....	76
Figure 3-16. Fitted smooth step functions in the detector crystal level using projection data from the 3 x 3 grid phantom (w/ surrounding wax), with a mean <i>c</i> value of 1.3584 (range: 1.1324 – 1.6895).....	77
Figure 4-1. A representation of data compression. X and Y represents bit values for a given parameter in an event, and 0 represents zero-padding. Here, data compression resulted in a 50% size reduction, from 16 bits (2 bytes) to 8 bits (1 byte).....	81
Figure 4-2. Bit assignments for a coarse timestamp (Judenhofer 2018). The bit resolution of the time value is 20 μs.....	82
Figure 4-3. Bit assignments for a single event (Judenhofer 2018).....	82
Figure 4-4. Bit assignments for a coincidence event (Judenhofer 2018).....	83
Figure 4-5. Design overview of the coincidence processor.....	84
Figure 4-6. Command-line example of the coincidence processor.....	86
Figure 4-7. Example of a coincidence processor configuration file.....	87
Figure 4-8. Pseudocode implementation of the coincidence processing algorithm.....	88
Figure 4-9. Reduced χ^2 statistics of various types of coincidences from the Biograph mCT-like simulations.....	93
Figure 4-10. Ratios of multiple coincidences in the prompt and delayed coincidences from the Biograph mCT-like simulations.....	93
Figure 4-11. Overall coincidence processing performance of the coincidence processor using increasing number of CPU threads while processing a single file. The average coefficient of variation (CV) of the data points, calculated over 10 repetitions, was 2.0%. Data points above the real-time threshold reflect data rates that can be processed at near real-time with 1 computer node.....	94
Figure 4-12. Coincidence processing performance of the coincidence processor with increasing number of files. The average coefficient of variation (CV) of the data points, calculated over 10 repetitions, was 3.2%. Data points above the real-time threshold reflect data rates that can be processed at near real-time with one computer node.....	96
Figure 4-13. Number of computer nodes needed to achieve near real-time coincidence processing.....	98

Figure 4-14. Singles-to-qualified singles, qualified singles-to-prompt, and prompt-to-multiples ratios of the test data.....	99
Figure 5-1. (Left) Illustration of the NX scanner. Image courtesy of Dr. Hongdi Li (UIH America). (Right) Geometry of the NX scanner (shoulder cutouts not included).....	101
Figure 5-2. Geometry of the (Top Left) Mini EXPLORER II, (Top Right) HRRT-D, (Bottom Left) Biograph Vision, and (Bottom Right) CareMiBrain scanners, respectively.	102
Figure 5-3. A representation of the uniform brain simulation setup.	106
Figure 5-4. NEMA NU 2-2018 sensitivity of various scanners.....	107
Figure 5-5. Point source sensitivity of various scanners.....	108
Figure 5-6. Uniform brain sensitivity of various scanners.	109

List of Tables

Table 1-1. Common scintillator materials used in PET detectors (Melcher 2000, Kemp 2006, Nassalski 2007, Cherry 2012).	5
Table 3-1. Details of the healthy human subjects (n=14).	59
Table 3-2. X-ray tube kVp-dependent values used for generating the 511-keV attenuation map (Carney 2006).	70
Table 3-3. SimSET simulation parameters for the XCAT phantom.	71
Table 3-4. Reconstruction parameters for the XCAT phantom.	72
Table 3-5. Specifications of the 3 x 3 grid phantom.	73
Table 3-6. Global event statistics of the SimSET output. Data courtesy of Dr. Zhaoheng Xie and Dr. Xuezhu Zhang.	74
Table 3-7. Mean ROI statistics of the brain and the liver between the materials. Data courtesy of Dr. Zhaoheng Xie and Dr. Xuezhu Zhang.	75
Table 4-1. Example of coincidence policies. A coincidence policy comprises of 1) a window type, and 2) a multiple coincidence event policy (i.e. multiples policy).	79
Table 4-2. Estimated size of list-mode singles data produced by the EXPLORER scanner.	80
Table 4-3. A representation of timestamps in an EXPLORER list-mode singles file. Here, a fine time resolution of 80 ps was used instead of the actual 78.125 ps for ease of demonstration.	83
Table 4-4. A representation of the reserve buffer in the coincidence processor. The green boxes represent single events in the reserve buffer. Note: events in the reserve buffer are not treated as reference single events.	89
Table 4-5. Compilation environment and major functions used for the coincidence processor.	89
Table 4-6. Simulation parameters for the Poisson validation protocol for a Biograph mCT-like scanner geometry.	90
Table 4-7. Simulation parameters of the test data. Note: the parameters were defined based on the expected EXPLORER scanner specifications and are not identical to the actual EXPLORER scanner specifications.	91
Table 4-8. Parameters used for the coincidence processor. Note: the parameters were defined based on the expected EXPLORER coincidence processor specifications and are not identical to the actual EXPLORER coincidence processor specifications.	91
Table 5-1. Specifications of the simulated PET scanners.	103

Chapter 1 – Background and Significance

Fundamentals of Positron Emission Tomography (PET)

PET is an *in vivo*, quantitative tomographic imaging technique that provides spatial and temporal distributions of a positron-emitting radiotracer, which reflects the underlying biochemical and physiological conditions in a living human. The working principle of PET is based on the detection of annihilation photon pairs originated from the subject of interest using radiation detectors commonly assembled in a cylindrical configuration that surrounds a portion of the subject. A typical PET scan involves injecting trace amounts of compounds labeled with a positron-emitting radioisotope into the subject of interest. During this process, the radiotracer accumulates in the relevant biological tissues. After some amount of wait time (typically in the order of 1 h depending on the task and radiotracer injected), the subject is positioned inside the scanner. Coincidence events arising from pairs of annihilation photons emitted from the subject are then detected, and the data, along with any corrections applied, are used to reconstruct a tomographic (3-dimensional) image volume using mathematical algorithms. The resulting image volume contains an estimation of the radiotracer distribution and concentration, which may be useful for diagnostic purposes (such as lesion detection) as well as for studying specific biological processes (such as brain glucose metabolism). PET is currently the most sensitive molecular imaging technique capable of detecting picomolar concentration levels in the body, thereby allowing the injection of radiotracer with minimal pharmacologic or toxicologic effects which may otherwise perturb the biological system ([Cherry 2012](#)).

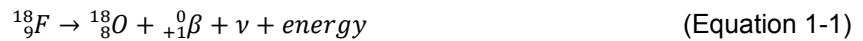
In this chapter, the complete workflow to generate a PET image, from the physical principles of PET to the data generation and processing, as well as PET data correction, image reconstruction, and computer simulations, is summarized. Next, the modern PET technologies and the methods to characterize the performance of a PET scanner are described. Then, the clinical and research PET applications, as well as the limitations of conventional PET scanners, are mentioned. Furthermore, the concept of total-body PET scanners, a long axial field-of-view (FOV) PET scanner that encloses the entire adult human is discussed, along with its advantages and challenges. Finally, the aims of this work are presented.

The basic physics of PET

Positron emission and annihilation

PET is based on the physical mechanisms of positron emission, where an unstable isotope undergoes radioactive decay, which transforms a proton into a neutron and a positron (i.e. a positively charged electron). During the process, the positron, along with a neutrino, and energy are emitted from the nucleus. An example of ^{18}F decay by positron emission is shown in $^{18}\text{F} \rightarrow ^{18}\text{O} + ^0_{+1}\beta + \nu + \text{energy}$

(Equation 1-1:



The net energy released during positron emission is shared between the positron, the neutrino, and the recoiling daughter nucleus. As the positron loses most of its kinetic energy during inelastic collisions with electrons in the surrounding medium through a tortuous path, it combines with an electron and forms a positronium (an unstable quasi-particle formed by the electron-positron pair). The positronium then annihilates into a pair of photons traveling in opposite directions, carrying a total energy equal to the rest masses of the positron and electron, at 511 keV each. Figure 1-1 demonstrates the effects of positron range and non-collinearity which is summarized below.

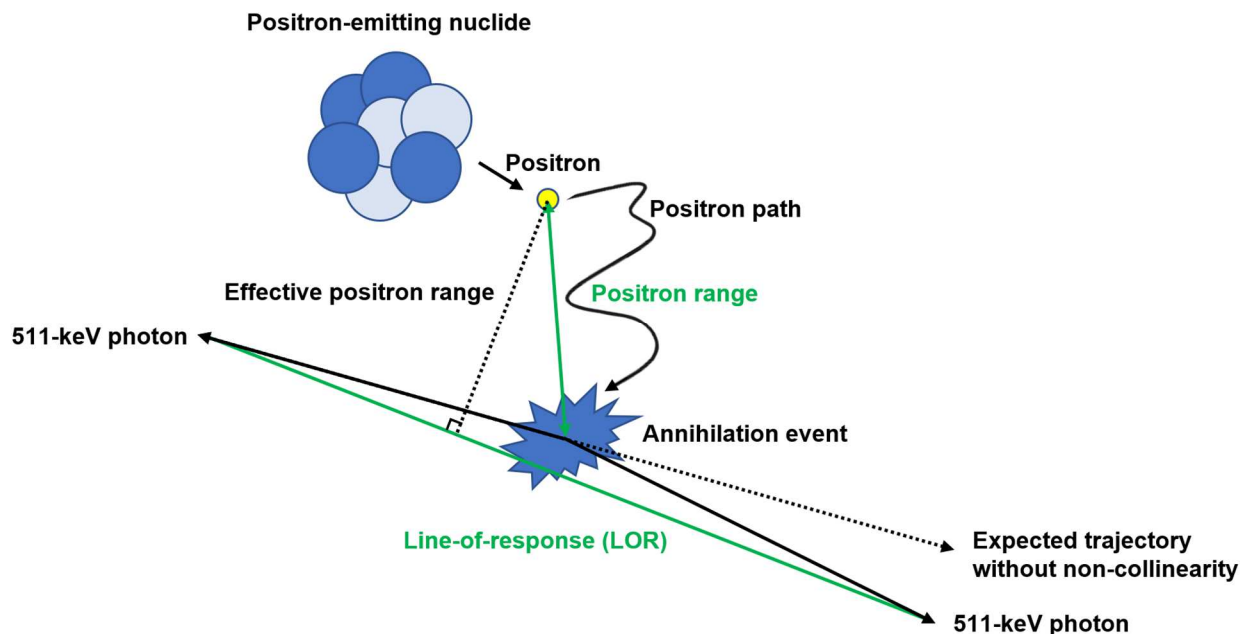


Figure 1-1. Positron range and non-collinearity effects from a positron emission.

Positron range

The displacement between the positron-emitting nucleus and the site of positron annihilation is known as the positron range and is dependent on the kinetic energy of the emitted positron. Also, the maximum kinetic energy of the positron is specific to the radionuclide. Positron range results in the spatial blurring of the PET images due to the perpendicular offset between the line-of-response (LOR) and the site of positron emission (known as the effective positron range), which imparts a fundamental limit on the finest achievable spatial resolution in PET.

Non-collinearity

Residual kinetic energies that remain in the positron and electron during the annihilation process lead to non-collinearity, meaning the photon pair travels at a slightly different angle than 180°. Non-collinearity results in the spatial blurring of PET images due to misassigned LORs. The magnitude of the spatial blurring (Δ_{nc}) due to non-collinearity is estimated using $\Delta_{nc} = 0.0022 \times D$

(Equation 1-2 ([Cherry 2006](#)):

$$\Delta_{nc} = 0.0022 \times D \quad \text{(Equation 1-2)}$$

where D is the ring diameter of the PET scanner.

Annihilation photon interactions with matter

In PET, the primary mechanisms of interest for 511-keV photons to interact with matter (that is, the scan subject and PET detectors) are 1) photoelectric absorption and 2) Compton scattering. Photoelectric absorption occurs when a photon deposits all its energy in a surrounding atom, ejecting a photoelectron in the process. When photoelectric absorption takes place inside the subject, it results in the loss of a true coincidence event since one of the two annihilation photons will not be detected by the PET detectors. At 511-keV, the probability of photoelectric absorption is negligible compared to Compton scattering in the human body.

Compton scattering occurs when a photon partially deposits its energy in an atom, ejecting a recoil electron and changes its direction in the process. Compton scattering is the predominant mechanism in PET that leads to scattered coincidences which causes mispositioning of LORs. The

energy of the scattered photon (E_{sc}) is calculated using $E_{sc} = \frac{E_0}{1 + (\frac{E_0}{m_0c^2})(1 - \cos\theta)}$

(Equation 1-3 (Cherry 2012):

$$E_{sc} = \frac{E_0}{1 + (\frac{E_0}{m_0c^2})(1 - \cos\theta)} \quad (\text{Equation 1-3})$$

where E_0 is the energy of the incident photon, m_0 is the rest mass of an electron, c is the speed of light, and θ is the scattering angle.

For 511-keV photons, $E_{sc} = \frac{E_0}{1 + (\frac{E_0}{m_0c^2})(1 - \cos\theta)}$ (Equation 1-3 can be

simplified into $E_{sc}(MeV) = \frac{0.511 MeV}{2 - \cos\theta}$ (Equation 1-4 by setting $E_0 = m_0c^2 =$

0.511 MeV (Cherry 2006):

$$E_{sc}(MeV) = \frac{0.511 MeV}{2 - \cos\theta} \quad (\text{Equation 1-4})$$

The angular distribution of the scattered photons is modeled using the Klein-Nishina formula

$$\left(\frac{d\sigma}{d\Omega} = Zr_0^2 \left(\frac{1}{1 + \alpha(1 - \cos\theta)}\right)^2 \left(\frac{1 + \cos^2\theta}{2}\right) \left(1 + \frac{\alpha^2(1 - \cos\theta)^2}{(1 + \cos^2\theta)[1 + \alpha(1 - \cos\theta)]}\right)\right) \quad (\text{Equation 1-5) (Knoll 2010):}$$

$$\frac{d\sigma}{d\Omega} = Zr_0^2 \left(\frac{1}{1 + \alpha(1 - \cos\theta)}\right)^2 \left(\frac{1 + \cos^2\theta}{2}\right) \left(1 + \frac{\alpha^2(1 - \cos\theta)^2}{(1 + \cos^2\theta)[1 + \alpha(1 - \cos\theta)]}\right) \quad (\text{Equation 1-5})$$

where $\frac{d\sigma}{d\Omega}$ is the differential scattering cross section, Z is the atomic number, r_0 is the classical electron

radius, and $\alpha \equiv \frac{h\nu}{m_0c^2} = \frac{E_0}{m_0c^2}$.

Substituting $E_{sc} = \frac{E_0}{1 + (\frac{E_0}{m_0c^2})(1 - \cos\theta)}$ (Equation 1-3 into $\frac{d\sigma}{d\Omega} =$

$$Zr_0^2 \left(\frac{1}{1 + \alpha(1 - \cos\theta)}\right)^2 \left(\frac{1 + \cos^2\theta}{2}\right) \left(1 + \frac{\alpha^2(1 - \cos\theta)^2}{(1 + \cos^2\theta)[1 + \alpha(1 - \cos\theta)]}\right) \quad (\text{Equation 1-5 gives } \frac{d\sigma}{d\Omega} =$$

$$\frac{Zr_0^2}{2} P(E_0, \theta)^2 [P(E_0, \theta) + P(E_0, \theta)^{-1} - \sin^2(\theta)] \quad (\text{Equation 1-6:}$$

$$\frac{d\sigma}{d\Omega} = \frac{Zr_0^2}{2} P(E_0, \theta)^2 [P(E_0, \theta) + P(E_0, \theta)^{-1} - \sin^2(\theta)] \quad (\text{Equation 1-6})$$

where $P(E_0, \theta) = \frac{E_{sc}}{E_0}$ is the ratio of photon energy after and before Compton scattering.

Annihilation photons must escape the attenuating medium without interacting with matter prior to reaching the PET detectors. The relationship between 511-keV photons passing through a medium with

and without interaction prior to reaching a PET detector is determined using $I(x) = I(0)e^{-\int_0^x \mu(x')dx'}$

(Equation 1-7 ([Cherry 2006](#)):

$$I(x) = I(0)e^{-\int_0^x \mu(x')dx'} \quad (\text{Equation 1-7})$$

where $I(x)$ is the photon intensity (flux) transmitted through the medium, $I(0)$ is the flux of the source, $\mu(x')$ is a function of the linear attenuation coefficient of the medium, and x is the straight-line distance between the source and the PET detector.

The probability of an annihilation photon pair reaching a pair of PET detectors unattenuated (P_C), on the other hand, can be expressed as an exponential function using $P_C = e^{-\int_0^y \mu(y')dy'}$

(Equation 1-8 ([Badawi 1998](#)):

$$P_C = e^{-\int_0^y \mu(y')dy'} \quad (\text{Equation 1-8})$$

where y is the straight-line distance between the two PET detectors.

PET detectors

The working principal of PET relies on the detection of the 511-keV annihilation photons. To do so, PET detectors are designed to interact with the 511-keV photons, which are then converted into an analog electrical signal, then digitized, and ultimately transformed into *List-mode* events (which contain energy, timing, and position information) for data processing, data correction, and image reconstruction.

A PET detector consists of 3 main components: 1) a scintillator, 2) a photodetector, and 3) associated readout electronics.

Scintillator

A scintillator used in PET is typically a high-density solid, inorganic, optically transparent material that converts a high-energy photon into visible light which is then detected by a photodetector. Compton scattering and photoelectric absorption are the predominant conversion mechanisms. The amount of visible light emitted is proportional to the deposited energy and is emitted isotropically.

An ideal scintillator exhibits the following properties: 1) high absorption coefficient against high-energy photons (so they can be converted readily into visible light), which is typically characterized by its

density and effective atomic number; 2) high visible light output (so the energy of the high-energy photon can be determined with improved statistical uncertainty during signal integration), which is typically characterized by its photon yield; 3) fast light pulses (for optimal timing resolution), in the form of sharp rise time and short decay time; 4) sharp emission peak in the blue wavelength range (to match the maximum quantum efficiency (QE) of the photodetector, which typically lies in the blue wavelength range); and 5) non-hygroscopic (to maximize stability and longevity). Table 1-1 shows the common scintillator materials used in PET detectors.

Table 1-1. Common scintillator materials used in PET detectors ([Melcher 2000](#), [Kemp 2006](#), [Nassalski 2007](#), [Cherry 2012](#)).

Material name	Lutetium oxyorthosilicate (LSO)	Lutetium-yttrium oxyorthosilicate (LYSO)	Bismuth germanate (BGO)	Gadolinium orthosilicate (GSO)	Lanthanum bromide (LaBr ₃)
Density (g / cm ³)	7.4	7.1	7.13	6.71	5.3
Effective atomic number (Z)	65	65	73	59	46
Photon yield (photons / MeV)	20000 – 30000	32000	8000	12000 – 15000	61000
Decay time (ns)	40	41	300	60	35
Emission Peak (nm)	420	420	480	430	358
Hygroscopic?	No	No	No	No	Yes

Photodetector

A photodetector converts visible light created in a scintillator into an analog electrical signal. The electrical signal is amplified to produce a usable signal pulse for processing. One of the most used PET photodetectors is the photomultiplier tube (PMT). The PMT is a high-voltage (10³ V) device that consists of a series of dynodes coated with a photo-emissive material. When a visible light photon is absorbed by the photocathode of the PMT, a photoelectron is ejected and accelerated into the first dynode. Additional photoelectrons are then ejected and accelerated into the subsequent dynodes, ultimately resulting in a pulse signal that is proportional to the number of optical photons created in the scintillator and, thus, proportional to the deposited energy of the high-energy photon in the scintillator. The resulting signal gain

from a PMT is about 10^6 . Despite its high gain, stability, and ruggedness, PMTs are being phased out in favor of silicon photomultipliers (SiPMs), a more affordable alternative that retains most of the advantages PMTs have.

An SiPM is a solid-state device that consists of an array of microcells containing single-photon avalanche photodiodes (SPADs) operating in Geiger mode. When a visible light photon is absorbed by a SPAD inside an SiPM, an electron-hole pair is created, and the bias voltage applied to the SiPM leads to a self-perpetuating ionization avalanche, ultimately leading to a pulse signal (in the form of a binary output, or in other words, an on/off switch) when used in conjunction with a quench resistor that terminates the avalanche process. The amplitude of the output pulse of an SiPM is the sum of the pulses from the triggered SPADs in the SiPM, which is proportional to the number of impinging optical photons on the SiPM, and is therefore proportional to the deposited energy of the high-energy photon in the scintillator. The primary advantage of SiPM is its high gain (10^6), low operating voltage ($\sim 30\text{V}$), and high quantum efficiency ($\sim 50\%$) ([Otte 2006](#), [Frach 2009](#), [SenL Tech](#)), and are relatively less sensitive to magnetic fields, compared to PMTs.

Readout electronics

The readout electronics are responsible for shaping and converting the analog output of a photodetector into discretized information (e.g. energy, timestamp, position, etc.). Conventionally in some PET systems, the output pulse of a photodetector is processed through a preamplifier, then an amplifier, and finally an analog-to-digital converter (ADC). The preamplifier amplifies and shapes the photodetector output into a signal with a rapid, rising component and a negative exponential component. The time it takes for the signal to rise from 10% to 90% of the peak amplitude called the rise time ([Leo 1994](#), [Knoll 2010](#)). After the peak, the time it takes for the signal to decay to $\frac{1}{e}$ (37%) of the peak amplitude is called the decay time ([Cherry 2012](#)). The amplifier further magnifies the preamplifier output and reshapes it into a narrow pulse for easier extraction of energy, timing, and position information. The ADC discretizes the signal which ultimately leads to a single event (containing the energy, timestamp, and position information of a detected event).

Block detector

The block detector is a basic detector unit used in PET scanners ([Casey 1986](#)) consisting of a block of scintillator crystals coupled to 4 PMTs or SiPMs, with a light guide sandwiched in between. It enables improved detector spatial resolution by utilizing scintillator crystals smaller than the photodetectors, as well as reducing the number of photodetectors (which reduces overall scanner costs). The sum of the 4 photodetector signals is proportional to the energy of the high-energy photon. With this setup, the x-y position where the annihilation photon is detected can be determined using $X =$

$$\frac{(PMT_A+PMT_B)-(PMT_C+PMT_D)}{PMT_A+PMT_B+PMT_C+PMT_D} \quad (\text{Equation 1-9 and } Y = \frac{(PMT_A+PMT_C)-(PMT_B+PMT_D)}{PMT_A+PMT_B+PMT_C+PMT_D})$$

(Equation 1-10 ([Cherry 2012](#)):

$$X = \frac{(PMT_A+PMT_B)-(PMT_C+PMT_D)}{PMT_A+PMT_B+PMT_C+PMT_D} \quad (\text{Equation 1-9})$$

$$Y = \frac{(PMT_A+PMT_C)-(PMT_B+PMT_D)}{PMT_A+PMT_B+PMT_C+PMT_D} \quad (\text{Equation 1-10})$$

where PMT_A , PMT_B , PMT_C and PMT_D represent the 4 photodetector signals.

Coincidence event generation

PET relies on the principles of annihilation coincidence detection (ACD) to generate coincidence events ([Cherry 2012](#)). In the following, the ACD mechanism is referred to as a coincidence processor. The primary function of a coincidence processor is to identify pairs of annihilation photons that may be originated from the same annihilation event. LORs are drawn between 2 scintillator crystals, indicating that the annihilation event originated from somewhere along that line. With enough coincidence events collected, an image volume that reflects the radiotracer distribution can be reconstructed.

Coincidence processing is typically performed using hardware. In analog setups, if two opposing detectors produce an input logic pulse (each with a time width τ , i.e. the coincidence resolving time) within a time window (i.e. a coincidence time window of 2τ , to account for negative time difference as one detector is presumed to always detect a photon earlier than the other detector), the coincidence processor produces an output logic pulse that reflects a coincidence detection. The amplitude threshold is set such that the amplitude sum of the 2 overlapping input pulses must exceed for a coincidence event to be counted. Modern PET scanners (as well as in computer simulations) perform coincidence processing

with digitized information of single events. For instance, a coincidence event is counted when the time difference of 2 single events is less than the coincidence time window (τ to be exact, since the single events are in chronological order), in addition to fulfilling additional requirements in the coincidence processor. Typically, only the coincidence output is stored during data acquisition, and the single events are discarded during coincidence processing.

In some PET scanners, single events are stored during data acquisition instead of coincidence events. As such, coincidence processing is performed post-acquisition using software. While uncommon in commercial PET scanners, this method enables the ability to re-process the same set of single event data with varying parameters. This is not feasible with most PET scanners that utilize hardware-based coincidence processors, since most of the single event information required for coincidence processing is either lost, or significantly altered. For example, while 2 single events contain absolute time information, a coincidence event may only contain the time difference between the single event pair.

A coincidence processor typically consists of 1) an energy window, 2) a time window, 3) a geometric window, and 4) a coincidence policy. Figure 1-2 provides a visual workflow of a coincidence processor. A brief description of each component is described below:

Energy window

An energy window is used to exclude single events that have undesired energy values for coincidence processing. The energy window is comprised of 1) a lower-level discriminator (LLD), and 2) an upper-level discriminator (ULD). The LLD excludes single events that may have 1) undergone scattering (since only a portion of the 511-keV photon energy is deposited in the scintillator crystals), or 2) not originated from an annihilation event (e.g. ^{176}Lu background, with energies of 307 keV, 202 keV and 88 keV ([Conti 2017](#))). The ULD excludes single events that are either 1) affected by pulse pile-up (where the energies of 2 uncorrelated annihilation photons are summed together), or 2) not originated from an annihilation event (e.g. 1275 keV prompt gamma emission from a ^{22}Na source). A typical energy window for a commercial clinical PET scanner is around 435 – 650 keV ([Jakoby 2011](#), [Spencer 2021](#)).

Time window

A time window is an essential component in a coincidence processor that makes ACD possible. It is used to exclude pairs of single events that are too far apart in time and that are therefore not originated from the same annihilation event. The premise is that pairs of annihilation photons that lead to coincidence events are detected by the PET scanner within a specified time difference (typically within nanoseconds). To identify possible coincidence events, a standard time window is typically set to a value appropriate for the transaxial FOV of the scanner (based on the product of the speed of light and the time required for a photon to travel across the transaxial FOV). A typical time window for a conventional, clinical PET scanner is around 4 ns ([Jakoby 2011](#)). Multiple time windows (e.g. a variable time window) may be used for longer PET scanners (in conjunction with geometric windows) to ensure that the longer, more oblique LORs are accounted for, while minimizing the number of random coincidences ([Spencer 2021](#)).

Geometric window

A geometric window is used to exclude coincidence events outside of the defined FOV. For instance, an LOR between 2 adjacent block detectors is typically outside the defined PET transaxial FOV and is therefore excluded during coincidence processing. This effectively restricts the number of radial bins in a *Sinogram*. It may also be used in conjunction with a variable time window to limit the axial acceptance angle of the scanner, which effectively limits the span of a *Michelogram*. In practice, a geometric window may be substituted by trimming the radial bins of a sinogram, and/or zeroing out elements in the sinogram and Michelogram prior to image reconstruction.

Coincidence policy

A coincidence policy consists of 1) a coincidence window type, and 2) a multiples policy. A coincidence window type determines which single event may open a time window for coincidence processing. In single window (SW) mode, single events (e.g. singles #2, #3, and #4 as shown in Figure 1-2) may not open its own time window if they are already inside another time window. In multiple window (MW) mode, all single events open their own time windows. MW mode maximizes the number of true

coincidences detected in the PET scanner, at the expense of increasing the number of random coincidences detected, particularly at higher single event count rates. A multiples policy is used for screening out specific coincidence events when 3 or more single events, including the reference single event (i.e. the single event that opened the time window), are within the same time window. Common coincidence policies include *takeAllGoods* (accepting all valid coincidence events) and *killAll* (discarding all coincidence events) (Morales 2015). At higher single event count rates, *MW*, *takeAllGoods* maximizes the number of true coincidences to be detected, at the expense of increased number of random coincidences. *SW*, *killAll* minimizes the number of random coincidences, at the expense of reduced number of true coincidences, which also effectively increases the coincidence dead-time of the scanner.

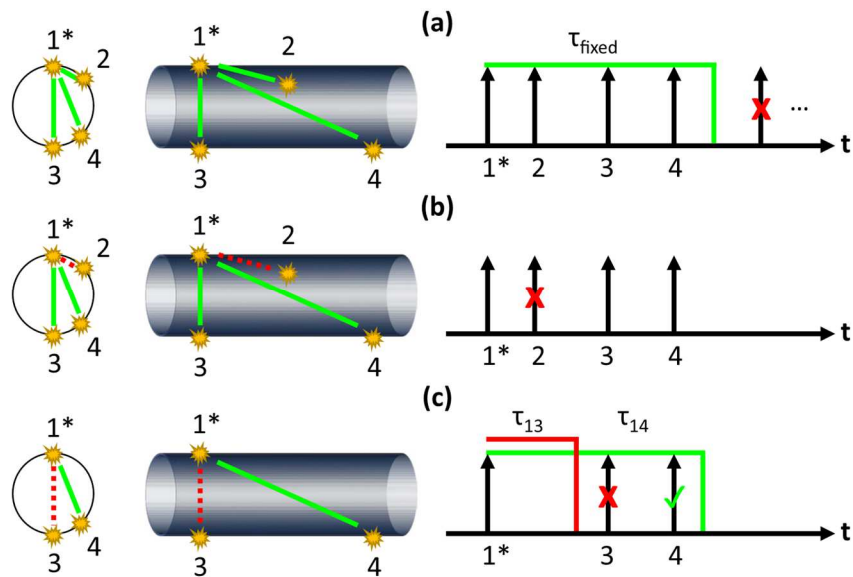


Figure 1-2. A visual example of a coincidence processor, shown with four total energy-qualified singles in the time window (in 2-D, 3-D views and time domains, respectively). (a) Three potential coincidences (coincidence pairs 1-2, 1-3 and 1-4) in the primary, fixed time window (τ_{fixed}). (b) Coincidence pair 1-2 is rejected by the geometric window. (c) Coincidence pair 1-3 is rejected by the variable time window (τ_{13}), while coincidence pair 1-4 is accepted by the variable time window (τ_{14}). Note: the asterisk (*) denotes the reference single event. Also, coincidence pairs 2-3 and 2-4 are not considered in the time window opened by 1 (τ_{fixed}) but will be considered in the time window opened by 2.

Coincidence event types

In PET, coincidence events produced by the PET scanner do not necessarily originate from the same annihilation event and the annihilation photons might not reach the detectors unscattered. The events are typically separated into 4 categories. Figure 1-3Figure 1-4 shows a representation of each type of coincidence events described below:

True coincidences – a type of coincidence event produced by the PET scanner where both annihilation photons originated from the same annihilation event and did not undergo scattering. This is the desired type of coincidence events in PET.

Scattered coincidences – a type of coincidence event produced by the PET scanner where at least one of the two annihilation photons originated from the same annihilation event but underwent scattering before detection. Scattered coincidences are separated into the following categories: 1) single-order scattered coincidences (single scatter) and 2) higher-order scattered coincidences (double scatter, triple scatter, etc.). A higher-order scattered coincidence event occurs when the total number of times both photons combined have scattered is 2 or more. S_{xy} denotes a scattered coincidence event S where the subscripts x and y correspond to the number of times the 1st and 2nd annihilation photons have scattered. Visual examples of higher-order scattered coincidences are shown in Figure 1-4 below. Scattered coincidences are undesirable in PET because they lead to incorrect LOR assignments, reducing image contrast surrounding the subject and affecting quantification.

Random coincidences – a type of coincidence event produced by the PET scanner where the 2 annihilation photons originated from uncorrelated annihilation events are detected and are accepted as a coincidence pair. Random coincidences are undesirable in PET because they lead to incorrect LOR assignments, reducing image contrast uniformly across the image volume and affecting quantification.

Multiple coincidences – a type of coincidence event produced by the PET scanner where more than 1 coincidence event is accepted in a time window. This occurs when 3 or more singles events (including the reference single event) are in a time window and are accepted as coincidence pairs. A multiple coincidence event is a double-edged sword because there may not be a true coincidence event in it.

Using a *MW, takeAllGoods* coincidence policy, n single events form up to $n - 1$ coincidences in the time window of the reference single event (as shown earlier in Figure 1-2). However, there may be fewer than $n - 1$ valid coincidences in a multiple coincidence event. This occurs when one or more potential coincidences are rejected by the geometric window and/or variable time window. Here multiple coincidences are defined to have 2 or more valid coincidence events in a time window.

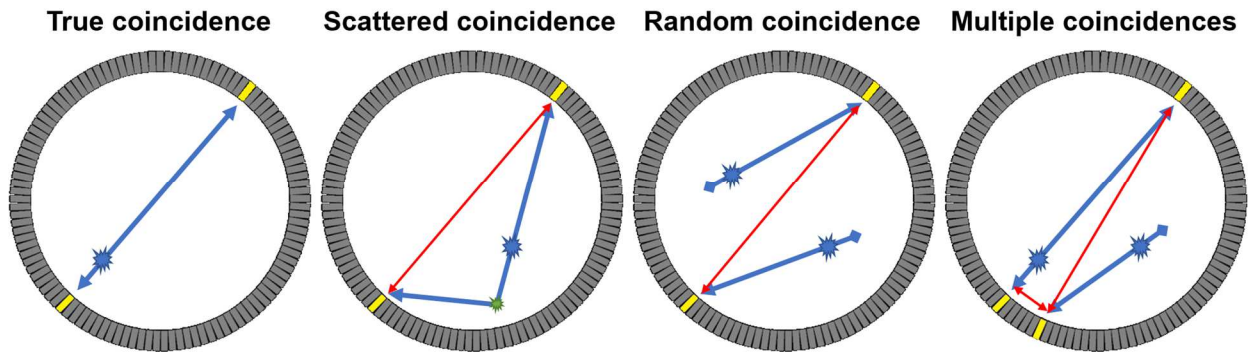


Figure 1-3. Types of coincidence events. Red lines indicate incorrectly assigned LORs.

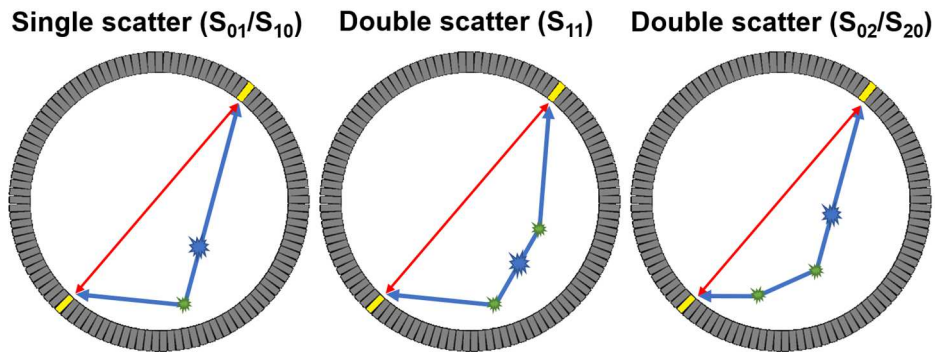


Figure 1-4. Types of scattered coincidence events. S_{xy} denotes the number of times each of the 2 annihilation photons scattered.

During PET data acquisition, the coincidence events detected by the PET scanner contain a mixture of the coincidence event types described earlier. Typically, two categories of coincidence events are stored in the coincidence output: 1) prompt coincidence events, and 2) delayed coincidence events.

Prompt coincidences – a type of coincidence event produced by the PET scanner during data acquisition. It contains a mixture of trues, scattered and random coincidence events that are indistinguishable from each other. To obtain an estimate of the true coincidence event rate, estimates of

scattered and random coincidences are subtracted from the prompt coincidence data to calculate the net true coincidence event rate.

Delayed coincidences – a type of coincidence event produced by the PET scanner during data acquisition by adding a time delay in one of the two PET detector channels prior to coincidence processing. A sufficiently large time delay (typically in the order of 100 ns) ensures the delayed coincidence channel output contains only random coincidence events. This is commonly done to estimate the number of random coincidence events in the prompt coincidence data channel.

PET data representation

To reconstruct a 3-D image volume that reflects the radiotracer distribution in a subject, millions to billions of coincidence events are detected by a PET scanner during data acquisition. To handle the large number of coincidence events, the coincidence output is organized in specific ways prior to data correction and image reconstruction. The most common coincidence data representation methods are described below.

List-mode

List-mode data contains a sequential list of coincidence events stored in a vectorized data format. Each list-mode event contains the locations of the crystal pair, typically in the form of crystal IDs. Depending on the implementation, energy, time difference and interaction depth information may be included (details regarding *Time-of-flight (TOF)* PET and *Depth-of-interaction (DOI)* PET are described later). The time period of each list-mode event (e.g. 0 – 1 s, 1 – 2 s, etc.) can either be 1) encoded using timestamp headers (if all of the data is stored in one file), or 2) encoded using multiple files where each file corresponds to a specific time period. The exact format of the list-mode data varies between different PET scanner manufacturers.

Sinogram

A sinogram is a 2-D histogram where the rows represent the projection angle ϕ , and the columns represent the radial offset r from the center of the scanner (Figure 1-5). For PET data, each sinogram bin

corresponds to the number of coincidence events recorded for a specific LOR at a particular radial offset and angle relative to the defined coordinate system of the scanner. The sinogram can be used for data correction, as well as for reconstructing a 2-D image.

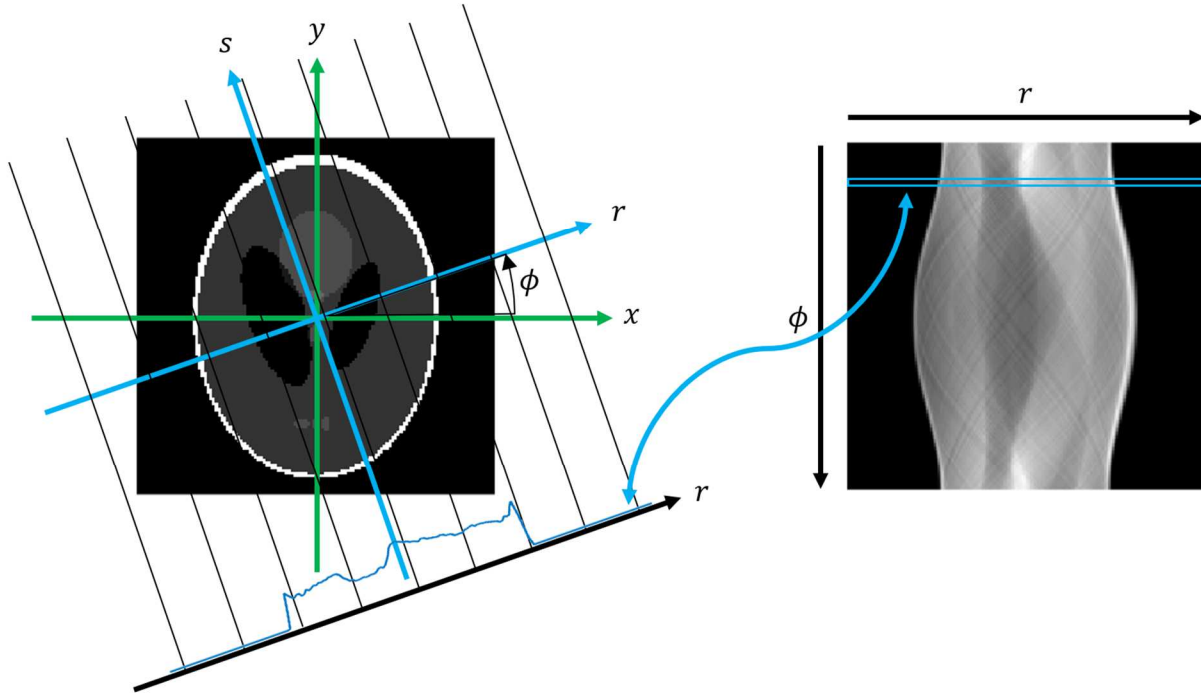


Figure 1-5. (Left) A projection profile of an image at angle ϕ . (Right) A sinogram.

In practice, adjacent angles in a PET sinogram are typically interleaved together to maximize radial sampling (i.e. the number of radial bins), which is considered to be more suitable for image reconstruction algorithms, at the expense of reduced angular sampling (i.e. the number of projection angles) ([Cherry 2006](#)). This means that the number of radial bins is approximately doubled, while the number of angular bins is halved.

Michelogram

A Michelogram is used to represent 3-D PET data ([Fahey 2002](#)). A Michelogram can be thought of as a 4-D sinogram, where the additional 2 dimensions correspond to the axial locations of the LOR (Figure 1-6). This means that a Michelogram contains both direct (axially in-plane) and oblique (axially cross-plane) sinograms. The extent of axial data combined is known as the span ([Fahey 2002](#)). Larger

spans include more oblique sinograms. A Michelogram is used in 3-D PET scanners where increased scanner sensitivity is desired, compared to the earlier 2-D PET scanners where only coincidence events are accepted if they are in direct, or cross axial planes (i.e. LORs that cross adjacent crystal rings)

([Daube-Witherspoon 1987](#), [Fahey 2002](#)).

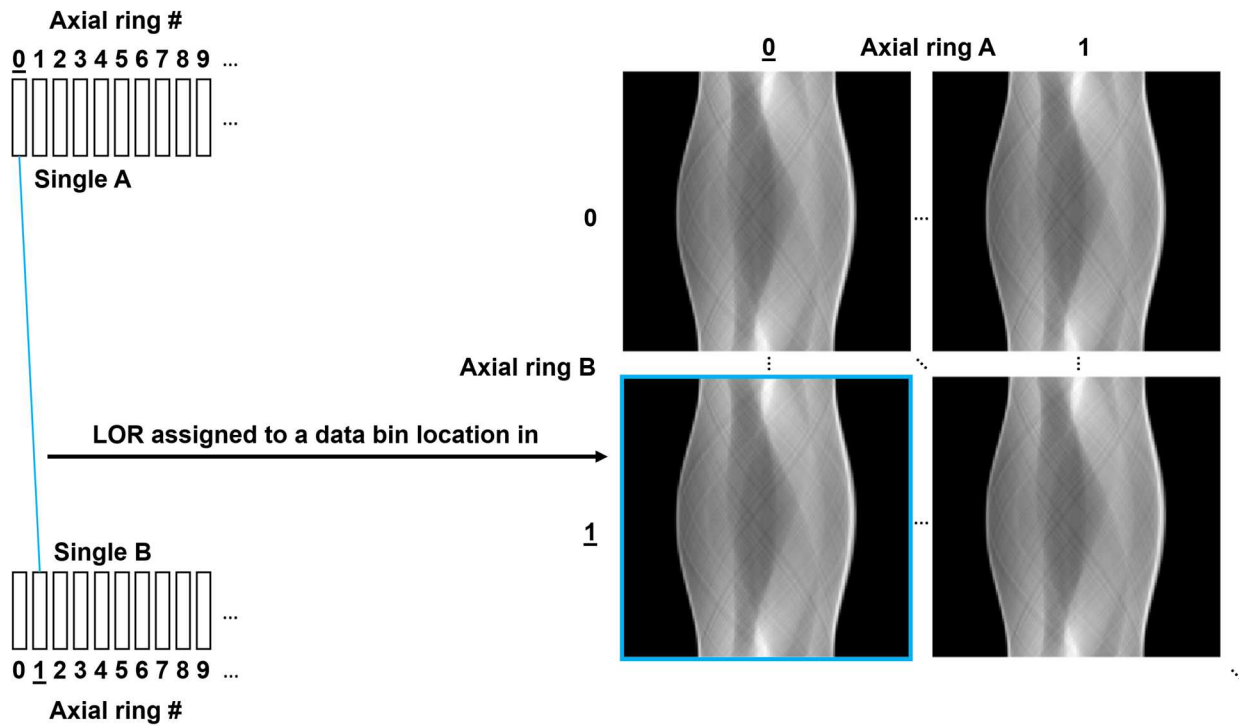


Figure 1-6. Relationship between an LOR and a Michelogram (portrayed as a 4-D sinogram).

Single-slice re-binning (SSRB)

In 2-D PET, a tomographic image volume is produced by performing 2-D image reconstructions of a series of direct and cross plane sinograms parallel to the scanner axis. To perform 2-D image reconstruction with 3-D PET data, oblique sinograms are grouped together such that they can be represented in direct plane sinograms. One such method is the single-slice re-binning (SSRB) algorithm ([Daube-Witherspoon 1987](#)). SSRB reorganizes the axially oblique LORs such that a coincidence event is assumed to be originated from a direct plane halfway across the LOR, thereby compressing the data into a series of direct plane sinograms. The primary advantage of this method is that the total number of sinograms (and therefore the total sinogram data size) is reduced by a factor of $\frac{2n-1}{n^2}$, where n is the number of axial crystal rings. Also, since the data can be treated as a series of direct plane sinograms,

the image reconstruction time is significantly reduced compared to 3-D image reconstructions. The primary drawback of SSRB is that the radially off-centered annihilation events become more susceptible to axial mispositioning since the events do not originate from the midpoints of the LORs. More sophisticated methods, such as SSRB-TOF ([Mullani 1982](#)) that utilizes TOF information, multi-slice re-binning (MSRB) ([Lewitt 1994](#)) that increments multiple direct plane sinograms for each oblique LOR, and Fourier re-binning (FORE) ([Defrise 1997](#)) that approximates direct sinograms using 2-D Fourier transform of oblique sinograms, were developed to compensate for axial mispositioning.

PET data corrections

The coincidence data acquired by a PET scanner is affected by a complex interplay of physical factors (e.g. attenuation, detector efficiency, scatter, dark count, motion, etc.) and contains various types of coincidence events discussed earlier. Using the PET data directly without modifications during the image reconstruction step can result in reconstructed images that have poor spatial resolution, reduced contrast, and incorrect quantification (in the form of bias, non-uniformity, and noise). Therefore, PET data is corrected for the factors discussed below prior to image reconstruction to obtain quantitatively accurate and high-quality images.

Normalization

To account for manufacturing variations in the scintillator crystals, as well as in the photodetector and front-end electronics, which ultimately leads to variations in coincidence detection efficiencies for each detector pair, detectors in a PET scanner are cross-calibrated using a technique called normalization. If normalization effects are unaccounted for prior to image reconstruction, the resulting images may contain high frequency artifacts.

The simplest form of normalization calibration involves irradiating each detector pair uniformly with a low radioactivity source to create a count rate map. The number of counts obtained from each detector pair is normalized to the mean number of counts from all detectors so that the normalization process does not create a bias in the system level. The normalization factor for each detector pair (n_{ij}) is

calculated using $n_{ij} = \frac{N_{ij}}{\bar{N}}$ (Equation 1-11:

$$n_{ij} = \frac{N_{ij}}{\bar{N}} \quad (\text{Equation 1-11})$$

where N_{ij} is the number of counts detected by the detector pair ij , and \bar{N} is the mean number of counts detected by all detector pairs. The reciprocal (i.e. the normalization correction factor) is applied to the experimental data prior to image reconstruction, as shown in $C_{ij,normalized} = \frac{C_{ij,observed}}{n_{ij}}$

(Equation 1-12:

$$C_{ij,normalized} = \frac{C_{ij,observed}}{n_{ij}} \quad (\text{Equation 1-12})$$

where $C_{ij,normalized}$ and $C_{ij,observed}$ are the normalized and observed number of counts detected by detector pair ij , respectively.

One of the limitations of direct normalization is the massive number of counts (hence the acquisition time) required to achieve low statistical noise. To reduce the time required for normalization, component-based methods were developed to estimate normalization factors based on the efficiencies of individual detector elements, which can be estimated using all of the counts from the normalization scan ([Hoffman 1989](#)). A simplified implementation of component-based normalization, expressed as a product of factors, is shown in $n_{ij} = \varepsilon_i \varepsilon_j g_{ij}$ (Equation 1-13:

$$n_{ij} = \varepsilon_i \varepsilon_j g_{ij} \quad (\text{Equation 1-13})$$

where ε_i and ε_j are the efficiencies of detector elements i and j , and g_{ij} is the geometric efficiency of the detector pair ij . Additional normalization components were investigated and some were found to have significant effects on the quality of reconstructed images in 3-D PET ([Badawi 1999](#)).

Attenuation Correction

In PET, annihilation photons travel through non-negligible amounts of attenuating medium in most phantoms as well as in human subjects prior to reaching the photodetectors. This means that some of the annihilation photons would be scattered or absorbed. If this physical effect not accounted for, the reconstructed images of a uniform cylinder would appear to have higher radiotracer concentrations towards the edge of the phantom, since annihilation photons originated from the edge of the phantom, on average, travel through less attenuating medium. Alternatively, the reconstructed images of a heterogenous object (but with uniform activity distribution) will appear to have non-uniform radiotracer

concentrations if no attenuation correction is performed. To recover the correct radiotracer distribution, the LOR of each detector pair is corrected for attenuation effects to compensate for photon pairs that travel through a non-negligible amount of attenuating medium. This is done by applying an attenuation correction factor, the reciprocal of the probability that both annihilation photons escape an attenuating medium for each LOR (as previously defined in $P_C = e^{-\int_0^y \mu(y') dy'}$ (Equation 1-8).

The attenuation correction factor required for each LOR can be directly measured via: 1) the combination of a blank scan and a transmission scan; or 2) a computed tomography (CT) scan, which is the current standard for commercial PET/CT scanners. The 1st method utilizes a radioactive rod source revolving around the scan subject to obtain the transmission scan data. The blank scan data is divided by the transmission scan data to obtain the attenuation correction factors. The 2nd method utilizes images from a CT scan and converts the CT image volume into a 511-keV attenuation map for attenuation correction via bi-linear interpolation ([Carney 2006](#)). The primary challenge in attenuation correction involves obtaining sufficient photon counts to minimize the noise and bias for the attenuation correction factor of each LOR, especially when the reduction of radiation dose from the CT is desired. Another challenge is the attenuation artifacts caused by metal implants which can affect the accuracy of the attenuation correction if not accounted for.

Dead-time correction

Detectors that are constantly bombarded by photons may be rendered temporarily inoperable. The time that it takes for the detector to become functional again is known as the dead-time. The primary effect of dead-time is the apparent loss of measured count rate relative to the true count rate, free from dead-time effects. Another side effect of dead-time is pulse pileups of photons, which, depending on the exact energy window used, may lead to the loss or mispositioning of an event. The dead-time of a PET scanner is commonly estimated using either 1) a paralyzable, or 2) a non-paralyzable dead-time model, as shown in $R_{observed} = R_{true}e^{-R_{true}\tau}$ (Equation 1-14 and $R_{observed} = \frac{R_{true}}{1+R_{true}\tau}$

(Equation 1-15:

$$R_{observed} = R_{true}e^{-R_{true}\tau} \quad \text{(Equation 1-14)}$$

$$R_{observed} = \frac{R_{true}}{1+R_{true}\tau} \quad (\text{Equation 1-15})$$

where $R_{observed}$ is the observed count rate, R_{true} is the true count rate, and τ is the dead-time. In a paralyzable dead-time model, the observed count rate peaks and decreases with increasing true count rates. In a non-paralyzable model, the observed count rate plateaus with increasing true count rates. The dead-time behavior of a detector is typically described by a paralyzable dead-time model, and the dead-time behavior of the front-end electronics is typically described by a non-paralyzable dead-time model.

To correct for dead-time in the PET data, a dead-time lookup table (LUT) is used to apply a multiplicative correction factor for each sinogram bin (in sinogram-based reconstruction) or coincidence event (in list-mode reconstruction).

Randoms Correction

As mentioned previously, random coincidences in PET data imposes a noisy background into the reconstructed images, thereby reducing image contrast and quantitatively accuracy. To correct for random coincidences, a random coincidence estimate is acquired for subtraction from the measured prompt coincidence data. This yields the sum of true + scattered coincidence data. The number of random coincidences is typically estimated via: 1) detector single event rates or 2) delayed coincidence channel. Random coincidence estimation using detectors singles rates can be acquired using $R_{ij} =$

$$2\tau R_i R_j \quad (\text{Equation 1-16:})$$

$$R_{ij} = 2\tau R_i R_j \quad (\text{Equation 1-16})$$

where R_{ij} is the random coincidence rate between detectors i and j , and τ is the coincidence resolving time. Occasionally, 2τ is rewritten as Δt which is the coincidence time window. The primary advantage of randoms estimation via detector single event rates is that the randoms estimate has a lower noise level than the delayed coincidence channel method, since R_i and R_j (typically measured in s^{-1}) are much larger compared to the number of random coincidences measured in the delayed coincidence channel (measured within the span of the coincidence time window). The primary drawback of the method is that it

can introduce quantitative bias to the randoms estimate at increasing count rates, since the dead-time properties between the PET detectors and the coincidence processor can be different.

To directly measure the number of random coincidences, the delayed coincidence channel method is used. The method utilizes a coincidence processor that delays the signal of the other detector by a period long enough such that coincidence events arising from the detector pair are uncorrelated. The primary advantage of this method is that the randoms estimation is free from quantitative bias since the delayed window method is an independent measurement of random coincidences using the same type of coincidence processing method as the prompt data. The primary drawback of this method is that since the number of random coincidences in a coincidence time window is very small, the noise level of the prompt minus delay coincidence data may become significant. Randoms subtraction using the delayed channel method also adds an additional random coincidence noise component to the data.

Scatter correction

Scatter correction is arguably the most challenging correction performed in PET since scattered coincidences are only identifiable based on their deposited energies. At the same time, true coincidences do not necessarily deposit exactly 511 keV of energy for each annihilation photon. The scintillator crystals used in a PET detector also do not have perfect energy resolution, which necessitates a wider energy window to capture most of the true coincidence events, at the expense of introducing scatter contamination. Without scatter correction, the reconstructed images contain a hazy background on the scan subject, affecting image contrast and quantitative accuracy.

Scatter correction methods for 3-D PET can generally be separated into the following categories: 1) convolution/deconvolution-based techniques, 2) multiple-energy window techniques, 3) gaussian-fitting techniques, 4) analytical model-based techniques, and 5) Monte Carlo model-based techniques. Convolution/deconvolution-based techniques estimate the scatter component by applying a scatter response function to the emission data ([Shao 1991](#), [McKee 1992](#), [Bailey 1994](#), [Lercher 1994](#)). While these methods consider the radioactivity distribution in the object, they do not account for object attenuation and can be sensitive to the radioactivity outside the FOV of the scanner.

Multiple-energy window techniques for scatter correction typically involve acquiring PET data in 2 or more energy windows, and then subtracting a scaled scatter component to obtain the true coincidence component ([Bendriem 1993](#), [Shao 1994](#), [Grootoank 1996](#)). One example involves acquiring PET data in 2 non-overlapping energy windows: a lower-energy scatter window at 200 – 380 keV, and the photopeak window at 380 – 850 keV ([Grootoank 1996](#)). The primary drawback of such approach is that the scatter distributions from non-overlapping energy windows are different from each other due to the increased contribution of higher-order scatters in the lower-energy window than in the photopeak window. Another approach utilizes 2 overlapping energy windows: a broad energy window at 250 – 850 keV, and an above-photopeak narrow energy window at 550 – 850 keV to capture only true coincidence events ([Bendriem 1993](#)). While such implementation ensures that the scatter distribution is consistent in both energy windows, the statistical quality of the scatter-subtracted data can become poor due to the lower number of events collected in the narrow energy window.

Gaussian-fitting techniques for scatter correction involving fitting a gaussian function to the tails of the projection profiles ([Cherry 1995](#), [Stearns 1995](#)), assuming the tails contain only scattered coincidences. This method performs well in regions where the activity and scatter distributions are smooth and do not occupy a large portion of the FOV (such as the brain), but not in scenarios where an inhomogeneous object covers a majority of the FOV (such as the chest and the abdomen).

Analytical model-based scatter correction techniques utilize both the attenuation and emission data, along with a model of the PET scanner to estimate the scatter component, using the Klein-Nishina formula ([Ollinger 1996](#), [Watson 2000](#)). These methods calculate the probability of Compton scattering for every attenuation image voxel contributing to a specific LOR and sums all probabilities for every LOR. Analytical model-based scatter correction is by far the most common scatter correction methods implemented in clinical scanners ([Zaidi 2007](#)). A drawback of analytical model-based techniques is that they can be sensitive to scattering from events outside the FOV of the scanner. Also, standard analytical model-based techniques only account for single scatters, and its accuracy can therefore be reduced in scenarios where higher-order scatters are more prevalent, such as in PET scanners with larger axial acceptance angles.

Monte Carlo-based scatter correction techniques incorporate the reconstructed activity image and the attenuation image in a Monte Carlo simulation of a PET scanner ([Levin 1995](#), [Holdsworth 2002](#)). Monte Carlo-based methods can be one of the most accurate scatter correction techniques when the scatter distribution is complex, and the contribution of higher-order scatters become significant. The main limitation of Monte Carlo-based scatter correction methods is that they are by far the most computationally demanding scatter correction techniques. Parallel computing techniques, such as the use of graphics processing units (GPUs) and cloud computing, can minimize this drawback.

Decay correction

The radiotracers used in PET typically have half-lives that span between minutes to hours. As a result, the radioactivity inside the scan subject can drop noticeably over the duration of the PET acquisition as well as in the image frame (in dynamic PET imaging). To ensure the reconstructed images are quantitatively accurate, the decay effect is typically corrected to the start of the data acquisition. The effective decay factor, $DF_{eff}(t, \Delta t)$, is calculated using $DF_{eff}(t, \Delta t) = DF(t) \times [(1 - e^{-x})/x]$

(Equation 1-17 ([Cherry 2012](#)):

$$DF_{eff}(t, \Delta t) = DF(t) \times [(1 - e^{-x})/x] \quad \text{(Equation 1-17)}$$

where t is the start time of the image frame, Δt is the frame duration, $DF(t)$ is the decay factor at time t , and $x = \ln 2 \times \frac{\Delta t}{T_{1/2}}$. The inverse of the effective decay factor is therefore the effective decay correction factor used for decay correction.

Dose calibration

The voxel intensity in a reconstructed PET image, with perfect data corrections, is proportional to the radioactivity concentration in that voxel. To convert the voxel values into physical units (e.g. in kBq/mL), a dose calibration scaling factor is applied globally to the reconstructed image volume. The dose calibration factor is typically obtained by first scanning a uniform cylinder phantom, and then calculated as the ratio between the mean volume-of-interest (VOI) of the uniform cylinder and the known radioactivity concentration of the uniform cylinder.

PET image reconstructions

Image reconstruction is a process which transforms coincidence events into a tomographic image volume that reflects the radioactivity distribution in the body. In theory, a PET scanner with very fine timing resolution (< 10 ps) could localize an annihilation event along an LOR to within 1.5 mm, which would eliminate the need for image reconstruction since the location of an annihilation event can be accurately determined. However, current commercial PET systems could only achieve a timing resolution of 210 ns ([van Sluis 2019](#)). To create quantitatively accurate and high-quality images with fine spatial resolution today, image reconstruction remains a necessity.

Early attempts in PET image reconstruction include analytical techniques, such as back projection (BP) and filtered back projection (FBP), which utilized frequency filters prior to back projection to amplify high spatial frequency information. These techniques involve back projecting coincidence events in image space. Back projection methods often result in poor image quality and poor quantitative accuracy due to the relatively coarse linear and angular sampling of PET data, and that they do not account for the physical and statistical properties of the data ([Cherry 2006](#)).

Today, iterative reconstruction techniques are by far the predominant image reconstruction methods implemented on commercial PET scanners. These techniques begin with a forward projection of an initial image estimate and then compare the estimated projection data to the measured data, and update the image estimate iteratively. The most well-known iterative reconstruction algorithm is the maximum-likelihood, expectation-maximization (MLEM) algorithm. The ML-EM algorithm maximizes the Poisson log likelihood function to predict the ground truth image ([Cherry 2006](#)). Iterative reconstruction techniques are computationally demanding, which led to the development of the ordered-subset, expectation-maximization (OSEM) algorithm ([Hudson 1994](#)). The OSEM algorithm only back projects subsets of the acquired data in each iteration, which improves the reconstruction speed, at the expense of increased image noise for the same number of effective iterations compared to the MLEM algorithm, and can, in some cases, introduce oscillations in the solution with smaller subset sizes ([Huang 1998](#)). The OSEM algorithm is the most common iterative reconstruction algorithm used in clinical PET scanners today.

Monte Carlo PET simulations

Monte Carlo (MC) PET simulations involve tracking many annihilation photons through their trajectories and interactions with surrounding medium and the scanner model to produce list-mode PET data that resembles data obtained from a physical PET scanner. Components of a MC PET simulation include: 1) the scanner model, including its geometry, physical and readout electronics parameters, 2) the model of the object being scanned, including the material and activity distribution, and 3) the physics engine. With accurate modeling a PET scanner, a MC PET simulation can produce results that match closely to the physical scanner. Today, it is arguably a standard practice to perform MC PET simulations prior to constructing the physical scanner to predict the performance of the physical scanner which can help minimize scanner development costs. Common open-source Monte Carlo simulation software available for PET simulations include 1) Geant4 Acquisition for Tomographic Emission (GATE), and Simulation System for Emission Tomography (SimSET).

The primary drawback of MC PET simulations is that it is computationally demanding, and that most simulation software only run on a single CPU thread. A MC PET simulation that involves simulating a human subject can easily take weeks, if not months. One way to counter this drawback is to parallelize the simulation by running multiple instances of the simulation software and dividing the entire simulation into multiple parts. Newer, GPU-based MC PET software, such as gPET, have been developed to speed up a MC PET simulation by a factor of 500 ([Lai 2019](#)). For relatively simple simulations (such as sensitivity and count rate performance simulations) however, a consumer laptop may be sufficient.

Another challenge in MC PET simulations is that due to the complexity of most open-source MC PET simulation software, customization outside of its design specifications is difficult. Also, since most MC PET software utilizes a generic digitizing module instead of a model of the exact front-end electronics of a scanner, the count rate results can easily be under- or over-estimated significantly, often between 30 – 60%, or more. The software can also be prone to software bugs due to the lack of rigorous software version control (Leung 2016). Care must be exercised to ensure that the results produced by MC simulation software are valid.

Modern PET technologies

Time-of-flight (TOF) PET

TOF-PET enables the capability to localize an annihilation event along an LOR by calculating the time difference between 2 detected single events, as shown in Figure 1-7. With TOF, the effective sensitivity (in terms of image signal-to-noise ratio (SNR)) of the scanner is improved because each annihilation event is spread to a smaller number of bins along the LOR. The localization uncertainty (Δx) of an annihilation event is proportional to the coincidence timing resolution (Δt) of the scanner, using $\Delta x =$

$$\frac{\Delta t \times c}{2}$$

(Equation 1-18:

$$\Delta x = \frac{\Delta t \times c}{2} \quad \text{(Equation 1-18)}$$

where c is the speed of light.

Scintillator crystals with shorter rise and decay times (e.g. LSO and LYSO as opposed to BGO), and faster detectors and front-end electronics are essential to achieve fine timing resolution in TOF-PET.

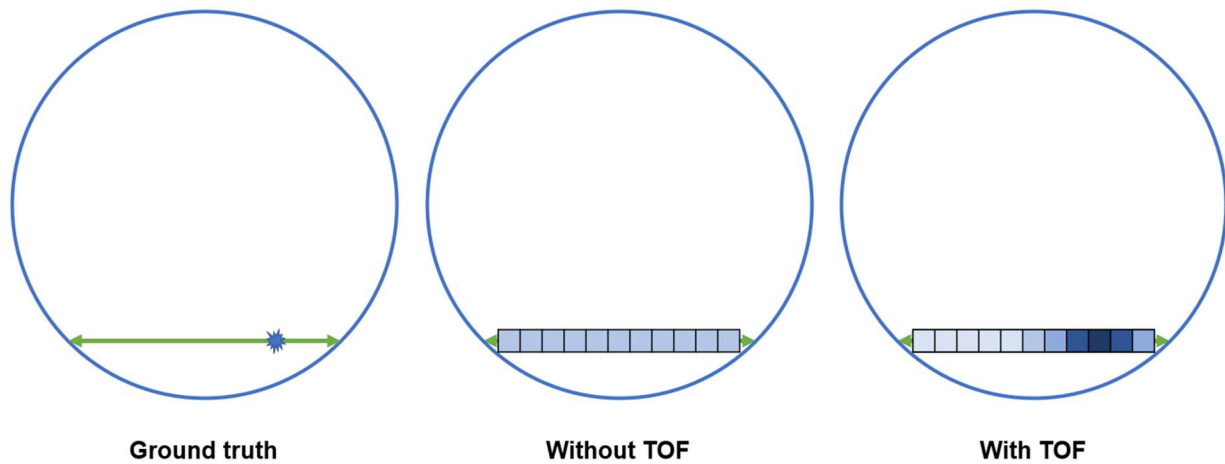


Figure 1-7. Determining the location of the annihilation event along the LOR (in green). (Left) ground truth. (Center) Without TOF information, where every bin along the LOR is given equal weights. (Right) With TOF information, where the bins closer to the annihilation event is given heavier weights.

Depth-of-interaction (DOI) PET

The energy deposition of an annihilation photon occurs along the length of a scintillator crystal. If the depth-of-interaction (DOI) in the crystal is not known, the LORs closer to the edge of the scanner will have degraded radial spatial resolution, since the width of the LOR approaches the length of the crystals, as demonstrated in Figure 1-8. This effect is particularly more noticeable for scanners with longer crystals, and with small animal PET scanners since the object scanned is often much closer in size as the bore diameter.

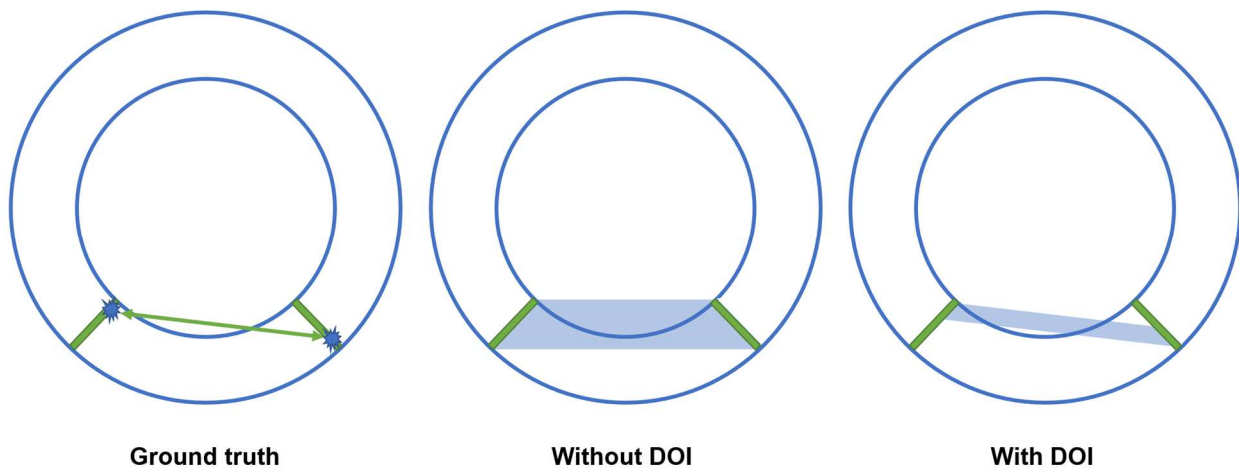


Figure 1-8. DOI effects on event localization. (Left) Ground truth, where the location of energy depositions in both scintillator crystals are known. (Center) Without DOI, where the width of the LOR is large. (Right) With DOI, where the width of LOR is small due to improved localization of energy deposition in both scintillator crystals.

DOI-capable detectors have been developed to reduce such parallax effect. Two of the most common methods involve 1) placing photodetectors on both ends of the scintillator crystals, or 2) using two scintillator materials with different decay time properties, commonly known as phoswich (as in sandwich). The first method requires the photodetector on the inside surface of the scanner to be as thin as possible to minimize attenuation effects, while the second method degrades the TOF resolution of the scanner due to the use of scintillator materials with slower decay time properties.

Performance and quantification in PET

The National Electrical Manufacturers Association (NEMA) publishes standard procedures for evaluating the performance of PET scanners. To date, the NEMA NU 2-2018 is the latest standard for evaluating clinical PET scanners. The goal of the NEMA NU 2 standard is to provide a unified method for comparison between various PET scanners of similar types, specifically for clinical PET scanners that have an axial FOV of 65 cm or less. The tests include 1) spatial resolution, 2) count rate performance, 3) sensitivity, 4) quantitative accuracy, 5) image quality, 6) TOF resolution, and 7) PET/CT co-registration accuracy and are summarized below.

Spatial resolution

The spatial resolution at the center of a PET scanner can be categorized into 1) intrinsic system spatial resolution, and 2) measured system spatial resolution. The intrinsic system spatial resolution (R_{sys})

of a PET scanner is estimated using $R_{sys} \approx \sqrt{R_{int}^2 + \Delta_{nc}^2 + \Delta_{pos}^2}$ (Equation

1-19:

$$R_{sys} \approx \sqrt{R_{int}^2 + \Delta_{nc}^2 + \Delta_{pos}^2} \quad (\text{Equation 1-19})$$

where R_{int} is the intrinsic spatial resolution of a PET detector element (i.e. scintillator crystal), which is half the width of the detector element; Δ_{nc} is the spatial blurring due to photon non-collinearity, and Δ_{pos} is the spatial blurring due to positron range. This equation assumes all resolution components are Gaussian in shape.

The measured system spatial resolution (as defined by the NEMA NU 2-2018 protocol) is based on the FBP reconstructed line profiles of a ^{18}F or ^{22}Na point source that is less than or equal to 1 mm in the radial, tangential, and axial directions. The point source is measured at various radial and axial offsets, and the FWHM and FWTM resolutions of each direction are reported for this assessment. One consideration to note is that the NEMA NU 2 spatial resolution assessment does not make assumptions regarding the shape of the line profile measurements.

Count rate performance

To determine the count rate performance of a PET scanner, the NEMA NU 2-2018 protocol specifies the use of a 203 mm diameter x 700 mm long polyethylene cylinder with a 45 mm radial offset line source of equal length positioned at the center of the PET scanner. A series of decay measurements are performed to obtain the count rate data. The count rate performance of a PET scanner is typically characterized by its noise-equivalent count rate (NECR), defined using $NECR = \frac{R_{true}^2}{R_{true} + R_{scatter} + kR_{random}}$

(Equation 1-20 ([NEMA NU 2-2018](#)):

$$NECR = \frac{R_{true}^2}{R_{true} + R_{scatter} + kR_{random}} \quad (\text{Equation 1-20})$$

where R_{true} , $R_{scatter}$, and R_{random} are the true, scattered, and random coincidence rates, respectively. k is a randoms multiplier such that $k = 1$ applies for random estimation using detector single event rates, and $k = 2$ applies for random estimation using the delayed coincidence channel. In practice, however, it is generally accepted that $k = 1$ is used universally, provided that the method of randoms subtraction is reported.

The NECR metric is widely accepted as a count rate performance metric when comparing different PET scanners. Modifications of the NECR metric have been proposed to provide a more appropriate estimate of the effective count rate performance of a PET scanner by accounting for the image SNR gain from TOF ([Conti 2005](#)).

Sensitivity

The sensitivity of a PET scanner reflects the probability that an annihilation photon pair emitted from the scan subject is detected. In a Monte Carlo simulation, the simplest way to measure sensitivity is to determine the ratio of the true coincidence events detected to the number of annihilation photon pairs emitted from a generic point source. The NEMA NU 2-2018 protocol, on the other hand, utilizes a 700 mm long line source and 5 aluminum sleeves to measure the system sensitivity and to generate an axial sensitivity profile.

Quantitative accuracy and image quality

PET is inherently a quantitative imaging technique that, if implemented correctly, provides images that accurately reflect the quantitative distribution of radiotracer in the body. To determine the quantitative accuracy of a PET scanner, the same dataset from the NEMA NU 2-2018 NECR measurement is used to calculate the relative count rate error of the PET scanner using reconstructed PET images.

In addition, a NEMA NU 2 image quality (IQ) phantom may be positioned at the center of the PET scanner, axially adjacent to a NEMA NU 2 scatter phantom. The contrast recovery coefficient (CRC) and background variability of the 6 hot spheres and warm background of the IQ phantom may be calculated to determine the quantitative accuracy of the PET scanner.

Conceptually, the quantitative accuracy of a PET scanner can simply be evaluated based on the total image-derived activity of the entire image volume to the known total activity in the FOV of the PET scanner. However, conventional PET scanners are typically much shorter than a human subject, and therefore such method is only applicable to short phantoms and is not a commonly assessed metric. ROI-based analysis that evaluates the bias relative to the known radioactivity concentration in phantoms are more common.

Time-of-flight resolution

The TOF resolution of a PET scanner reflects the uncertainty in the arrival times of the annihilation photons that form a coincidence event, which in turn, reflects the uncertainty in the localization of an annihilation event along an LOR. The NEMA NU 2-2018 protocol utilizes the dataset acquired from the NECR measurement to determine the TOF resolution of a PET scanner.

PET/CT co-registration accuracy

The NEMA NU 2-2018 PET/CT co-registration accuracy test is created to ensure that the CT and PET data is spatially aligned to ensure accurate attenuation correction and anatomical correlation of the resulting PET/CT images. Weights and PET/CT fiducial markers are placed along the scanner bed prior to data acquisition to simulate the weight of an adult human subject.

Energy resolution

The energy resolution of a PET scanner is defined by the ratio of the FWHM of the photopeak to the photopeak of the radioactive source used. A better energy resolution enables the use of a narrower energy window to discriminate scattered photons.

Applications in PET

To generate clinically useful PET images, a radionuclide is attached to a molecule of biological interest and is injected into the subject prior, or immediately after the start of a PET acquisition (for dynamic PET imaging). The choice of radionuclide used for labeling a molecule depends partly on the half-life required, which commonly ranges between seconds to days. Common radionuclides used in PET include ^{11}C , ^{13}N , ^{15}O , ^{18}F , ^{68}Ga , ^{89}Zr , and more.

Biology of ^{18}F -FDG

^{18}F -FDG (^{18}F -fluorodeoxyglucose) is a radioactive analog of glucose, where the hydroxyl group in the C-2 position of the glucose molecule is substituted with an ^{18}F radionuclide, which is produced by proton bombardment ^{18}O - H_2O in a cyclotron. The structures of glucose and ^{18}F -FDG are shown in Figure 1-9. ^{18}F -FDG is by far the most common radiotracer used in oncology PET applications because tumor cells tend to exhibit an increased uptake of glucose over healthy tissues ([Warburg 1927](#)), and its unique aspect in that it is taken up by the cells with membrane glucose transporters (GLUT), then phosphorylated inside the cell by hexokinase, but is not further broken down since it is missing the hydroxyl group required for glycolysis. This effectively “traps” the ^{18}F -FDG in the cells, which enables the possibility of static PET imaging in humans. Combined with a reasonably long radioactive half-life, this makes ^{18}F -FDG a suitable tracer for oncology PET applications. The voxel intensity in an ^{18}F -FDG PET image reflects the level of radioactivity concentration of ^{18}F -FDG, which in turns reflects the level of glucose metabolism in cells and is therefore used as a biomarker for oncology staging, for example.

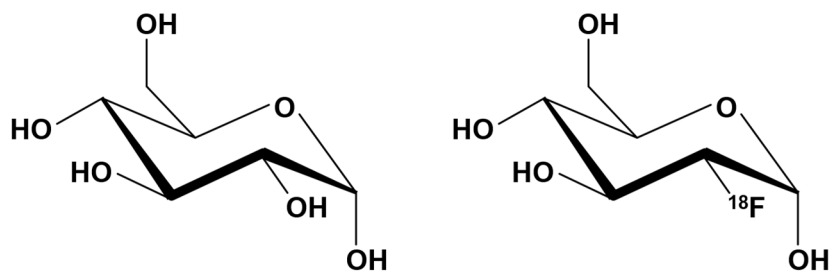


Figure 1-9. (Left) A glucose molecule. (Right). An ^{18}F -fluorodeoxyglucose molecule.

Many more PET radiotracer compounds (some with different radionuclides) are also used for evaluating various biological conditions of a human subject. Some examples include ^{18}F -fluciclovine, which is used to detect prostate cancer recurrence ([Bach-Gansmo 2017](#)); ^{11}C -UCB-J is used in brain PET imaging to study Alzheimer's disease ([Nabulsi 2016](#)); ^{82}Rb -chloride is used in myocardial perfusion imaging to identify myocardial ischemia; and ^{89}Zr -VRC01 is used for assessing the biological burden of HIV-infected individuals ([Vera 2020](#)).

Dynamic PET imaging

The concept of dynamic imaging originated from the need to develop a tracer kinetic model that reflects the underlying biochemical and physiologic mechanisms in human as well as in animal subjects. A typical dynamic PET study involves acquiring data beginning at the bolus injection phase and monitor the radiotracer distribution over a period (typically for 60 min). A time series of reconstructions are performed to obtain a movie of tracer distributions, and ROIs are drawn at specific locations (e.g. organs) to determine the changes in radiotracer concentration over time. The information is used to determine various kinetic parameters that help understand the biological functions in the body.

Typically, 2- and 3-compartment models are used to model specific biological mechanisms of interest. Using ^{18}F -FDG as an example, a 3-compartment model is used to model glucose metabolism and is shown in Figure 1-10. In the figure, 4 parameters are shown: K_1 , k_2 , k_3 , and k_4 . K_1 and k_2 represents the influx and efflux rates of ^{18}F -FDG between blood and tissue, k_3 represents the rate of phosphorylation of ^{18}F -FDG, and k_4 represents the rate of dephosphorylation of ^{18}F -FDG-6- PO_4 , which is typically considered to be negligible. While the dynamic image reconstruction protocol (in terms of frame lengths) depends on

the specific radiotracer used, a typical protocol uses shorter time frames at the start of the acquisition (in the order of seconds), to time frames in the order of minutes near the end of the acquisition.

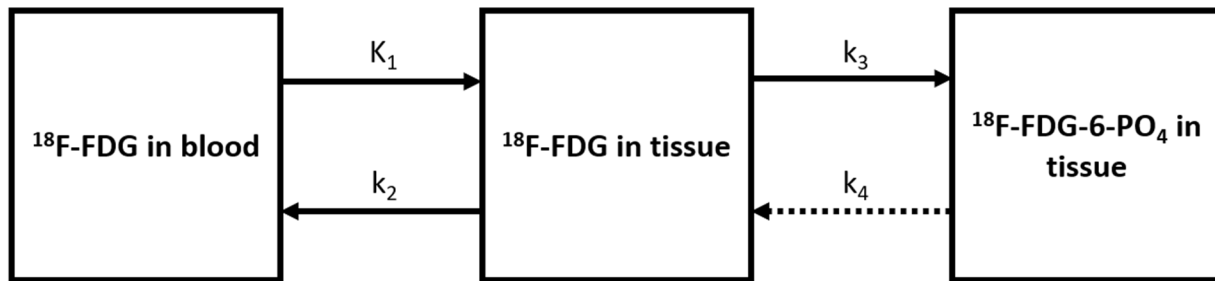


Figure 1-10. A 3-compartment model of ^{18}F -FDG.

The accuracy of determining the kinetic parameters heavily depends on the quantitative accuracy of the dynamic PET images.

Limits on conventional PET imaging

Conventional PET scanners suffer from low system sensitivity due to the limited axial FOV (~20 cm), detecting less than 1% of annihilation photons emitted from the human body. To detect enough coincidence events for image reconstruction, adult human subjects often are subjected to an average of 370 MBq ^{18}F -FDG injection and a total scan time in the order of 20 minutes. This precludes repeated PET studies of healthy adult humans as well as radiation-sensitive populations (such as pediatric patients) due to concerns regarding long-term radiation effects. Late time point studies (after several half-lives of the radiotracer) are also not feasible since the level of radioactivity remaining in the subject is going to be insufficient for a conventional PET scan. As a result, the dynamic range of a conventional PET scanner is limited.

The limited axial FOV also means that to image the entire human subject, or from the base of the skull to mid-thigh for whole-body PET studies, the subjects are positioned on the scanner and are stepped through the scanner during data acquisition. This has several implications. First, the acquired PET data may not be suitable for system-level kinetic modeling since the images from different bed positions do not belong to the same time frame, which may be ill-suited during the initial radiotracer uptake phase, or for tracers with fast kinetics, where acquiring synchronized image data for multiple

organs is required. One way to overcome this limitation is to stagger the acquisition to increase the number of sampled time points for each bed position with multiple bed passes ([Karakatsanis 2013](#)), at the expense of increased statistical noise (due to the reduced number of detected counts per time frame). Second, motion artifact may become more prominent near the image boundaries of different bed positions and may be problematic if the ROIs lie between bed positions. Lastly, outside FOV scattered and random coincidence events may make scatter and random corrections more challenging.

Research efforts to improve the sensitivity of a PET detector typically involved the development of new photodetectors, scintillator crystals and front-end electronics. Despite the incremental improvements made over the years, the axial FOV of a PET scanner remains the major roadblock to large improvements in overall scanner sensitivity.

Emergence of total-body PET

The concept of building a long axial FOV PET scanner is not new. Several studies were conducted over the years to evaluate the potentials of total-body PET, however the level of commercial interest to market a total-body PET scanner remains low. Since the cost of a PET scanner scales relatively linearly with the volume of scintillator material, a 2 m long PET scanner (which covers the entire adult human) would cost roughly an order of magnitude more than a conventional 20 cm long PET scanner, making it cost-prohibitive for widespread adoption.

The consistent level of research interest for total-body PET, on the other hand, led to the formation of the EXPLORER consortium in 2011. The EXPLORER consortium is a multi-institutional consortium established with the goal to develop the world's first 2 m long total-body PET scanner. The EXPLORER total-body PET scanner is designed to overcome the challenges that conventional PET scanners cannot address, which enables new possibilities in a wide variety of biomedical applications. With the massive sensitivity gain of the EXPLORER total-body PET scanner since the entire adult human can be imaged simultaneously, the count-limited nature of PET is significantly improved. The 40-fold increase in effective sensitivity enables 1) improved image quality, 2) reduced scan time, 3) reduced radiation dose, 4) late time point imaging, and 5) system-level modeling of the human body. This ultimately led to the \$15.5M funding approval from the National Institutes of Health (NIH) in 2015 to build

the world's first total-body PET scanner. A commercial, small-scale EXPLORER scanner (i.e. the Mini-EXPLORER II) for companion animal imaging was built 2 years after the NIH funding approval. The first FDA 510(k) cleared EXPLORER scanner was installed and in clinical use since 2019, featuring 564,480 LYSO scintillator crystals, 53,760 SiPMs, and an 8-node computational cluster (with an extra [hot spare](#) node) for PET data storage and image reconstruction. PET images acquired using the EXPLORER scanner has demonstrated the potentials in total-body PET imaging, with images acquired with ~20 MBq ^{18}F -FDG injected in healthy adult human subjects, delayed time point ^{18}F -FDG imaging up to 12 h post-injection, as well as sub-second dynamic PET images ([Badawi 2019](#), [Zhang 2020a](#)).

Current challenges in total-body PET imaging

The latest advancements in PET detector technology and the relative affordability in high-performance computing has enabled total-body PET imaging to be actualized in the clinical environment. However, several challenges (in addition to scanner costs) unique to total-body PET imaging continue to limit its widespread adoption. Some of the challenges include: 1) computational demands, 2) storage needs, 3) infrastructure, and 4) data corrections.

Since data from 92 billion LORs are collected for the EXPLORER scanner, the required size of a sinogram approaches 700 GiB, making sinogram-based image reconstruction impractical. Therefore, list-mode image reconstruction is implemented. Since the time required for list-mode image reconstruction is dependent on the number of coincidence events collected, the computational demands and storage space required for EXPLORER datasets are much higher than that of conventional PET scanners. A 370-MBq ^{18}F -FDG 60-min dynamic PET study on average occupies > 1 TiB of storage space. This massive computational burden necessitates a robust computational infrastructure that seamlessly and reliably handles data processing, image reconstruction and data sharing. Also, with the massive number of PET detectors and axial FOV coverage involved, the demands for stable quantification across a wide activity range may put more burden on the PET data corrections. In addition, the logistics required to calibrate and maintain a scanner of such scale is not trivial. Finally, new applications that were previously not addressable with conventional PET scanners require careful planning to maximize the utility of total-body PET.

Project aims

The work described in this dissertation provides portions of the foundation for the research and development in total-body PET, particularly for the EXPLORER PET program, with modularity and flexibility in mind. Chapter 2 details a first attempt at characterizing the quantitative accuracy of PET in a long axial FOV environment under a wide range of conditions previously not achievable with conventional PET scanners, in addition to standard quantitative PET measurements, using the EXPLORER total-body PET scanner.

Chapter 3 assesses the relationship between TOF-reconstructed image SNR and total-body NECR using the EXPLORER scanner. The NECR equations for non-TOF and TOF scanners were modified to handle list-mode PET data. The scatter component was estimated using a highly parallelizable, Monte Carlo scatter correction implementation for an in-house total-body PET reconstruction platform using continuous water density materials. The implementation is based on the SimSET Monte Carlo simulation package and can be reconfigured for other conventional PET scanner geometries.

Chapter 4 details the development of a high-performance, multi-threaded, software-based coincidence processor designed for the EXPLORER total-body PET scanner to handle its massive incoming single event data rates. Similar to the scatter correction implementation mentioned in Chapter 3, the coincidence processor can also be tailored for other PET scanner geometries.

Chapter 5 describes a sensitivity simulation study involving the NeuroEXPLORER (NX) dedicated brain PET scanner using a customized Monte Carlo simulation platform based on GATE. The framework developed as a result of the study becomes the primary simulation infrastructure for the NX PET program, a project that stemmed from the EXPLORER PET program.

Finally, Chapter 6 summarizes the work described in this dissertation and discusses possible improvements in total-body PET quantification and computation, as well as potential ways to accelerate the adoption of total-body PET in the clinical setting. The future of total-body PET is also discussed.

Chapter 2 – Quantitative accuracy in total-body PET using the EXPLORER PET/CT scanner

Introduction

Absolute quantification of regional tissue radioactivity concentration is a hallmark of positron emission tomography (PET), and the quantitative accuracy of the reconstructed images is a critical parameter-of-interest across both clinical and research imaging applications. Accurate quantification is essential for kinetic modeling, lesion characterization, as well as measuring tumor response to therapy ([Carson 2003](#), [Wahl 2009](#)). Quantitative accuracy in PET is affected by a complex interplay of factors, from the scanner calibration to the PET data corrections and image reconstruction parameters ([Badawi 1999](#), [Brasse 2005](#), [Johansson 2007](#), [van Velden 2009](#), [Lockhart 2011](#), [Walker 2011](#), [Jian 2015](#)), along with application-dependent factors such as the total radioactivity in the FOV of the scanner, activity distribution, and patient habitus ([Boellaard 2009](#), [Boland 2009](#), [El Fakhri 2009](#)).

The emergence of total-body PET imaging with a long axial field-of-view (FOV) system (e.g. 194 cm in the EXPLORER PET/CT scanner ([Spencer 2021](#))) enables the entire adult human to be imaged in a single bed position ([Badawi 2019](#)), and provides approximately a 40-fold increase in scanner sensitivity for whole-body imaging compared to conventional PET systems with 15 – 30 cm axial FOV that comprise the majority of PET systems available for human imaging ([Bettinardi 2004](#), [Teräs 2007](#), [Bettinardi 2011](#), [Jakoby 2011](#), [Poon 2012](#), [Miller 2015](#), [Rausch 2019](#), [van Sluis 2019](#)). The sensitivity gain and the long axial FOV aspect of total-body PET provides increased image signal-to-noise ratio (SNR) and widens the dynamic range accessible to PET, creating new clinical research and healthcare opportunities in: 1) reduction of radiation dose ([Badawi 2019](#), [Liu 2021](#)), 2) dynamic imaging with short image frame durations ([Zhang 2020a](#)), 3) delayed or low-activity imaging ([Berg 2020](#), [Vera 2020](#)), and 4) kinetic modeling of the entire human body ([Feng 2020](#), [Wang 2020](#), [Zhang 2020b](#)).

While these and other imaging regimes are now possible with total-body PET imaging from a SNR perspective, they introduce challenging conditions for accurate quantification. For instance, the non-linearity and non-negativity constraints imposed by iterative image reconstruction can make quantification challenging when there are few coincidence events contained in the image (e.g. in low-dose, short frame durations, and delayed imaging). In addition, the variations in count rate and scatter fraction across the long axial FOV can be large and rapidly changing in some imaging applications, particularly in the early

phase of total-body dynamic acquisitions. The scanner also has approximately an order of magnitude greater volume of scintillator material ([Jakoby 2011](#), [Spencer 2021](#)) and, when combined with an increased axial acceptance angle, leads to higher ^{176}Lu background count rate than shorter conventional PET scanners. The ^{176}Lu background (7.5 Mcps singles and 93 – 94 kcps coincidence background rates for the EXPLORER scanner) comprises the bulk of the PET data at very low levels of radiotracer activity.

The goal of this work is to evaluate the quantitative accuracy of the EXPLORER scanner in a variety of conditions that encompass existing and potential imaging applications, including total-body high-dose dynamic imaging and ultralow-dose imaging within the dynamic ranges as depicted in Figure 2-1. To that end, we devised a set of total-body specific phantom and human measurements to characterize the quantitative accuracy of the EXPLORER scanner across a wide range of activity and count rate scenarios. These measurements included global quantification bias assessments using an extended NEMA NU 2 scatter phantom and a long uniform water cylinder scanned at various activity levels and scan durations, in addition to the more traditional methods of evaluating regional bias and variability in regions-of-interest (ROIs) by simultaneously imaging three NEMA image quality (IQ) phantoms.

In addition to phantom evaluations, a set of healthy human studies performed on the EXPLORER scanner at the EXPLORER Molecular Imaging Center (Sacramento, CA, United States) were used to measure global quantitative bias. Evaluating the absolute quantitative accuracy in human subjects is a challenging task due to the absence of ground truth radioactivity concentration in different organs. Furthermore, since conventional PET scanners capture the signal from only a 20 – 30 cm axial region at a time, validating absolute PET quantification relative to the total injected radioactivity in human subjects is difficult and can be prone to error, since there is no direct knowledge of the total radioactivity inside the axial FOV of the scanner. Therefore, the evaluation of quantitative accuracy in PET has, for the most part, been limited to ROI analysis in shorter phantoms with known radioactivity concentrations, but which do not represent realistic conditions for human imaging, which involves significant variations in attenuation, scattering, and radioactivity distribution. An exception is the work of [Lodge 2021](#) where the accuracy of a conventional PET/CT scanner was assessed in the descending thoracic aorta by means of venous sampling. Here, we make use of the total-body coverage provided by the 194 cm long EXPLORER

scanner to evaluate the absolute quantitative accuracy in human dynamic imaging studies since all of the radioactivity is always confined within the FOV throughout the PET acquisition shortly after radiotracer injection.

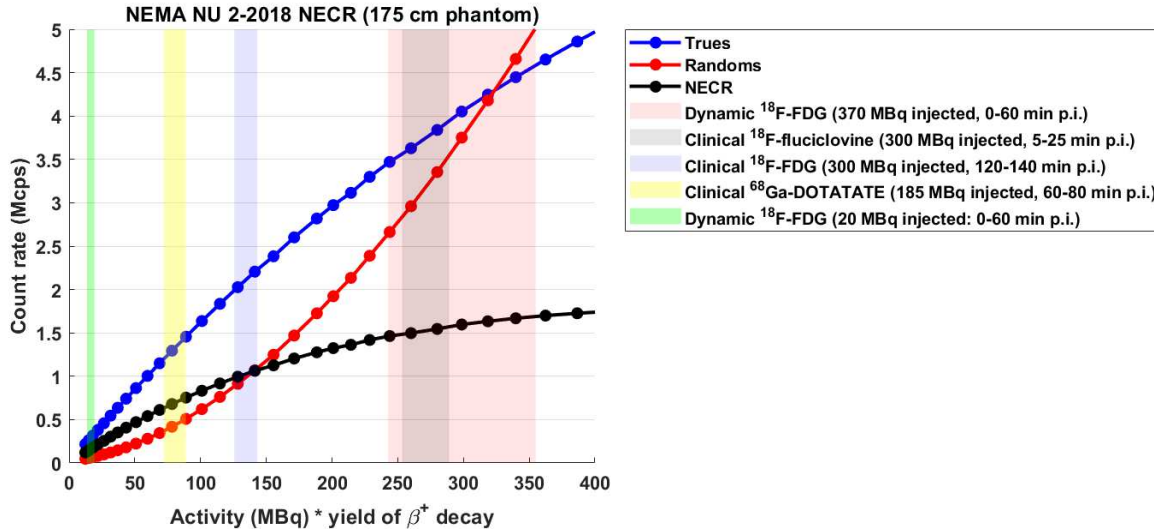


Figure 2-1. Range of count rates encountered by the EXPLORER scanner (throughout the PET acquisition) in various clinical and research tasks. The count rates were estimated based on the NEMA NU 2-2018 NECR performance assessment using an extended, 175 cm NU 2 scatter phantom. Note: the activity at peak NECR is 528 MBq, and “p.i.” stands for post-injection.

Methods

System parameters

The 194 cm long EXPLORER PET/CT scanner consists of 8 PET scanner units, with a ring diameter of 786 mm. There are 24 detector modules in each scanner unit. Each module contains 5 x 14 (transaxial x axial) detector blocks, where each block contains 7 x 6 (transaxial x axial) scintillator crystals (each 2.76 x 2.76 x 18.1 mm³). The time-of-flight (TOF) resolution of the system is 505 ps, and the spatial resolution of the system is ≤ 3.0 mm full width at half maximum (FWHM) near the center of the axial FOV of the scanner. The system utilizes a scanner unit-based variable time window (4.5 – 6.9 ns) and allows each unit to form coincidence events with up to a maximum unit difference of 4, which corresponds to a maximum axial acceptance angle of 57.0°. The energy window is 430 – 645 keV. Additional information regarding the system performance is reported in [Spencer 2021](#).

Image reconstruction

The PET images were reconstructed in a research-only environment, using the vendor-provided list-mode time-of-flight, ordered-subset expectation-maximization (TOF-OSEM) reconstruction platform (a clinical release R001.2-based, stand-alone hardware and software environment extended with customizable offline reconstruction and other research functionality) installed on in-house computational hardware. In this software environment we were provided direct access to all intermediate reconstruction files and PET data correction files (e.g. normalization and dead-time lookup tables (LUTs)). This enabled us to investigate the effects from changes made into individual correction files on the quantitative accuracy of the reconstructed images without making changes to the underlying reconstruction and data correction algorithms. As a result of this investigation, updated normalization and dead-time LUTs provided by the vendor were used for this work. The results presented below utilized the same data correction parameters and these parameters were not fine-tuned for individual studies. To maximize computational efficiency as well as to minimize effects from varying reconstruction parameters, only one set of reconstruction parameters was employed for all experiments: the images were reconstructed with 4 iterations, 20 subsets, and with 4 mm isotropic voxels in a 150 x 150 x 486 image matrix. Resolution modeling (i.e. point spread function (PSF)) was not included, and no post-reconstruction smoothing was applied to the images. All other PET data corrections were applied throughout the studies, including corrections for scattered and random coincidences, attenuation, dead-time, normalization, and radioactive decay. Random coincidences were estimated for each block-pair using a delayed coincidence channel. Scattered coincidences were estimated for each dual-block (7 transaxial x 12 axial crystals) pair using Monte Carlo simulations independently for each image frame. Dead-time correction was performed using a non-paralyzable model based on the detector block singles rates from a high-count scan of a long acrylic uniform water cylinder (16.5 cm outer diameter, 15 cm inner diameter, 210 cm long) filled with approximately 500 MBq of ^{18}F -FDG at the start of the scan. Attenuation correction factors (ACFs) were obtained from a low-dose co-registered CT image acquired for each study. Prior to calculating ACFs, the CT images were pre-processed using a custom software patch to remove artifacts that manifested at the edge of the FOV, which were found to introduce quantitative biases. The low-intensity CT artifacts were

present in the form of an annulus with an inner diameter of 500 mm and an outer diameter of 700 mm. The extent of their effects on the quantitative biases in the PET images depended on the size of the object as well as its position relative to the FOV of the CT. The scanner manufacturer has implemented a software fix that will be released in the next version of the clinical software. Normalization factors (crystal efficiency and plane efficiency) were obtained using a 20 cm diameter x 30 cm long ^{68}Ge uniform cylinder that was stepped across the axial FOV for 45 min. The reconstruction dose calibration factor used for absolute quantification was obtained using a 20 cm diameter x 30 cm long ^{18}F -FDG uniform cylinder positioned at the center of the scanner. The dose calibrator (Capintec CRC-55tR) used for the study was calibrated daily in accordance with the recommended calibration procedure from the owner's manual.

Accuracy of count rate corrections

The 70 cm NEMA NU 2 scatter phantom and a 175 cm extended version of it were used to evaluate the dependence of count rate on the quantitative accuracy. The standard 70 cm scatter phantom was assembled using four 17.5 cm polyethylene phantom sections, while the extended phantom consisted of ten sections. Each phantom was positioned at the center of the scanner, and a decay series of acquisitions over 10 h were acquired for each phantom. Initial ^{18}F -FDG activities were 370 MBq for the 70 cm phantom, and 441 MBq for the 175 cm phantom. Both experiments were acquired until the total activity in the FOV of the scanner was < 10 MBq. The NEMA NU 2-2018 accuracy test was performed for both the 70 cm phantom using image slices within the central 65 cm of the axial FOV, and the central 170 cm axial FOV for the 175 cm phantom. The quantitative accuracy was assessed based on the relative percent true error in each image slice.

Uniform phantom

A long acrylic uniform water cylinder (16.5 cm outer diameter, 15 cm inner diameter, 210 cm long) filled with ^{18}F -FDG was positioned at the center of the scanner. List-mode PET data were acquired at five time points over 10 h, from 474 MBq to 17 MBq in the FOV of the scanner. The scan duration for each acquisition was 60 min, and a series of 5-min dynamic PET images (12 time frames total) were reconstructed. The axial uniformity of the scanner was evaluated based on the normalized mean values

for each image slice within a 130 mm diameter circular ROI concentric to the phantom, using the 0 – 5 min image slices from each of the five datasets. The global quantitative bias was evaluated by comparing the activity sum in the image to the known activity in the axial FOV of the scanner with dynamic (5-min x 12 time frames) reconstructed images.

Regional bias and variability

The triple NEMA IQ phantom evaluation was based on the NEMA NU 2-2018 IQ assessment, with a 4:1 hot-to-warm background radioactivity concentration. In this modified protocol, 3 IQ phantoms and a NU 2 scatter phantom were filled according to the NEMA NU 2-2018 protocol and were positioned as shown in Figure 2-2, with the third IQ phantom abutting the NU 2 scatter phantom and positioned near the center of the scanner. To yield constant activity concentrations in the three IQ phantoms, a single radiotracer dose was diluted in a one-liter saline bag and was used to fill all the hot spheres, and another single radiotracer dose was diluted in 33.4 L of water and was used to fill the background volume in all three phantoms. Given the small variations in total volume of the three phantoms, this resulted in a total activity of 42.9, 42.7, and 43.4 MBq in the first, second, and third IQ phantoms, respectively. Data were acquired over 12 h, with six 1-h data acquisitions, from 217 MBq to 2 MBq of ¹⁸F-FDG in the FOV of the scanner. An ROI-based analysis was performed by assessing the bias of the warm background of each IQ phantom using 30-min static reconstructions. On every slice of the central 10 cm axial length of the phantom (27 slices), twelve circular ROIs (37 mm diameter) were drawn on the warm background region of each IQ phantom ([Spencer 2021](#)). This fulfills the NEMA NU 2-2018 background ROI placement criteria for evaluating the quantitative biases of the ROIs relative to the known warm background activity concentration.

Also, to assess the effects of the total number of counts on the bias and noise of the reconstructed images, 30 mm diameter spherical volumes-of-interest (VOIs) were drawn on the 37 mm hot sphere and warm background of each IQ phantom. The VOI for the warm background was placed in the proximity of the 28 mm and 37 mm spheres, at approximately 107 mm radial offset from the center of the phantom. Two types of images were used for this analysis: (1) 30-min static images at each time point, and (2) re-sampling of 60-min data (and portions of it) into 30 dynamic images that contained

equivalent number of counts in each time frame, similar to the re-sampling strategy described in [Jian 2015](#).

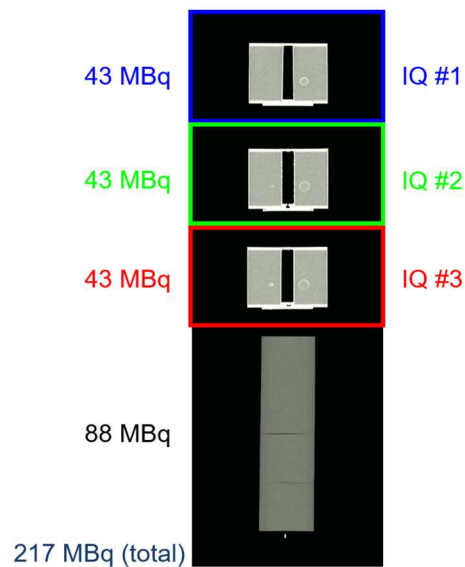


Figure 2-2. The position and activity of each phantom in the triple NEMA IQ phantom assessment.

Dynamic quantification in humans

Dynamic images from two representative research human subjects injected with ^{18}F -FDG were used to evaluate the global quantitative accuracy in human subjects over the scan duration at two activity levels: 370 MBq (80.8 kg, 165.1 cm) and 21 MBq (84.4 kg, 170 cm) injected activity. The studies were IRB-approved (#1341792), and the subjects provided informed consent. The subjects were placed in a supine position with their hands to the side of their bodies. Data acquisition began immediately following radiotracer injection in the antecubital vein. The scan duration was 60 min. For this evaluation, a dynamic reconstruction framing protocol that consists of 66 frames (30 x 2 s, 12 x 10 s, 6 x 30 s, 12 x 120 s, and 6 x 300 s) was used. Since the injected activities were completely within the FOV of the scanner, the global activity bias was evaluated by computing the percent bias of the activity sum in a total-body ROI to the known injected radiotracer activity.

Results

Count rate dependent quantitative accuracy

Figure 2-3 and Figure 2-4 show the relative percent trues error of the standard 70 cm and extended 175 cm NU 2 scatter phantoms, plotted against activity concentration, as well as the average activity in the phantom (located on the top x-axis), respectively. The mean relative trues errors for both phantoms ranged between $\pm 3 - 4\%$, from approximately 10 to 400 MBq.

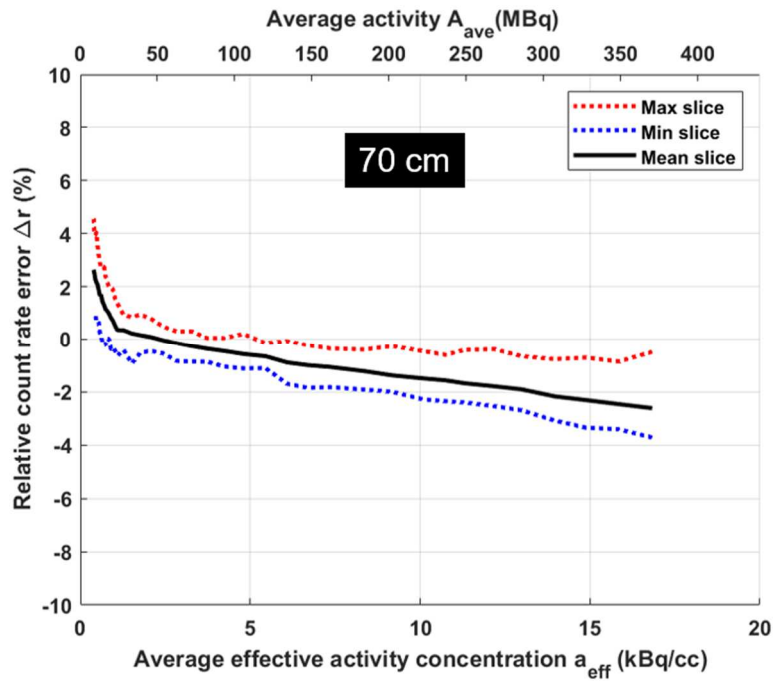


Figure 2-3. The relative trues error of the standard 70 cm NU 2 scatter phantom.

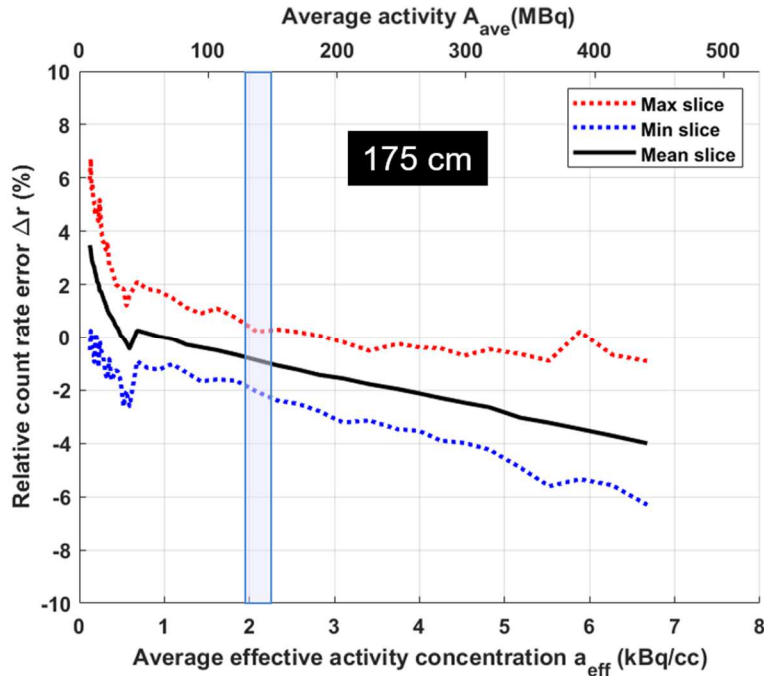


Figure 2-4. The relative true error of the extended 175 cm NU 2 scatter phantom. The shaded blue region represents the average activity throughout an clinical ^{18}F -FDG scan (~300 MBq injected; scan begins at 120-min post-injection).

Uniform phantom

Figure 2-5 shows the axial uniformity plotted against axial slice position, measured with the uniform phantom at 3 radioactivity levels, from 17 MBq to 474 MBq. The uniformity spread was $\pm 3\%$ in the central 90% axial FOV of the scanner. The normalized root-mean-square errors (NRMSE) of the central 90% of the image slices were 1.7% (17 MBq), 1.3% (151 MBq), and 1.2% (474MBq). Figure 2-6 shows the global activity bias of the uniform phantom, plotted against the activity in the FOV of the scanner. The biases ranged from 1.3% to 4.3%, from 17 MBq to 474 MBq, respectively.

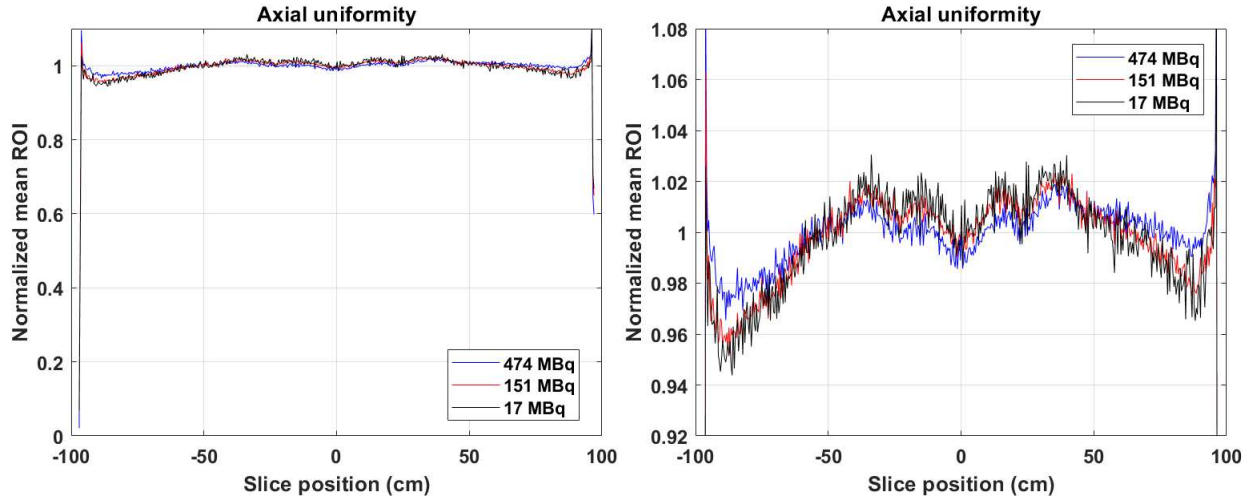


Figure 2-5. Axial uniformity of the EXPLORER scanner. (Left) The y-axis ranged from 0 to 1.1. (Right) The y-axis ranged from 0.92 to 1.08. The normalization factor was based on the ROI average of the central 90% slices.

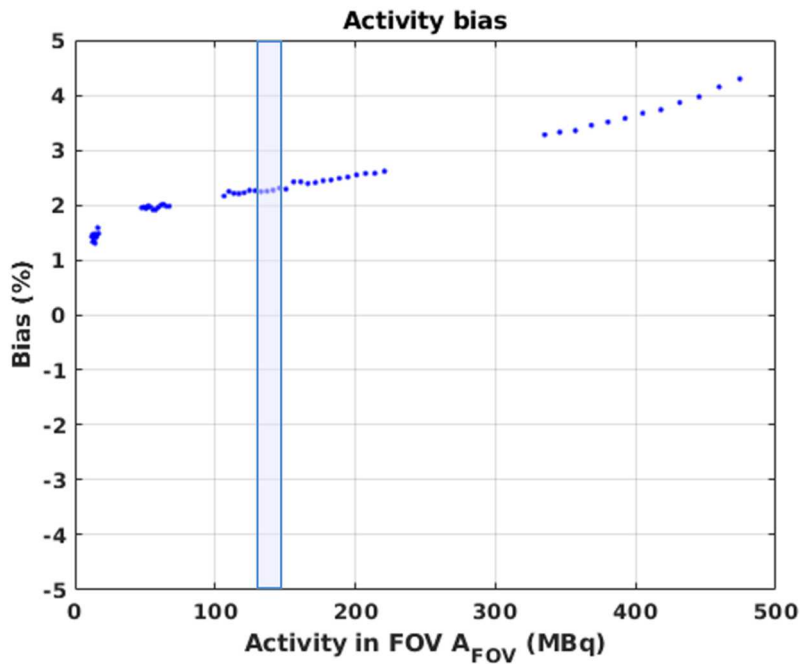


Figure 2-6. The global activity bias of the uniform phantom. The shaded blue region corresponds to the average activity throughout an EXPLORER clinical ^{18}F -FDG scan (~300 MBq injected; scan begins at 120-min post-injection).

Triple NEMA IQ phantom

Figure 2-7 shows the warm background ROI biases of the three IQ phantoms. The mean biases (from the known warm background activity concentration) of the three IQ phantoms ranged between +4%/+5%, from 22 MBq to 217 MBq. Figure 2-8 shows the box plots of the VOI biases of the 37 mm hot sphere and the background of the 3rd IQ phantom, with the effective total counts of each image (normalized to the first 30 min of the first scan) shown on the upper x-axis. The biases ranged between -5%/-3% for the hot sphere, and -1/+6% for the background, between 0.2 – 100% of effective counts.

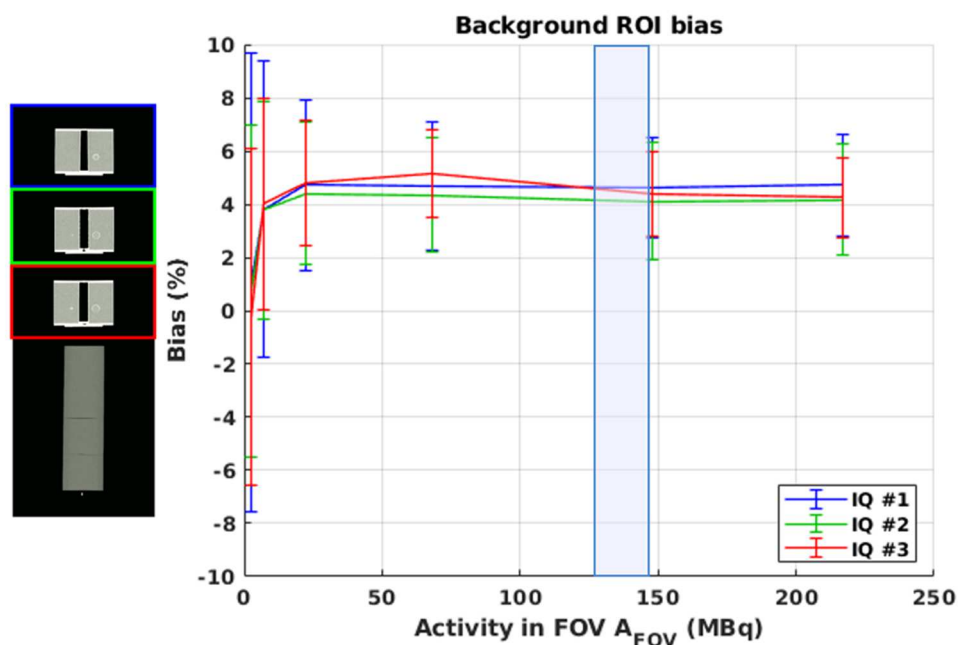


Figure 2-7. Bias (mean±SD) of the background ROIs in the 3 IQ phantoms. The error bars indicate the standard deviation (SD) of the mean bias of the 324 background ROIs analyzed for each IQ phantom. The blue shaded region represents the average activity throughout an EXPLORER clinical ¹⁸F-FDG scan (~300 MBq injected; scan begins at 120-min post-injection).

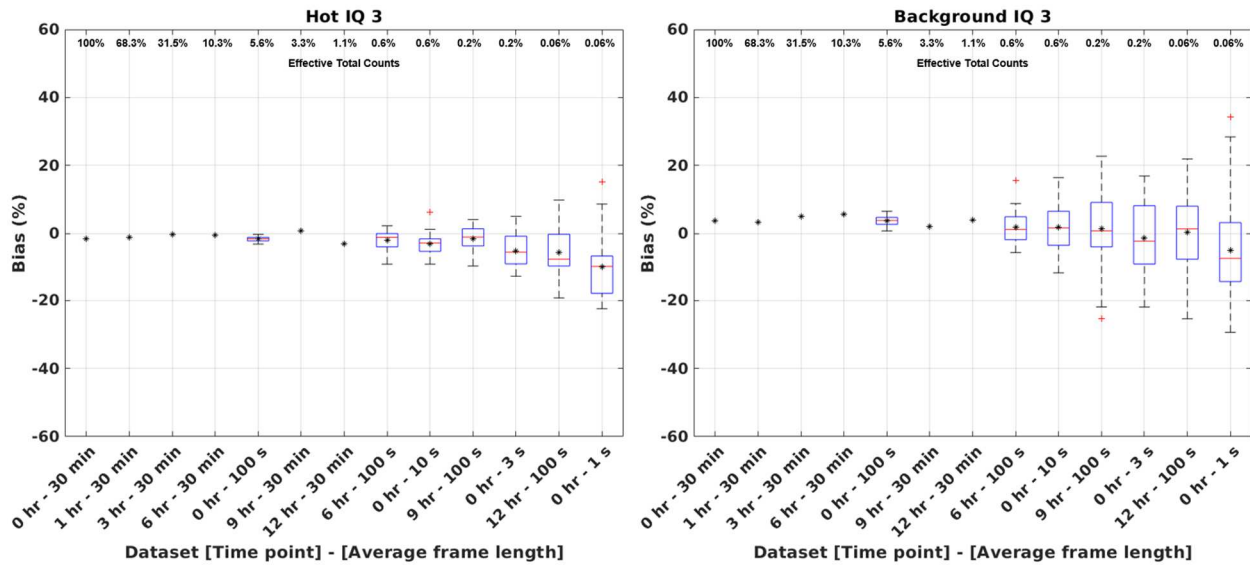


Figure 2-8. VOI biases of the (left) 37 mm hot sphere and (right) background of the 3rd IQ phantom. Each label on the x-axis represents the acquisition time point and the average frame duration of the re-sampled dataset, ordered based on the fraction of total counts of the 1st 30-min scan (as shown on the upper x-axis). Mean VOI biases are shown for all datasets using black asterisks. In the case of shorter time-frame re-sampled datasets, the mean was calculated on the 30 re-sampled dataset images, and box plots were included to show the variations among the 30 datasets.

Human subjects

Figure 2-9 shows the activity bias of the human subjects, with the uniform phantom reconstructed using the same 66-frame dynamic protocol shown as reference. For both human subjects, the bias changed quickly during the initial bolus phase before stabilizing at ~60-s post-injection with approximately -2%/+1% bias in both subjects. For the uniform phantom, the biases ranged between +1%/+4% for the 300-s frames.

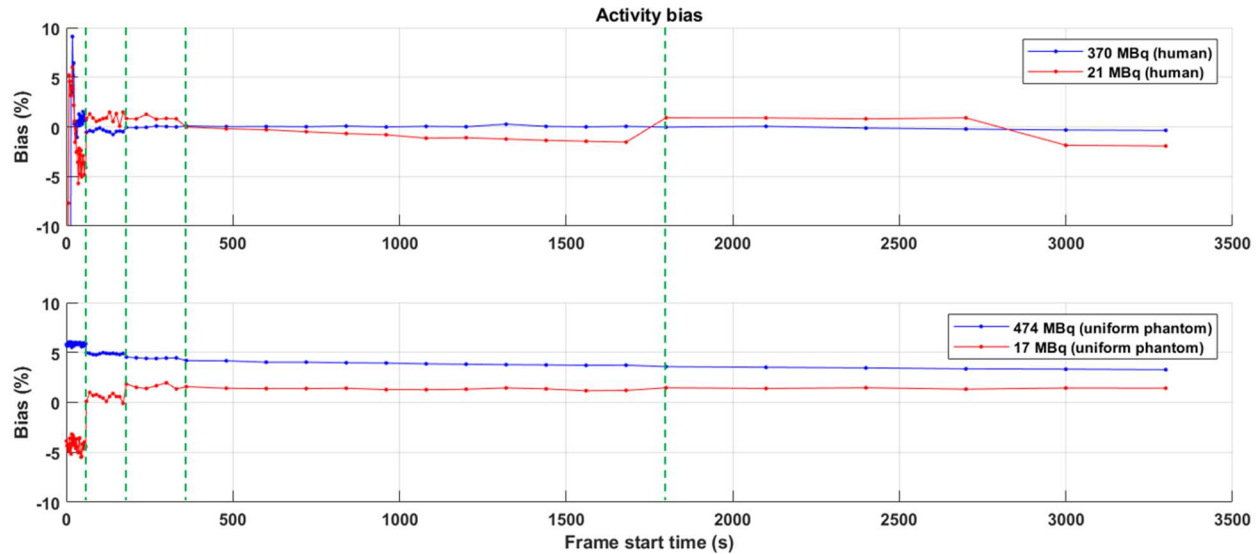


Figure 2-9. Activity bias of the (top) human subjects, and (bottom) uniform phantom using the 66-frame reconstruction framing protocol. The vertical dashed lines correspond to the time points where the frame duration changed.

Discussion

The quantitative accuracy of the EXPLORER total-body PET/CT scanner was evaluated for both static and dynamic imaging using phantom and human datasets. Overall, consistent quantification was obtained throughout most experiments, across a wide range of activity levels, activity distributions, and image frame durations. With the exception of very low activities (< 25 MBq), the total variation in the image bias was < 3% with the 70 cm NEMA NU 2 scatter phantom up to the activity at peak NECR. Three general trends were observed in the count rate quantification assessments: (1) negative correlation of relative count rate error with activity, (2) non-linear error at low activities (< 25 MBq), and (3) a transition point in error at approximately 25 MBq that is more pronounced in the 175 cm extended scatter phantom. Our investigations suggested that the activity-dependent count rate error may be related to imperfect background subtraction from the substantial presence of ^{176}Lu background in the LYSO crystals. The transition in error observed at ~25 MBq with the scatter phantoms may also be related to the total number of counts in each acquisition: to obtain sufficient temporal sampling at low activity datapoints, the acquisition times were reduced, which means even fewer counts were acquired at the low activity region. Previous literature has suggested that the number of counts in a PET acquisition may lead to biases in

images reconstructed using OSEM ([Johansson 2007](#), [van Velden 2009](#), [Walker 2011](#), [Jian 2015](#)).

Another possible cause of quantitative biases may be due to inaccuracies caused by the use of single-precision floating point calculations. These effects in total-body PET will be investigated in greater detail in future experiments. Early data from the manufacturer suggests that using double-precision floating point calculations and a reduced number of subsets in the reconstruction may result in improved quantitative accuracy at activities below ~25 MBq. For instance, the average bias of the 30 frames for the first 60 s of the uniform phantom (17 MBq) scan reconstructed with 8 iterations and 10 subsets improved the quantitative bias from -5% to +2.5%.

Uniformity assessment performed on the 2 m long cylinder phantom data showed up to $\pm 3\%$ variations across the central 90% axial FOV of the scanner. The patterns in axial uniformity were largely conserved across the range of activity investigated and were correlated with the normalization plane efficiency factors. The non-uniformities may be caused by using a shorter uniform cylinder (20 cm diameter x 30 cm long) that was stepped through the axial FOV of the scanner for normalization calibration compared to the 2 m long uniform cylinder used for this assessment, suggesting that modifications to the algorithm used for estimating the normalization factors may be appropriate. For example, inaccuracies in the estimation of normalization factors for the more oblique LORs may result in bias propagation and non-uniformities across the axial FOV, in addition to differences in attenuation and scatter between the two phantoms that is typically not a consideration in PET normalization when using a shorter phantom with less attenuation. However, the use of a 2 m long phantom is challenging in practice, largely due to its bulk and weight, in addition to potential imperfect mixing of the radionuclide.

Quantitative biases in each of the three IQ phantoms in the triple IQ experiment were stable above ~25 MBq and further demonstrates accurate and axially uniform quantification with a non-uniform radioactivity distribution. The decrease in bias at the low end of the activity may be attributed to the compounding effects of the lower total number of counts and a higher number of subsets used in the OSEM reconstruction. Also, the total activity in the FOV of the scanner in the last PET acquisition was only 2 MBq and may be responsible for the large standard deviations observed in these datapoints. In the future, a detailed assessment using various reconstruction parameters along with varying number of

iterations and subsets may further help evaluate the quantitative accuracy in total-body PET across a wide dynamic range.

For dynamic imaging, 3% variations in quantitative biases were observed in both phantoms and humans, except with shorter frame durations (< 5 s). In humans, the changing activity distribution is a confounding factor in determining the root cause of the activity biases, but not in the phantom. Thus, based on the phantom results, the changes in bias that occurred when the reconstruction frame length changed may be due to differences in the total number of counts in the image, which may impact scatter estimation. In the human subject assessment, four out of six data points in the 300-s frames of the 21 MBq human subject showed a positive bias. This may be attributed to the scatter correction since the scatter fractions reported in the DICOM headers were slightly lower for those image frames compared to the other 300-s frames. While the quantitative biases in the human subjects did not appear to be dependent on the injected activity in the latter half of the 60-min acquisition, caution should be exercised to not overinterpret the results. Other complex, physiologic factors specific to human data may come into play, such as voluntary and involuntary motion that results in misalignments between the PET and the CT images, and the initially rapid, time-varying activity distribution following the bolus injection, all of which may lead to biases that may have compounding or opposing effects. Each human subject also has a unique body habitus and activity distribution that are distinct from each other, as well as from the shape and distribution of the uniform phantom. Figure 2-10. Activity bias of 14 human subjects using the 66-frame reconstruction framing protocol. The injected ^{18}F -FDG activity ranged from 337 – 397 MBq. shows the activity bias of 14 human subjects injected with 337 – 397 MBq of ^{18}F -FDG. Utilization of an image-derived input function (IDIF) for dynamic PET kinetic modeling may mitigate the effects of the larger biases present in the shorter frames; since scatter correction is applied on a per frame basis, both the IDIF and tissue of interest may be similarly affected. The opposing effects in bias changes with shorter frame durations between the high and low activities are peculiar and may be related to the frame-based scatter estimation and/or the effect of random coincidences from the ^{176}Lu background events that comprise most of the singles and prompt coincidences at low activity. The TOF image reconstruction with approximately 500 ps FWHM resolution and a 430 keV lower energy threshold would adequately remove any true coincidences formed by the ^{176}Lu beta decay and the 307 keV gamma emissions from the total-

body ROIs. However, the background singles subtraction performed during dead-time correction is subject to detector drifts and therefore may impact the quantitative accuracy at very low activity levels. These are all a subject for future investigations. The small positive bias of the uniform phantom with higher activity may be attributed to the count rate-dependent variations in the energy and/or TOF calibrations, in addition to the different object geometry compared to that used for scanner calibration, which further demonstrates the necessity for highly accurate physics corrections.

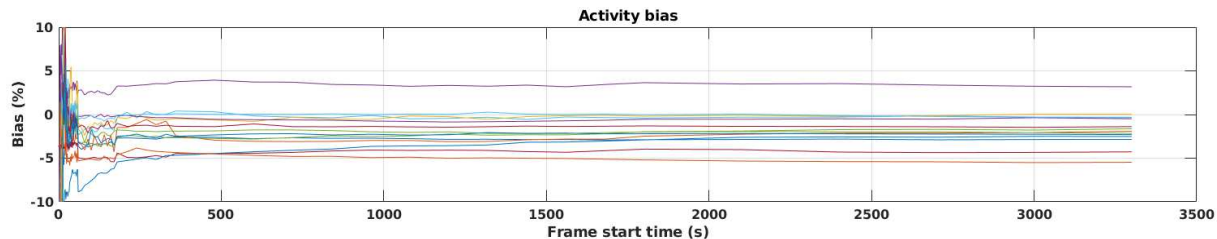


Figure 2-10. Activity bias of 14 human subjects using the 66-frame reconstruction framing protocol. The injected ^{18}F -FDG activity ranged from 337 – 397 MBq.

As mentioned earlier, one of the greatest challenges in PET quantification is that the quantitative accuracy is impacted by a complex interplay of multiple physical factors, along with the exact implementations of scanner calibrations, data corrections and image reconstruction parameters, many of which are proprietary and specific to the scanner manufacturer. A comprehensive and quantitative study using an independent image reconstruction platform may be beneficial to fully understand the origins of all types of quantitative biases observed, however this is beyond the scope of this study. Two primary types of biases were observed in the study: (1) bias that depends on the amount of radioactivity in the FOV; and (2) bias that depends on the number of total counts in the image. Based on the results, quantification in dynamic imaging studies may be most impacted by the frame length-dependent biases. Clinical and research imaging studies with total-body PET, both higher and lower dose, with static image reconstruction and longer frame durations (i.e. > 30 s) are expected to exhibit quantification biases within $\pm 5\%$.

Conclusion

The quantitative accuracy of the first total-body PET imaging system, the EXPLORER PET/CT scanner, was evaluated using a set of experiments devised to cover the range of activity and count rates representative of both clinical and research total-body imaging applications. Through these evaluations we demonstrated a relative count rate quantification accuracy of $\pm 3 - 4\%$, an axial uniformity spread of $\pm 3\%$ across the central 90% axial FOV of the scanner (175 cm region), and a 3% activity bias from low to high activity (17 – 474 MBq) in a 2 m long uniform cylinder. We also showed a stable ROI quantification of 1% from 22 – 217 MBq with the triple IQ phantoms, and relatively stable VOI quantification across 0.2 – 100% of total counts through re-sampled datasets. In addition, we showed an activity bias spread of -2% to +1% post-bolus injections in human subjects in the 2 – 5 min frames. Larger bias changes during the bolus injection phase in humans indicated the difficulty in providing accurate PET data corrections for complex activity distributions across a very large dynamic range. While there are opportunities to optimize the data corrections and image reconstruction parameters, our results overall indicated that the quantitative performance achieved with the EXPLORER total-body PET/CT scanner is uniform across the axial FOV of the scanner and provides the level of quantitative accuracy required to support a wide range of imaging applications spanning from low-dose studies to dynamic imaging with commonly used frame lengths.

Chapter 3 – Relating ^{18}F -FDG image signal-to-noise ratio to time-of-flight noise-equivalent count rate in total-body PET using the EXPLORER scanner

Introduction

In positron emission tomography (PET), the image signal-to-noise ratio (SNR) is a common metric used to characterize image quality. One way to predict image SNR is by assessing the count rate performance of a PET system using the noise-equivalent count rate (NECR), a surrogate metric adopted into the National Electrical Manufacturers Association (NEMA) NU 2 standard ([NEMA NU 2-2018](#)) that estimates the effective true count rate of a PET system in the presence of scattered and random coincidences. The linear relationship between image SNR^2 and noise-equivalent count (NEC) was first introduced in Brownell 1979 and [Strother 1990](#) for linear reconstruction algorithms, such as filtered back-projection (FBP). It was later shown that the relationship also applied experimentally for non-linear reconstruction methods, such as ordered-subset expectation-maximization (OSEM) algorithms ([Dahlbom 2005](#)). Based on this linear relationship, NECR may be used to optimize injected radiotracer dose, guide imaging protocol design, and can, in appropriate circumstances, directly predict image quality in humans ([Lartzien 2002](#), [Watson 2005](#), [Danna 2006](#), [Chang 2011](#), [Carlier 2014](#)).

With the introduction of long axial field-of-view (FOV) total-body PET systems, such as the 194 cm EXPLORER PET/CT scanner, the entire adult human can be enclosed inside the axial FOV of the PET system for the first time ([Badawi 2019](#), [Spencer 2021](#)). The 15 – 68 fold increase in system sensitivity ([Spencer 2021](#)) across the adult human compared to conventional PET systems with 15 – 30 cm axial FOV broadens the dynamic range of activity levels accessible to PET and enables, for example, delayed time point or imaging with reduced injected activity ([Badawi 2019](#), [Berg 2020](#), [Vera 2020](#), [Liu 2021](#)). The total-body scanner also opens the possibility for new research applications, such as dynamic imaging with short frame lengths ([Zhang 2020a](#)), and kinetic modeling across the entire human subject ([Feng 2020](#), [Wang 2020](#), [Zhang 2020b](#)).

Although the use of NECR as a surrogate metric to predict image quality in conventional PET systems is well studied and is mathematically well modeled in phantoms, the relationship between image SNR and NECR is not well investigated in human subjects when extended to a long axial FOV environment. With the 194 cm length and wide axial acceptance angle (up to 57.0°) of the EXPLORER

scanner ([Spencer 2021](#)), the count rates across the scanner can vary substantially in human subjects, particularly during the early phase of dynamic imaging, which is not well represented by phantom NECR experiments alone. When using conventional PET systems, it was also suggested that the patient-specific NECR can vary widely across different bed positions ([Watson 2005](#)). As a result, the optimal injected dose may vary for different bed positions. With the EXPLORER scanner, a global NECR across the body (i.e. total-body NECR) can be obtained in a single bed position, which may help minimize the complexity when developing imaging protocols and optimal injected doses based on a global metric that is independent of bed position. Another potential benefit when imaging the entire human body at once is that the total activity inside the human subject can be obtained using reconstructed images, regardless of voiding between consecutive scans, which is not possible with conventional PET systems without direct measurements of the excretion. This means that a global NECR curve across the entire human body can be produced using experimental data for the first time.

An important consideration when assessing NECR in total-body PET is that the current NEMA NU 2 NECR protocol ([NEMA NU 2-2018](#)) does not account for count rate performance gains due to time-of-flight (TOF). With the large axial acceptance angles and when combined with an order of magnitude greater volume of scintillator material than conventional scanners ([Jakoby 2011](#), [Spencer 2021](#)), the random coincidence count rate can become significant. As a result, the use of TOF-NECR may be particularly important to accurately assess the count rate performance of total-body PET scanners. Non-TOF NECR only captures the sensitivity of a scanner to coincidence events and not the count rate dependent performance gain due to TOF. It was previously suggested that a TOF-enabled PET system improves image SNR due to the ability to localize the site of annihilation along the line-of-response (LOR) and therefore reduces the variance in the reconstructed images ([Snyder 1981](#), [Budinger 1983](#), [Moses 2003](#)). There should be value in using TOF-NECR rather than non-TOF NECR as a surrogate metric to predict TOF-reconstructed image quality.

Following the count rate performance results measured previously with NEMA NU 2 NECR phantoms in total-body PET ([Spencer 2021](#)), this work assesses the total-body NECR in a long uniform water cylinder and 14 healthy human subjects using the EXPLORER scanner. To do so, the NEMA NU 2-2018 NECR expression as well as the TOF-NECR expression ([Conti 2005](#)) were modified to enable the

processing of list-mode coincidence data. Then, the image SNR², non-TOF NECR and TOF-NECR of the long uniform water cylinder and human subjects were assessed. The subjects were grouped according to their body mass index (BMI) to assess the effects of body size on the relationships between NECR and SNR.

Methods

Derivation of NEC expressions for list-mode coincidence data

The SNR² expressions for both non-TOF and TOF ([Conti 2005](#)) can be rewritten into the following

non-TOF and TOF forms for NEC, as shown in $NEC_{non-TOF} = \frac{T^2}{\left(T+S+\frac{D}{D_{FOV}}R\right)}$

$$\text{(Equation 3-1 and } NEC_{TOF} = \frac{D}{\Delta x} \cdot \frac{T^2}{\left(T+S+\left(\frac{D}{D_{FOV}}\right)^2 R\right)} \quad \text{(Equation 3-2:}$$

$$NEC_{non-TOF} = \frac{T^2}{\left(T+S+\frac{D}{D_{FOV}}R\right)} \quad \text{(Equation 3-1)}$$

$$NEC_{TOF} = \frac{D}{\Delta x} \cdot \frac{T^2}{\left(T+S+\left(\frac{D}{D_{FOV}}\right)^2 R\right)} \quad \text{(Equation 3-2)}$$

where T , S , and R are the true, scattered, and random coincidence counts; D is the object diameter; $D_{FOV} = ct_w/2$ is the diameter of the FOV, which depends on the speed of light c and the coincidence time window t_w ; and $\Delta x = c\Delta t/2$ is the TOF localization uncertainty, which depends on the timing resolution of the PET system (Δt).

$$\text{Then, } NEC_{non-TOF} = \frac{T^2}{\left(T+S+\frac{D}{D_{FOV}}R\right)} \quad \text{(Equation 3-1 and } NEC_{TOF} = \frac{D}{\Delta x} \cdot$$

$$\frac{T^2}{\left(T+S+\left(\frac{D}{D_{FOV}}\right)^2 R\right)} \quad \text{(Equation 3-2 can be rewritten into } NEC_{non-TOF} =$$

$$\frac{(\sum_i T_i)^2}{\sum_i T_i + \sum_i S_i + \sum_i \left(\frac{D_i}{D_{FOV,i}} R_i\right)} \quad \text{(Equation 3-3 and } NEC_{TOF} = \frac{1}{\Delta x} \cdot \frac{(\sum_i D_i T_i)^2}{\sum_i D_i T_i + \sum_i D_i S_i + \sum_i \left(\frac{D_i^3}{D_{FOV,i}^2}\right) R_i}$$

(Equation 3-4 for list-mode coincidence data over all LORs ([Poon 2013](#)):

$$NEC_{non-TOF} = \frac{(\sum_i T_i)^2}{\sum_i T_i + \sum_i S_i + \sum_i \left(\frac{D_i}{D_{FOV,i}} R_i\right)} \quad \text{(Equation 3-3)}$$

$$NEC_{TOF} = \frac{1}{\Delta x} \cdot \frac{(\sum_i D_i T_i)^2}{\sum_i D_i T_i + \sum_i D_i S_i + \sum_i \left(\frac{D_i^3}{D_{FOV,i}^2}\right) R_i} \quad (\text{Equation 3-4})$$

where i is the i^{th} LOR, $D_i = \max(D_i, \Delta x)$ is the intersection distance between the i^{th} LOR and the object; T_i , S_i , and R_i are the true, scattered and random coincidence counts in the i^{th} LOR, and $D_{FOV,i}$ is the diameter of the FOV for the i^{th} LOR.

$$\text{The randoms component in } NEC_{non-TOF} = \frac{T^2}{\left(T+S+\frac{D}{D_{FOV}}R\right)} \quad (\text{Equation 3-1})$$

$$\text{and } NEC_{non-TOF} = \frac{(\sum_i T_i)^2}{\sum_i T_i + \sum_i S_i + \sum_i \left(\frac{D_i}{D_{FOV,i}}\right) R_i} \quad (\text{Equation 3-3 differs from the NECR})$$

expression described in the NEMA NU 2-2018 NECR protocol by a factor of D/D_{FOV} . This is because in the NU 2 NECR protocol, the LORs that do not intersect the phantom are discarded. For consistency with the NU 2 NECR expression, Equations 3 and 4 are modified to reduce the randoms component by a

$$\text{factor of } D/D_{FOV}, \text{ ultimately leading to } NEC_{non-TOF} = \frac{(\sum_i T_i)^2}{\sum_i T_i + \sum_i S_i + \sum_i R_i}$$

$$(\text{Equation 3-5 (Poorn 2013)}) \text{ and } NEC_{TOF} = \frac{1}{\Delta x} \cdot \frac{(\sum_i D_i T_i)^2}{\sum_i D_i T_i + \sum_i D_i S_i + \sum_i \left(\frac{D_i^2}{D_{FOV,i}}\right) R_i}$$

(Equation 3-6:

$$NEC_{non-TOF} = \frac{(\sum_i T_i)^2}{\sum_i T_i + \sum_i S_i + \sum_i R_i} \quad (\text{Equation 3-5})$$

$$NEC_{TOF} = \frac{1}{\Delta x} \cdot \frac{(\sum_i D_i T_i)^2}{\sum_i D_i T_i + \sum_i D_i S_i + \sum_i \left(\frac{D_i^2}{D_{FOV,i}}\right) R_i} \quad (\text{Equation 3-6})$$

To maintain similarity with the numerator of the non-TOF NEC expression shown in

$$NEC_{non-TOF} = \frac{(\sum_i T_i)^2}{\sum_i T_i + \sum_i S_i + \sum_i R_i} \quad (\text{Equation 3-5, the TOF NEC expression in})$$

$$NEC_{TOF} = \frac{1}{\Delta x} \cdot \frac{(\sum_i D_i T_i)^2}{\sum_i D_i T_i + \sum_i D_i S_i + \sum_i \left(\frac{D_i^2}{D_{FOV,i}}\right) R_i} \quad (\text{Equation 3-6 was divided by } D^2 \text{ in both the})$$

$$\text{numerator and denominator and rewritten into } NEC_{TOF} = \frac{(\sum_i T_i)^2}{\sum_i \frac{\Delta x}{D_i} [T_i + S_i + \left(\frac{D_i}{D_{FOV,i}}\right) R_i]}$$

(Equation 3-7:

$$NEC_{TOF} = \frac{(\sum_i T_i)^2}{\sum_i \frac{\Delta x}{D_i} [T_i + S_i + \left(\frac{D_i}{D_{FOV,i}}\right) R_i]} \quad (\text{Equation 3-7})$$

where $\frac{\Delta x}{D_i} T_i$, $\frac{\Delta x}{D_i} S_i$, and $\frac{\Delta x}{D_{FOV,i}} R_i$ are the reduced variance of true, scattered, and random coincidence counts in the i^{th} LOR. The expression in Equation 6b shows that the reduced variance of the i^{th} LOR is dependent of the timing resolution of the PET system (which is related to Δx), the object size (D_i), and the coincidence time window (which is related to $D_{FOV,i}$).

System parameters

The 194 cm long EXPLORER scanner consists of 8 PET scanner units, with a 786 mm ring diameter. Each unit contains 24 detector modules, with each module containing 5 x 14 (transaxial x axial) detector blocks, where each block contains 7 x 6 (transaxial x axial) scintillator crystals (each 2.76 x 2.76 x 18.1 mm³). The time-of-flight (TOF) resolution of the system is 505 ps, and the spatial resolution of the system is ≤ 3.0 mm full width at half maximum (FWHM) near the center of the scanner. The system utilizes a scanner unit-based variable time window (4.5 – 6.9 ns) and allows each unit to form coincidence events with up to a maximum unit difference of 4, corresponding to a maximum axial acceptance angle of 57.0°. The energy window of the system is 430 – 645 keV. Detailed information regarding the scanner is shown in [Spencer 2021](#).

Uniform phantom

An acrylic uniform water cylinder (16.5 cm outer diameter, 15 cm inner diameter, 210 cm long) filled with ¹⁸F-FDG and covering the entire axial FOV was positioned at the center of the scanner. List-mode data were acquired at five time points over 10 h, from 474 MBq to 17 MBq in the FOV of the scanner. The duration for each scan was 60 min, and twelve 5-min dynamic PET images were reconstructed. To assess the SNR of the images, 50 mm spherical volumes of interest (VOIs) were drawn at the center of the FOV of the scanner and analyzed using $SNR = \frac{\mu}{\sigma}$

(Equation 3-8:

$$SNR = \frac{\mu}{\sigma} \quad \text{(Equation 3-8)}$$

where μ and σ are the mean and standard deviation of the VOI, respectively.

Human subjects

Data from 14 healthy human subjects injected with ^{18}F -FDG were selected for this work (IRB #1341792). Details of the subjects are shown in Table 3-1. The human subjects were positioned at the center of the scanner in a supine position with hands placed above the head at 90 min, 3 h, 6 h, 9 h, and 12 h after radiotracer injection and were scanned for 20 min at each time point. A low-dose CT scan was performed at the 90-min time point (140 kVp, 50 mAs), while ultralow-dose CT scans were performed at the later time points (140 kVp, 5 – 20 mAs depending on the size of the human subject).

The image SNR analysis was based on a 50 mm diameter spherical VOI positioned in a uniform region of the liver. For human subjects with significant motion in the liver, elongated cylindrical VOIs with similar number of voxels as the spherical VOI were drawn instead. To account for activity redistribution in the liver as well as the variations in liver uptake across human subjects, the SNR^2 of the liver for time point t (SNR_t^2) was adjusted and normalized to the study population ($\text{SNR}_{adjusted,t}^2$) using $\text{SNR}_{adjusted,t}^2 =$

$$\text{SNR}_t^2 \times \frac{\text{SUV}_0}{\frac{\text{TIDA}_0 \times 0.5^{t/T_{1/2}}}{\text{TIDA}_t} \times \text{SUV}_t} \times \frac{\text{SUV}_0}{\overline{\text{SUV}_0}} \quad (\text{Equation 3-9, assuming the SNR can be scaled}$$

in a Poisson-like manner with activity concentration:

$$\text{SNR}_{adjusted,t}^2 = \text{SNR}_t^2 \times \frac{\text{SUV}_0}{\frac{\text{TIDA}_0 \times 0.5^{t/T_{1/2}}}{\text{TIDA}_t} \times \text{SUV}_t} \times \frac{\text{SUV}_0}{\overline{\text{SUV}_0}} \quad (\text{Equation 3-9})$$

where SUV_0 is the standardized uptake value (SUV) of the liver from the 90-min scan; $\text{TIDA}_0 \times 0.5^{t/T_{1/2}}$ is the expected total image-derived activity (TIDA) at time t after the 90-min scan, based on the TIDA from the 90-min scan (TIDA_0) and the half-life of ^{18}F ($T_{1/2} = 109.771$ min); TIDA_t is the TIDA at time t ; SUV_t is the SUV of the liver at time t ; and $\overline{\text{SUV}_0}$ is the average liver SUV of the liver from the 90-min scan across all human subjects.

Table 3-1. Details of the healthy human subjects (n=14).

Parameter	Value
Age (years)	29 – 78 (mean: 50.6)
BMI (kg/m ²)	19.4 – 37.0 (mean: 28.8)
Weight (kg)	53.0 – 109 (mean: 80.0)
Height (m)	1.57 – 1.80 (mean: 1.67)
Injected ^{18}F -FDG dose (MBq)	337 – 394 (mean: 371)

Data processing

The non-TOF NECR and TOF-NECR were calculated using Equations 5 and 6 and divided by the acquisition time. Due to the large number (9.2×10^{10}) of LORs of the EXPLORER scanner ([Spencer 2021](#)), the list-mode data was re-binned into detector block-pair sinograms to maximize computational efficiency. True coincidences were estimated based on the direct subtraction of scattered and random coincidences from the prompt coincidence data. To further streamline data processing, scatter estimation was based on a customized version of the SimSET Monte Carlo simulation package (v2.9.2) that incorporates variable attenuation coefficients ([Leung 2021a](#)). Each detector block-pair trues plus scatters sinogram from the simulation was scaled to match the experimental prompt minus delay detector block-pair sinogram using least squares fitting. Information regarding the variable attenuation coefficients method for scatter estimation is described in the appendix. Finally, random coincidences were based on the data from the delayed coincidence channel.

For consistency with the NEMA NU 2-2018 NECR protocol, coincidence events outside the scan object were excluded. To do so, the bed in the CT image volume was first removed using an automated segmentation method based on an ROI of the bed. Then, a binary mask based on the thresholded forward projection of the CT image volume (to exclude air) was applied to the detector block-pair sinograms.

Image reconstruction

The PET images were reconstructed using a vendor-provided, research-only list-mode TOF-OSEM reconstruction platform installed on in-house computational hardware. To ensure consistency with our previous work on assessing the quantification accuracy of the EXPLORER scanner ([Leung 2021b](#)), all images were reconstructed with 4 iterations, 20 subsets, and with 4 mm isotropic voxels in a 150 x 150 x 486 image matrix. Resolution modeling (i.e. point spread function (PSF)) was not included, and no post-reconstruction smoothing was applied to the reconstructed images. All other PET data corrections were applied, including corrections for scatter and random coincidences, attenuation, dead-time, normalization, and radioactive decay.

Results

Uniform phantom

The non-TOF NECR and TOF-NECR of the uniform phantom are shown in Figure 3-1. At an activity concentration of 13.8 kBq/mL, the TOF-NECR was 3.1-fold higher than non-TOF NECR. Also, while the non-TOF NECR curve began to plateau as the activity concentration approached 15 kBq/mL, the TOF-NECR curve continued to increase at a greater rate. Figure 3-2 shows the relationship between SNR^2 and non-TOF NECR, as well as TOF-NECR, respectively. The SNR^2 increased more rapidly than non-TOF NECR at higher count rates, while the relationship between SNR^2 and TOF-NECR was more linear over the range of values studied. The linear fit R^2 values for SNR^2 vs. non-TOF NECR and TOF-NECR were 0.94 and 0.98, respectively.

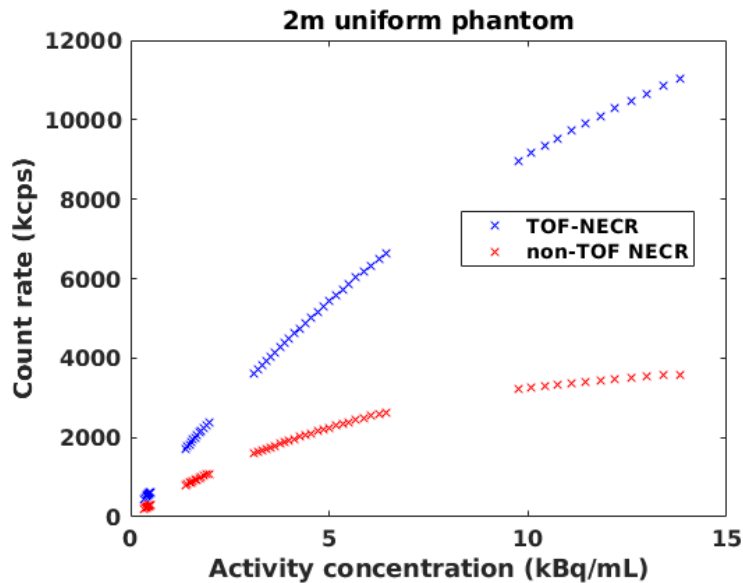


Figure 3-1. The non-TOF NECR and TOF-NECR of the uniform phantom.

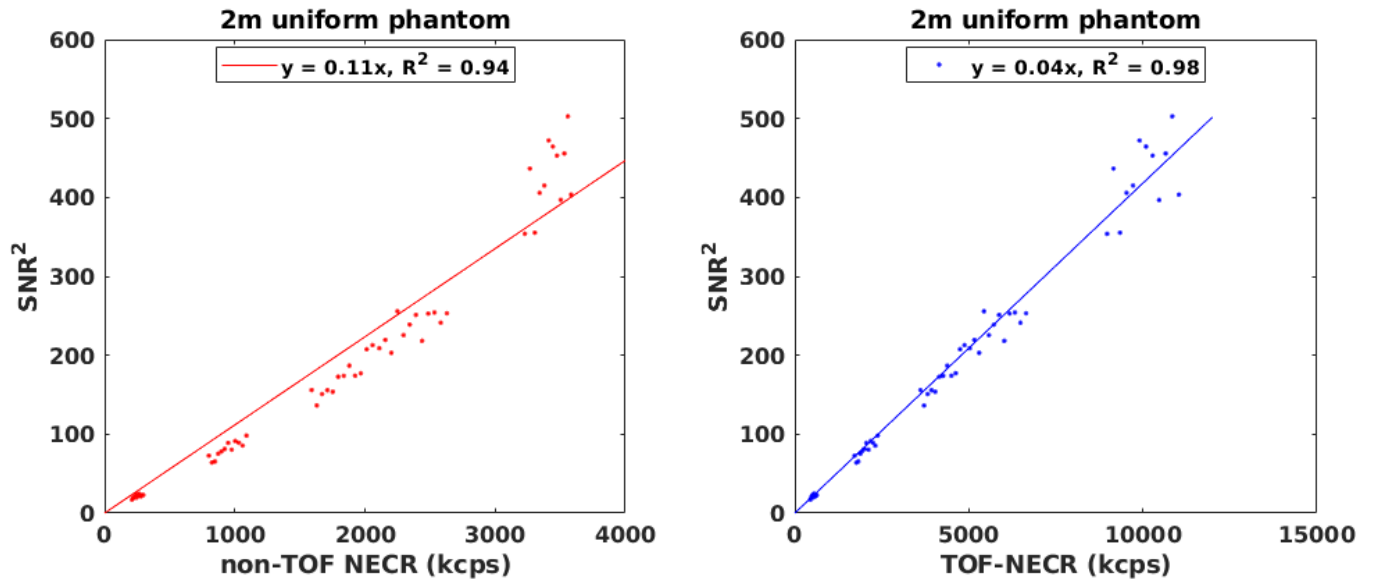


Figure 3-2. The image SNR^2 of the uniform phantom, plotted against (left) non-TOF NECR, and (right) TOF-NECR.

Human subjects

Figure 3-3 shows the non-TOF NECR and TOF-NECR of the human subjects, plotted against the activity concentration as well as the activity. Figure 3-4 shows the relationship between the adjusted SNR^2 and non-TOF NECR, as well as TOF-NECR, respectively. Since the slope of the SNR^2 vs. non-TOF NECR and TOF-NECR depends on the geometry as well as the activity distribution of the scan object, a linear fit was performed individually on each human subject. The mean R^2 values for the adjusted SNR^2 vs. non-TOF NECR and TOF-NECR of all 14 human subjects were 0.98 (min: 0.91) and 0.98 (min: 0.94), respectively. For reference, Figure 3-5 shows the relationship between the unadjusted SNR^2 and non-TOF NECR, as well as TOF-NECR, respectively. The mean R^2 values for the unadjusted SNR^2 vs. non-TOF NECR and TOF-NECR of all 14 human subjects were 0.97 (min: 0.90) and 0.98 (min: 0.94), respectively.

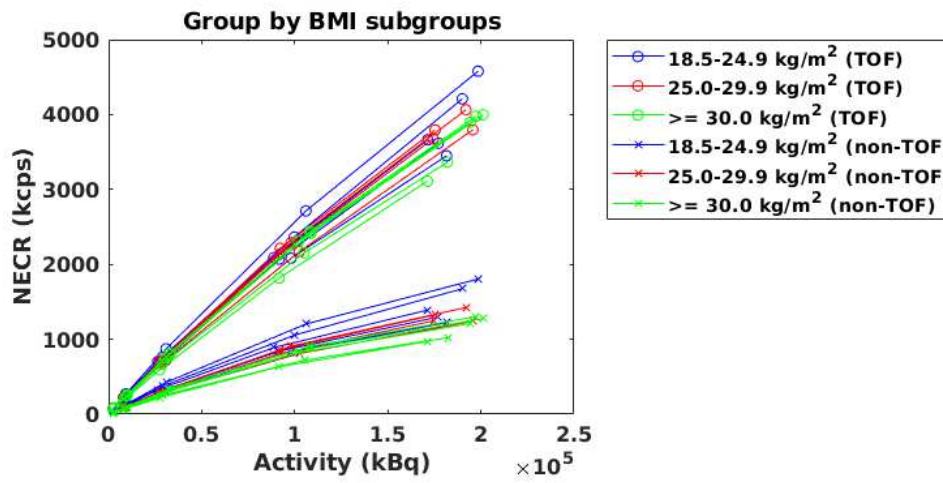
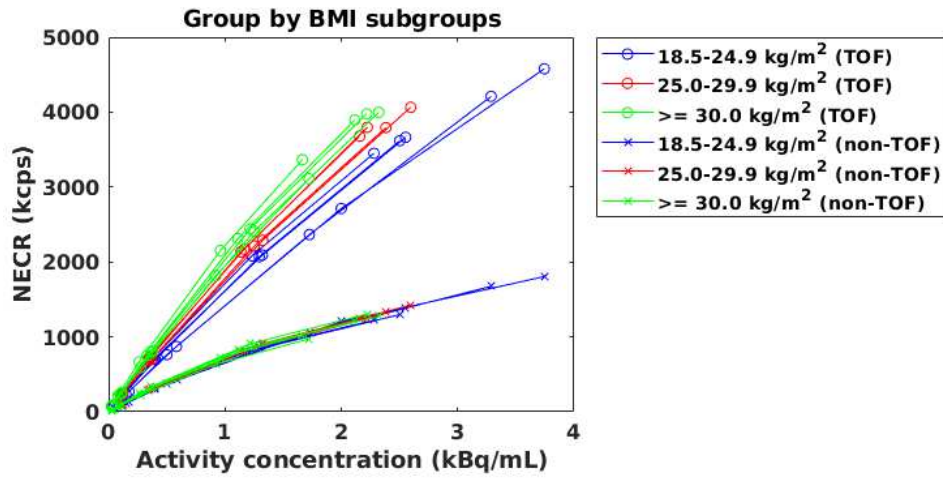


Figure 3-3. The non-TOF NECR and TOF-NECR of human subjects, plotted against (top) activity concentration, and (bottom) activity.

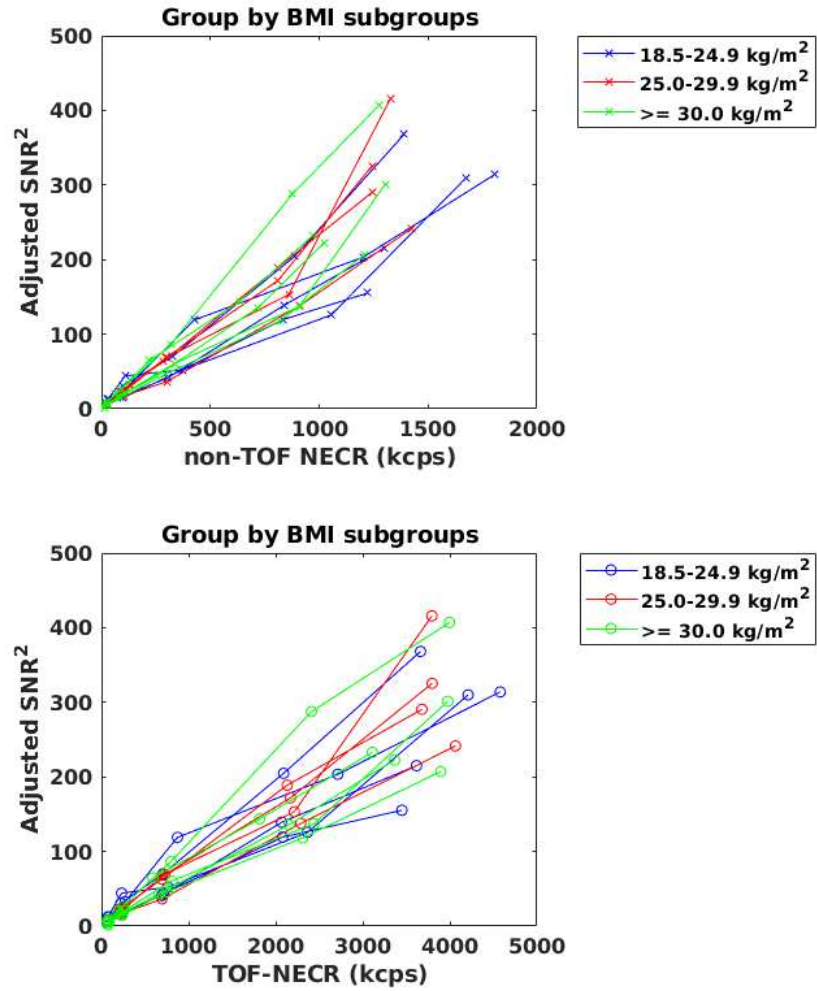


Figure 3-4. The adjusted SNR² of the human subjects, plotted against (top) non-TOF NECR, and (bottom) TOF-NECR. A linear fit was performed on each human subject, and the mean R² values for SNR² vs. non-TOF NECR and TOF-NECR of all 14 human subjects were 0.98 (min: 0.91) and 0.98 (min: 0.94), respectively.

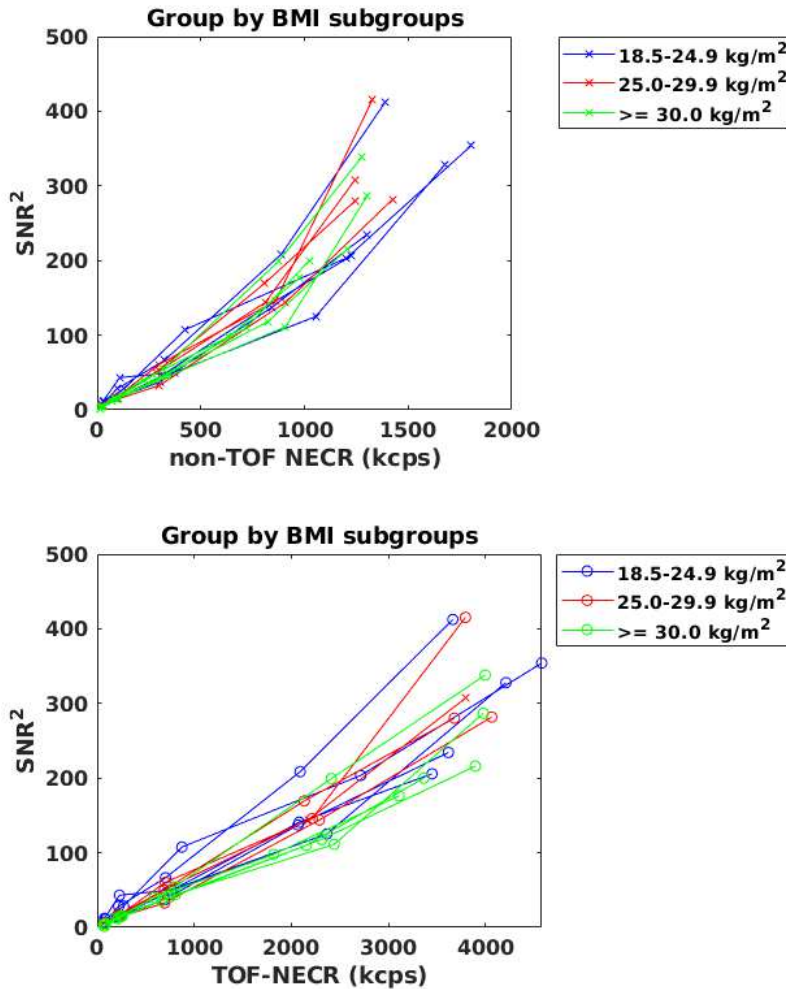


Figure 3-5. The SNR² of the human subjects, plotted against (top) non-TOF NECR, and (bottom) TOF-NECR. A linear fit was performed on each human subject, and the mean R² values for SNR² vs. non-TOF NECR and TOF-NECR of all 14 human subjects were 0.97 (min: 0.90) and 0.98 (min: 0.94), respectively.

Discussion

The NECR results shown in Figure 3-1 covers the activity concentration range for typical EXPLORER ¹⁸F-FDG PET scans (~300 MBq injected; scan begins at 120 min after radiotracer injection) which may suggest that the injected activity in human subjects may be increased beyond the activity concentration at peak non-TOF NECR (if permitted) to improve TOF-reconstructed image SNR when using the EXPLORER total-body scanner. The non-TOF NECR results suggest an activity concentration

of approximately 15 kBq/mL at peak non-TOF NECR, with diminishing gains starting at approximately 10 kBq/mL. The TOF-NECR results, on the other hand, continued to increase at a greater rate, suggesting that the activity concentration at peak TOF-NECR may be substantially higher than that at peak non-TOF NECR. Furthermore, the TOF-NECR results in Figure 3-2 were linearly correlated with image SNR², while the image SNR² increased more rapidly than the linear fit at higher non-TOF NECR, suggesting that the TOF-NECR metric may be more suitable for directly predicting the image quality of the EXPLORER scanner. Given that TOF-enabled PET systems are expected to improve image SNR ([Snyder 1981](#), [Budinger 1983](#), [Moses 2003](#)), the results may also suggest the activity concentration limits expected from the standard non-TOF NECR measurements may be less appropriate for estimating the count rate performance of the TOF-enabled EXPLORER total-body scanner. This may especially be an important consideration when imaging radiotracers with shorter half-lives, such as in ⁸²Rb cardiac imaging or ¹⁵O studies, though further investigation by assessing image SNR for these imaging scenarios is needed. Overall, it was found that the relationship between image SNR² and non-TOF NECR may not be entirely linear for images reconstructed with the TOF-OSEM algorithm, which may suggest that the use of TOF-NECR may be more appropriate for assessing the count rate performance of PET systems with TOF capability, as demonstrated in Figure 3-2 and Figure 3-4.

In Figure 3-3 (top), the non-TOF NECR curves for all 14 human subjects overlapped with each other when plotted against activity concentration, but not for TOF-NECR. In addition, the TOF-NECR curves appeared to increase with higher BMIs. We suggest that this may be related to the combination of higher total activity in the higher BMI subjects during the scan as well as the greater count rate performance gains due to TOF for larger subjects. The overlaps between human subjects across BMIs with non-TOF NECR is peculiar and suggests that a weight-based dosing scheme may potentially be appropriate for adult humans when assessing non-TOF reconstructed images from the EXPLORER scanner, although further investigation is needed. In Figure 3-3 (bottom), the count rate performance gain due to TOF was generally higher with increasing BMIs for each human subject, which is consistent with

the TOF-NEC expression shown in $NEC_{TOF} = \frac{(\sum_i T_i)^2}{\sum_i \frac{\Delta x_i}{D_i} [T_i + S_i + (\frac{D_i}{D_{FOV,i}}) R_i]}$ (Equation 3-7)

where the count rate performance is expected to increase with larger objects.

In Figure 3-4, the image SNR² vs. both non-TOF NECR and TOF-NECR overlapped between subjects across a wide range of BMIs. Although this may be unexpected at first glance, variations in activity distribution between different subjects can affect the NECR curves and subsequently the slope of the SNR² vs. NECR plots. Also, the activity range assessed in the human subjects did not approach peak non-TOF NECR and may explain the similar R² values observed for image SNR² vs. non-TOF NECR and TOF-NECR. Future studies that utilize phantoms with varying diameters and lengths, as well as increasing the activity level in humans (if permitted), may provide more insight on this.

As shown in both Figure 3-4 and Figure 3-5, the use of adjusted SNR² over unadjusted SNR² led to a small increase (0.01) in mean R² value for the non-TOF NECR case, but not for the TOF-NECR case. At the same time, the mean R² values for all cases were 0.90 or higher. Future studies involving finer time sampling and a higher injected activity may help discern the effects when accounting for activity redistribution in the liver using adjusted SNR² vs. unadjusted SNR². Additionally, simulations of human subjects with activity redistribution in the liver may also help assess the effectiveness of the adjusted SNR² metric by further removing potential variability attributed to VOI positioning due to multiple PET acquisitions at different time points.

Based on the results, we attempted to determine if an optimal injected activity level can be found for a given TOF-NECR with respect to BMI, Figure 3-6. The optimal (left) activity concentration, and (right) activity vs. BMI when TOF-NECR = 3000 kcps for the 14 human subjects. shows the optimal activity concentration and activity vs. BMI when a target TOF-NECR of 3000 kcps is specified. The R² values for both plots were 0.87 and 0.34, respectively.

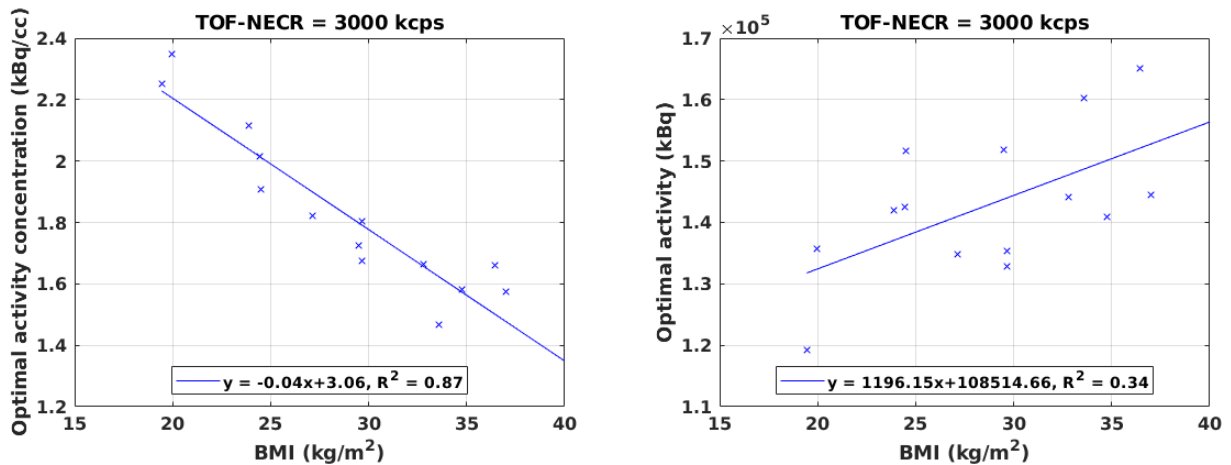


Figure 3-6. The optimal (left) activity concentration, and (right) activity vs. BMI when TOF-NECR = 3000 kcps for the 14 human subjects.

Overall, although a linear relationship was found between SNR^2 of OSEM-reconstructed images and TOF-NECR for both the uniform water phantom and human subjects, caution should be exercised to not overinterpret the data for several reasons. First, while it was previously reported ([Dahlbom 2005](#)) that the non-TOF reconstructed image SNR^2 and non-TOF NECR were linearly proportional to each other using OSEM reconstructions (up to 120 kcps) and that similar trends were found in this work, the OSEM algorithm itself is not a linear reconstruction algorithm and therefore the results may vary significantly depending on reconstruction parameters. In addition, at low count conditions some of the additional non-linear behavior between image SNR^2 and TOF-NECR may be related to the non-negativity constraints imposed by Poisson distribution. Additional work using a variety of reconstruction parameters, such as using different reconstruction voxel sizes and varying number of subsets and iterations to ensure convergence, is needed to ensure the linear relationship applies for a wide variety of imaging conditions. In addition, despite the ability to derive the total activity in the human subjects based on reconstructed images, a ground truth cannot be directly determined since the subjects voided between consecutive scans. It may be beneficial to collect and measure the activity in the excretion between scans to ensure all activities are directly measured and accounted for. Finally, both the image SNR in the liver and the NECR can vary since ^{18}F -FDG redistributes in the body over time. Additional work using other tracers that are more stable in the liver and/or other organs over longer durations, such as ^{68}Ga -NEB which binds to serum albumin ([Niu 2014](#), [Zhang 2015](#)), may further strengthen the robustness of the total-body TOF-NECR estimations in humans.

Conclusion

The relationship between image SNR and total-body NECR in long axial FOV PET was assessed for the first time using the EXPLORER total-body PET/CT scanner. The TOF-NEC expression ([Conti 2005](#)) was rewritten for list-mode PET data, and both the non-TOF NECR and TOF-NECR were compared using datasets from a long uniform water cylinder and 14 human subjects scanned up to 12

hours after radiotracer injection. The TOF-NECR for both the uniform water cylinder and the human subjects were found to be linearly proportional to the TOF-reconstructed image SNR², but less so for non-TOF NECR. The use of TOF-NECR to estimate the count rate performance of TOF-enabled PET systems may potentially be more appropriate for predicting the SNR of TOF-reconstructed images. Additional phantom and human studies are needed to further assess the applicability of TOF-NECR in PET systems with TOF capabilities.

Acknowledgement

We thank Dr. Robert L. Harrison for his help in modifying the SimSET source code to accept additional material definitions, and we thank Dr. Zhaoheng Xie and Dr. Xuezhu Zhang for their help in validating the scatter estimation method using continuous water density materials and the default SimSET materials with the XCAT phantom. We also thank Dr. Jonathan K. Poon for his initial work on deriving the non-TOF NECR and TOF-NECR expressions for list-mode data. In addition, we thank Dr. Jinyi Qi for his help in deriving the final NECR expressions for list-mode data. Finally, we thank Dr. Yasser Abdelhafez for his help for drawing the VOIs in the liver.

Appendix

To perform Monte Carlo scatter estimation, the required components are: 1) an attenuation map, in the form of a material map; 2) an activity map; 3) a model of the scanner and its electronics; and 4) a Monte Carlo physics engine. With experimental data as simulation input, the material map is typically generated via a threshold-based segmentation of the CT image volume. Due to the limited number of materials available in common Monte Carlo simulation software (such as GATE and SimSET), the attenuation map is typically segmented into only a few materials ([Levin 1995](#), [Moliner 2019](#)). As shown in Figure 3-7, the Hounsfield Unit (HU) distribution in a healthy adult human is continuous and is therefore unlikely to be well represented by only a very small number of materials. When the granularity of the material map is limited, the accuracy of scatter estimation may be affected, particularly in regions where the attenuation and scattering properties vary widely, such as in the chest region which is surrounded by the lung, heart, and bone tissues.

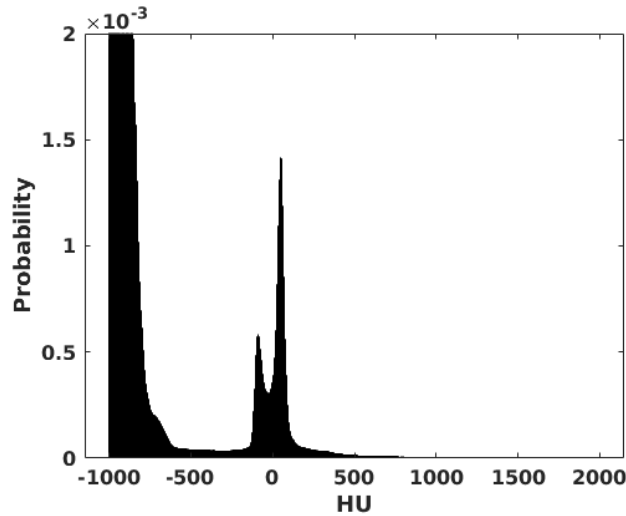


Figure 3-7. HU probability distribution in the CT image volume of a healthy adult human subject.

To preserve the granularity of the attenuation map (converted from the CT image volume) used in the Monte Carlo simulation, a method that generates a continuous water density map from the CT image volume was developed, which serves as a surrogate to the material map required for the simulations. The method was first validated against default SimSET materials using both count statistics and reconstructed images from an XCAT phantom, and then evaluated in the projection space to eliminate influences due to image reconstruction, using a phantom constructed from a 3 x 3 grid of square tubing. The SimSET source code was modified to increase the maximum number of materials from 100 (29 standard materials + 71 placeholder materials) to 22100 materials (100 default SimSET materials + 22000 water density materials). The water density materials corresponded to water densities ranging from 0.001 g/cm³ to 2.2 g/cm³ (in 0.001 g/cm³ increments) and were generated using the SimSET material generator. The water density range covers a wide range of Hounsfield Units (HUs) expected in the CT image volume of a healthy adult human subject, as shown in Figure 3-7.

The material index map for SimSET is generated using a 3-part process as shown in Figure 3-8. The DICOM CT image volume is read, then rescaled with the associated rescale slope and intercept. The CT images are then interpolated and resized as needed to match the dimensions of the activity map. The voxel values in the CT images are limited to between -1000 HU and 2000 HU to remove outlier values introduced by potential image artifacts, as well as to reduce the number of materials required to

encompass the specified HU range, which minimizes the initialization time required for the simulation (it takes approximately an hour to load 20000+ material definitions into SimSET). As shown earlier in Figure 3-7, the CT HU distribution of human subjects scanned using the EXPLORER scanner demonstrated that a 2000 HU upper limit is sufficient to cover the entire range of HU units in healthy humans, though the lower and upper limits can be tailored for each human subject (e.g. to account for metal implants) if needed. Next, the 511-keV attenuation map is generated using bilinear fitting, as shown in Below break

point: $\mu = 9.6 \times 10^{-5} \cdot (HU + 1000) \text{ cm}^{-1}$ (Equation 3-10 and Above break point: $\mu = a \cdot$

$(HU + 1000) + b \text{ cm}^{-1}$ (Equation 3-11 ([Carney 2006](#)):

Below break point: $\mu = 9.6 \times 10^{-5} \cdot (HU + 1000) \text{ cm}^{-1}$ (Equation 3-10)

Above break point: $\mu = a \cdot (HU + 1000) + b \text{ cm}^{-1}$ (Equation 3-11)

where μ is the 511-keV linear attenuation coefficient (in cm^{-1}), and HU , a , and b are the X-ray tube kVp-dependent values (shown in Table 3-2).

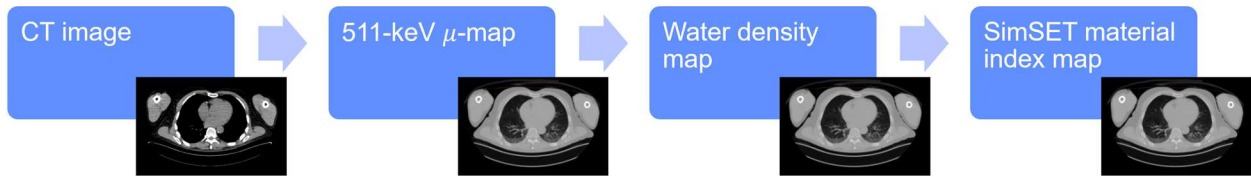


Figure 3-8. A general overview of converting a CT image into a SimSET material index map.

Table 3-2. X-ray tube kVp-dependent values used for generating the 511-keV attenuation map ([Carney 2006](#)).

kVp	$a(\times 10^{-5}) \text{ cm}^{-1}$	$b(\times 10^{-2}) \text{ cm}^{-1}$	Break point (HU)
80	3.64	6.26	50
100	4.43	5.44	52
110	4.92	4.88	43
120	5.10	4.71	47
130	5.51	4.24	37
140	5.64	4.08	30

Once the 511-keV attenuation map is generated, each voxel value in the attenuation map is fitted to an associated water density (0.0001 g/cm^3 increments) that has the closest corresponding 511-keV attenuation coefficient. Preliminary analysis suggests that an appropriate water density material may be

used as a surrogate to replace the default SimSET materials used for the XCAT phantom. Figure 3-9 shows excellent agreement (substantially less than 1% difference) between the linear attenuation coefficient vs. photon energy plots of the brain, bone, and respective fitted water density materials between 430 keV (the LLD of the EXPLORER scanner) and 511 keV. For the default SimSET bone material, the difference at 200 keV was 2.5%. Finally, the water density map is converted into the SimSET material index map for the simulation, and an index translator is used to convert the material index map into materials defined in the customized SimSET software.

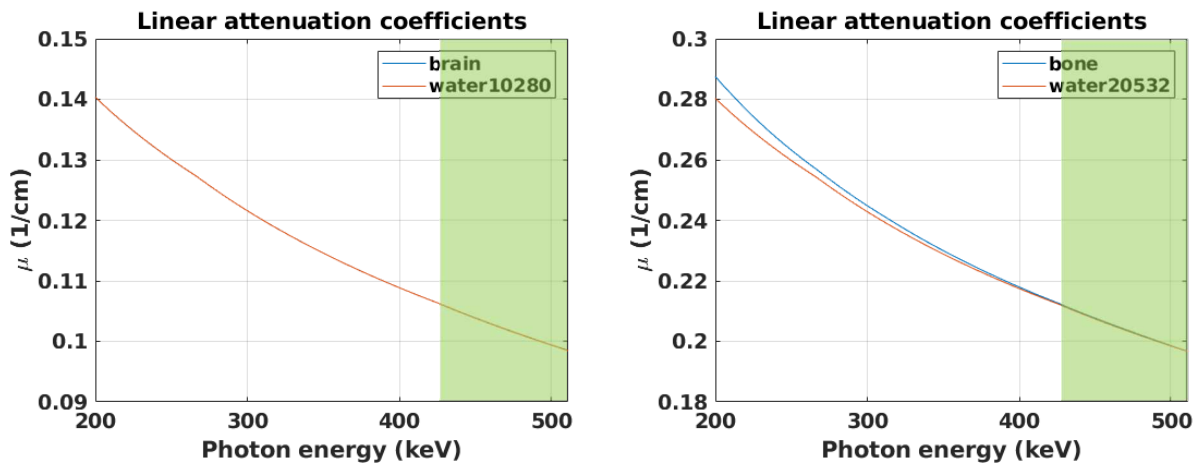


Figure 3-9. The linear attenuation coefficient vs. photon energy plots for the (Left) SimSET brain material, and (Right) SimSET bone material, with respective fitted water density materials. The region highlighted in green shows the energy range between the LLD of the EXPLORER scanner (430 keV) and 511 keV.

To assess the feasibility of using water density materials as a surrogate to the default SimSET materials for biological tissues, an XCAT phantom was simulated using both types of materials with the same random seed. The simulation parameters are shown in Table 3-3. The activity in each organ was simulated separately to extract the respective number of counts and scatter fractions. Since random coincidences were not produced in the simulation, the outputs from all organs were added together prior to image reconstruction for ROI analysis in the brain and the liver. The reconstruction parameters are shown in Table 3-4.

Table 3-3. SimSET simulation parameters for the XCAT phantom.

Crystal material	LYSO
Crystal size	2.76 x 2.76 x 18.1 mm ³
Crystal pitch	2.85 mm transaxial x 2.85 mm axial
# crystals per block	7 transaxial x 6 axial
# block detectors	120-block ring x 112 rings
LLD	435 keV
Energy resolution	11.7% @ 511 keV
Phantom image matrix size	239 x 239 x 679
Phantom image voxel size	2.85 x 2.85 x 2.85 mm ³
Simulation time	30 s

Table 3-4. Reconstruction parameters for the XCAT phantom.

Algorithm	List-mode TOF-OSEM
Image matrix size	239 x 239 x 679
Image voxel size	2.85 x 2.85 x 2.85 mm ³
# iterations and subsets	3 iterations, 10 subsets
Correction(s) applied	Attenuation correction and normalization only
Post-reconstruction smoothing	No

While traditional ROI analysis is commonly used to evaluate the quantitative accuracy in PET, the results can be influenced by the reconstruction parameters as well as the accuracy of various PET data correction implementations, including scatter correction. Therefore, we also evaluated the accuracy of the scatter estimation implementation in projection space, independent of image reconstruction. To do so, a custom 3 x 3 grid phantom made of acrylic square tubing and filled with ¹⁸F-FDG was designed and fabricated, as shown in Figure 3-10. Furthermore, we surrounded the phantom with wax blocks to mimic the scatter fraction that a large human torso may produce, as shown in Figure 3-11. The specification of the phantom is described in Table 3-5.



Figure 3-10. (Left) A 3-D rendering of the 3 x 3 grid phantom. (Right) The 3 x 3 grid phantom.

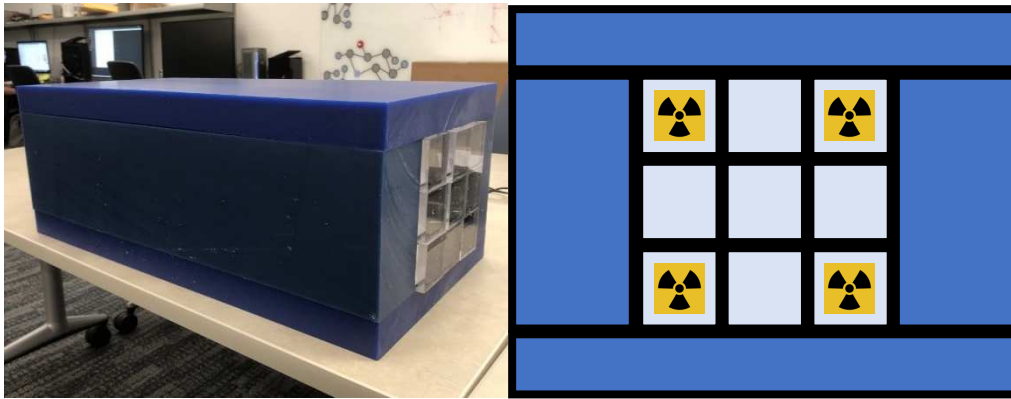


Figure 3-11. (Left) The 3 x 3 grid phantom, surrounded by wax blocks. (Right) A schematic representation of the 3 x 3 grid phantom, where only the corners of the grid are filled with ¹⁸F-FDG.

Table 3-5. Specifications of the 3 x 3 grid phantom

Square tubing exterior dimensions	50.8 x 50.8 x 609.6 mm ³ (2 x 2 x 24 cu. in.)
Wall thickness	3.175 mm (0.125 in.)
Tubing configuration	3 x 3
Phantom exterior dimensions (w/o wax blocks)	152.4 x 152.4 x 609.6 mm ³ (6 x 6 x 24 cu. in.)
Phantom exterior dimensions (w/ wax blocks)	304.8 x 228.6 x 609.6 mm ³ (12 x 9 x 24 cu. in.)

In the 3 x 3 grid phantom, only the 4 corners (as shown in Figure 3-11 and Figure 3-12) of the 3 x 3 grid phantom are filled with ¹⁸F-FDG, and the rest with water. To evaluate the accuracy of the scatter estimation, the projection profile (in both the detector block level and the detector crystal level) that delineates the hot and cold regions were evaluated, as demonstrated in Figure 3-12. Both detector levels were evaluated to assess the effects of data compression on the scattered sinograms. Then, a modified smooth step function ($\bar{C}_{hot,\phi,j} * St(x)$) was fitted to each hot/cold transitions to obtain a sharpness metric, c , to quantify the accuracy of the scatter estimation. A small c value indicates a sharp transition between the hot and cold regions of the projection profile. The modified smooth step function is shown in $\bar{C}_{hot,\phi,j} *$

$$St(x) = \frac{\bar{C}_{hot,\phi,j}}{2} [1 + \tanh(\frac{x-x_0}{c^2})] \quad (\text{Equation 3-12:})$$

$$\bar{C}_{hot,\phi,j} * St(x) = \frac{\bar{C}_{hot,\phi,j}}{2} [1 + \tanh(\frac{x-x_0}{c^2})] \quad (\text{Equation 3-12})$$

where $St(x)$ is the smooth step function ([Sahin 2006](#)), x is the relative radial bin position of a projection, x_0 is the relative radian bin position such that $St(x_0) = 0.5$, c is the sharpness metric of the smooth step function $St(x)$, and $\bar{C}_{hot,\phi,j}$ is the mean projection bin value of the hot region for an angle ϕ of acquisition j . To minimize fitting error due to the non-uniformity of the projection data in the hot region, $\bar{C}_{hot,\phi,j}$ was chosen based on the highest bin value used for the fitting in each hot/cold transitions.

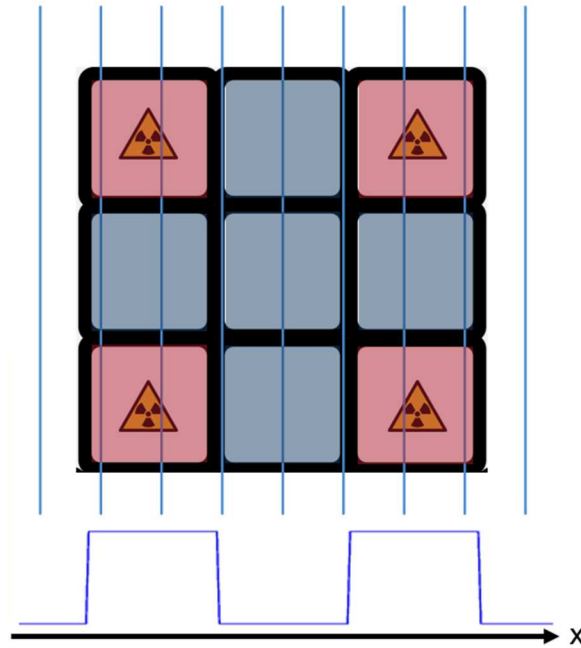


Figure 3-12. (Top) A cross-sectional representation of the 3 x 3 grid phantom. (Bottom) A representative PET projection of the 3 x 3 grid phantom, assuming perfect PET data corrections.

The total true and scattered coincidence counts of the simulations using the default SimSET materials and the continuous water density materials are shown in Table 3-6. Figure 3-13 shows the count and scatter fraction biases of individual organs between the default SimSET materials and the continuous water density materials. The count and scatter fraction biases were under 1% for all organs, with most organs well under 0.1%. Table 3-7 shows the mean ROI statistics of the brain and the liver between the materials.

Table 3-6. Global event statistics of the SimSET output. Data courtesy of Dr. Zhaoheng Xie and Dr. Xuezhu Zhang.

	SimSET default	Continuous water density	Difference
True coincidence counts	815967312	816567960	0.07%
Scattered coincidence counts	421032540	421472912	0.10%
Single scatter counts	340027386	341805466	0.52%
Double scatter counts	69058607	69402870	0.50%
Triple scatter counts	9224682	9271022	0.50%
Higher-order scatter counts	991648	993554	0.19%

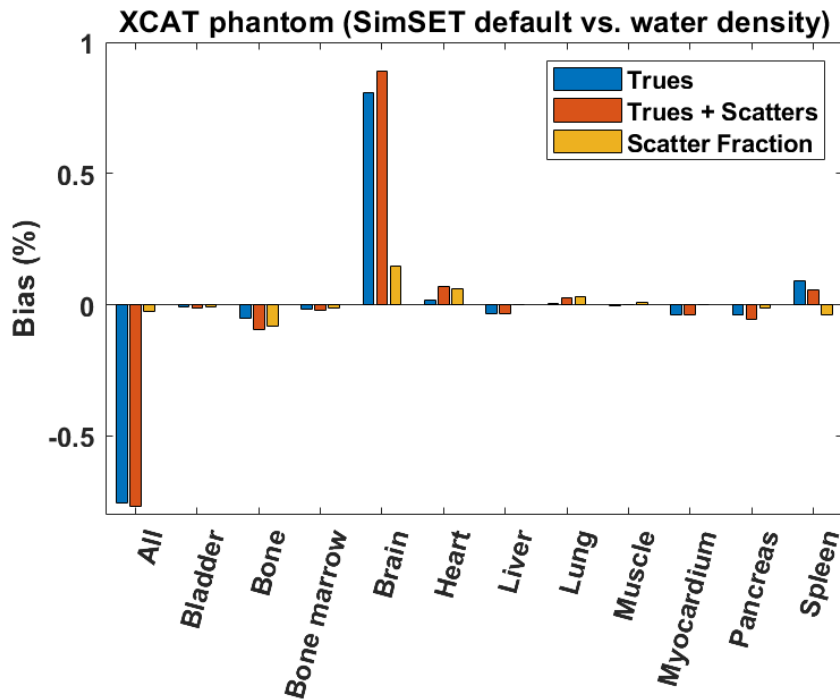


Figure 3-13. Count and scatter fraction biases of individual organs between the default SimSET materials and the continuous water density materials. Data courtesy of Dr. Zhaoheng Xie and Dr. Xuezu Zhang.

Table 3-7. Mean ROI statistics of the brain and the liver between the materials. Data courtesy of Dr. Zhaoheng Xie and Dr. Xuezu Zhang.

	SimSET default	Continuous water density	Difference
Brain	0.0834987 (a.u.)	0.0840022 (a.u.)	0.60%
Liver	0.0254816 (a.u.)	0.0261109 (a.u.)	2.47%

Figure 3-14 shows the scatter fitting of the 3 x 3 grid phantom (w/o surrounding wax) in the detector block level. Figure 3-15 shows the scatter fitting of the 3 x 3 grid phantom, surrounded with wax,

in both the detector block level and detector crystal level. Figure 3-16 shows the fitted smooth step functions in the detector crystal level using projection data from the 3 x 3 grid phantom (w/ surrounding wax). The mean value of the sharpness metric c was 1.3584 (range: 1.1324 – 1.6895).

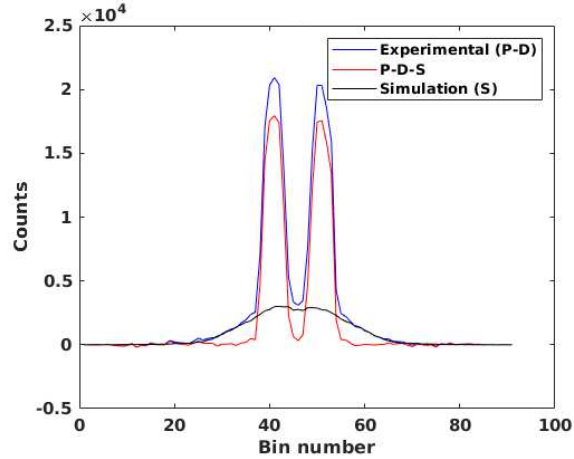


Figure 3-14. Scatter fitting (w/o surrounding wax) in the projection space, in the detector block level.

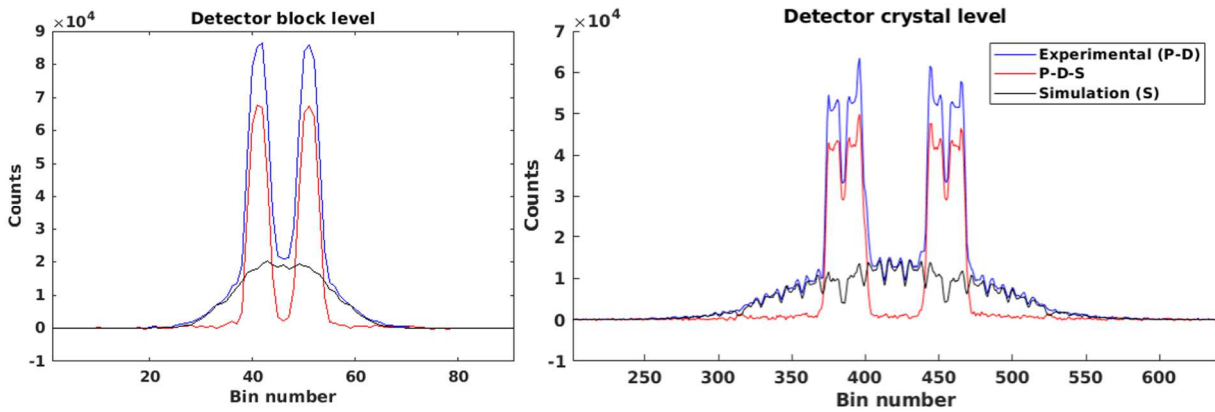


Figure 3-15. Scatter fitting (w/ surrounding wax) in the projection space. (Left) Scatter fitting in the detector block level. (Right) Scatter fitting in the detector crystal level.

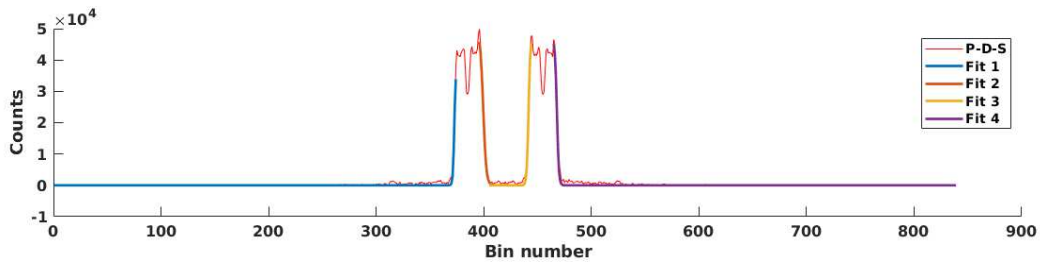


Figure 3-16. Fitted smooth step functions in the detector crystal level using projection data from the 3 x 3 grid phantom (w/ surrounding wax), with a mean c value of 1.3584 (range: 1.1324 – 1.6895).

Chapter 4 – Development and performance evaluation of a high-performance, software-based coincidence processor for total-body PET

Introduction

The 194 cm EXPLORER total-body PET scanner is approximately an order of magnitude longer than conventional PET scanners ([Bettinardi 2011](#), [Jakoby 2011](#), [Rausch 2019](#), [van Sluis 2019](#), [Spencer 2021](#)). This results in up to a 40-fold increase in effective sensitivity for total-body imaging compared to the Biograph mCT scanner ([Poon 2012](#)) largely due to the increased axial acceptance angle, from 13.2° to 57°. Previous work has shown that the singles-to-prompt ratio of a 76 kg human subject injected with 320 MBq ¹⁸F-fluciclovine and scanned in the EXPLORER scanner at 4 – 14 min after radiotracer injection was 4:1 ([Spencer 2021](#)), compared to the typical ratio of ~10:1 in conventional PET scanners ([Poon 2012](#)). The data size benefit of storing list-mode coincidence events over singles events during PET data acquisition thus becomes less significant. This motivated the work to investigate the feasibility of using a software-based coincidence processor in total-body PET where list-mode singles are stored and processed into coincidences after data acquisition.

When using a conventional hardware-based coincidence processor, only coincidence events are stored during data acquisition. The information contained in the single events are not fully recoverable from the coincidence events because some critical information (e.g. timestamp and energy information) is either partially lost or discarded. For example, when two 64-bit single events are paired into one 64-bit coincidence event, the two single event timestamps containing absolute time information are converted into a relative time difference, and the energy information may be discarded or stored with coarser bit resolutions. Single and/or coincidence events may also be entirely lost when utilizing narrower time and energy windows, or with some coincidence policies (e.g. single window (SW), killAll) where valid single and/or coincidence events are rejected, especially at higher single event count rates ([Moraes 2015](#)). Examples of coincidence policies are shown in Table 4-1. In addition, the limited buffer size of the hardware-based coincidence processor may also be susceptible to buffer overflow at higher single event count rates, leading to single and coincidence event losses.

Table 4-1. Example of coincidence policies. A coincidence policy comprises of 1) a window type, and 2) a multiple coincidence event policy (i.e. multiples policy).

Parameter	Name	Description
Window type	Single window (SW)	In this window type, single events that are inside a time window of another single event do not open its own time window for coincidence pairing.
Window type	Multiple window (MW)	In this window type, every single event opens its own time window for coincidence pairing.
Multiples policy	takeAllGoods	All valid coincidence pairs are accepted when a multiple coincidence event is detected.
Multiples policy	killAll	All valid coincidence pairs are discarded when a multiple coincidence event is detected.
Multiples policy	takeWinnerOfGoods	Only the coincidence pair with the highest total energy is accepted when a multiple coincidence event is detected.

With a software-based coincidence processor, the single events stored during data acquisition can be re-processed into coincidence events repeatedly. This provides the option to optimize the coincidence processing parameters (e.g. different energy and time windows) after data acquisition, which enables opportunities in assessing the effects of individual coincidence processing parameters on the overall quality and quantitative accuracy of the reconstructed images. With a hardware-based coincidence processor, it is impractical to repeat phantom studies for the sole purpose of optimizing coincidence processing parameters, and is unfeasible for human studies due to radiation dose concerns. The repeatability of human studies can also be sensitive to patient habitus. In contrast, datasets collected in single event acquisition mode are not subject to the same limitations and may still be useful for unforeseen applications in the coming years. For example, the list-mode singles data may be used for maximizing noise-equivalent count rate performance (NECR), or for other research applications, such as data correction involving the removal of ^{176}Lu background ([Omidvari 2020](#)) as well as inter-crystal scatter correction ([NIH 1-U01-EB029811-01](#)).

The use of a software-based coincidence processor has some drawbacks, primarily due to the potentially massive size of list-mode singles data as well as the computational time required for post-acquisition coincidence processing. For instance, the list-mode coincidence data size of a 60-min

dynamic EXPLORER healthy human PET study typically exceeds 1 TiB, and a 4:1 singles-to-prompt ratio infers a list-mode singles data size of ~4 TiB. Simulations have also shown that the EXPLORER scanner can generate 6 – 7 times more singles data than shorter clinical scanners at their optimal activity concentrations where peak NECR occur ([Poon 2012](#)). In addition, previous software-based coincidence processors were only tested to handle singles count rates of 3 – 12 Mcps ([McElroy 2005](#), [Streun 2006](#), [Goldschmidt 2013](#)). On the other hand, a 320 MBq ¹⁸F-fluciclovine EXPLORER scan produced a singles count rate of ~100 Mcps ([Spencer 2021](#)). The use of shorter-lived radionuclides, such as ¹¹C and ⁸²Rb, is therefore expected to produce even greater single event count rates. Thus, it is essential for the software-based coincidence processor to be capable of processing list-mode singles data at near real-time prior to image reconstruction to minimize total computational time.

In this chapter, we assessed our implementation of a high-performance, software-based coincidence processor that can process list-mode single events into coincidence events at a rate that enables near real-time coincidence processing, at incoming singles rates of up to 500 Mcps (for ⁸²Rb myocardial perfusion imaging the expected singles rate is ~430 Mcps). We determined the computational requirement for processing 150 M singles/s (e.g. for typical EXPLORER ¹⁸F-FDG imaging) so that near real-time coincidence processing becomes feasible at this singles count rate.

Methods

Computational requirements

Table 4-2 below provides an estimate of the amount of 64-bit list-mode singles data produced by the EXPLORER scanner. For reference, a 30-s scan at an incoming singles rate of 150 Mcps would lead to approximately 34 GiB (1 GiB = 2³⁰ bytes), or 1.1 GiB/s of data. Preliminary evaluation (using enterprise-grade computational hardware) suggested that the minimum computational hardware required for processing 150 M singles/s would involve the use of multiple server nodes equipped with multi-threaded CPUs and storage devices that can handle such rates.

Table 4-2. Estimated size of list-mode singles data produced by the EXPLORER scanner.

Singles count rate (Mcps)	Acquisition time (min)	Estimated data size (TiB*)
150	0.5	0.03

150	20	1.3
150	60	3.9
500	0.5	0.1
500	20	4.4
500	60	13.1

*1 TiB = 1024 GiB = 2⁴⁰ bytes.

Data compression and format

To manage the massive data demands of the EXPLORER scanner, compression of the list-mode data is necessary. This means that the bit values of each event parameter (e.g. energy, crystal ID, etc.) are packed tightly together to form a 64-bit event. A representation of data compression is demonstrated in Figure 4-1. Unlike the uncompressed data formats where unused bits are assigned with 0's (i.e. zero-padding) to match the byte size of a given parameter's data type, data compression minimizes the total number of unused bits. This allows more usable data to be stored in a storage device, thereby reducing computational hardware costs and data transfer times (due to the reduced file size). One drawback of data compression is that the data must be decompressed prior to data processing, which increases overall computational time.

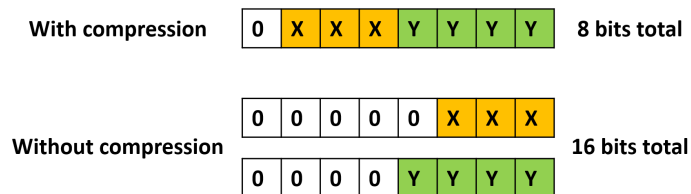


Figure 4-1. A representation of data compression. X and Y represents bit values for a given parameter in an event, and 0 represents zero-padding. Here, data compression resulted in a 50% size reduction, from 16 bits (2 bytes) to 8 bits (1 byte).

The compressed, 64-bit list-mode data format for the EXPLORER scanner was proposed (Judenhofer 2018) and is the primary data type used in our coincidence processor. The data format consists of 3 different event types – coarse timestamps, single, and coincidence events. The bit assignments of each event are shown in Figure 4-2, Figure 4-3, and Figure 4-4. Detailed information

regarding the EXPLORER list-mode data format is available in the EXPLORER singles processing framework documentation (Judenhofer 2018).

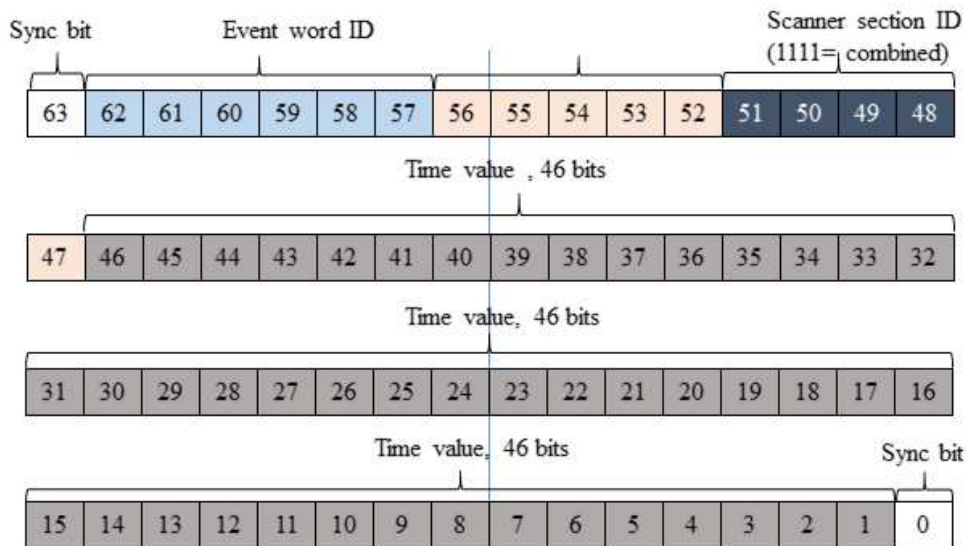


Figure 4-2. Bit assignments for a coarse timestamp (Judenhofer 2018). The bit resolution of the time value is 20 μ s.

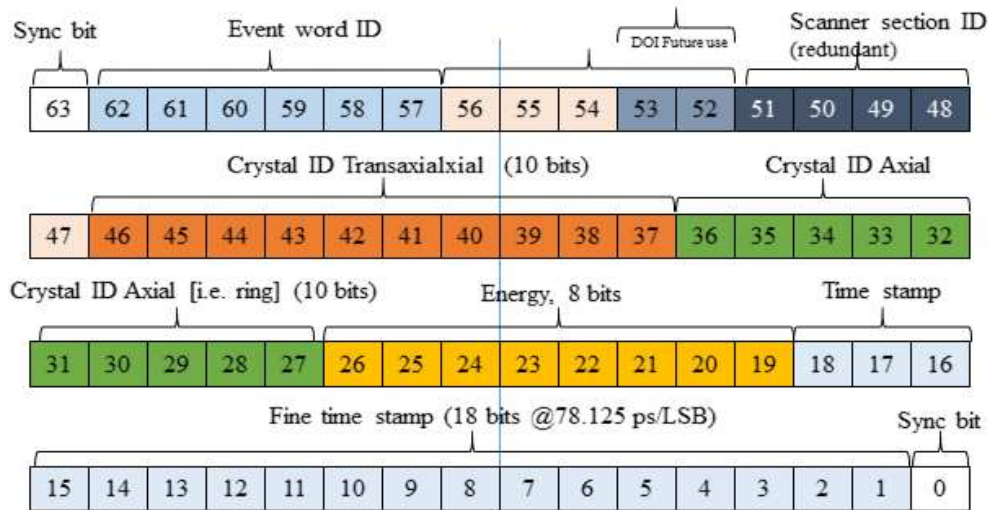


Figure 4-3. Bit assignments for a single event (Judenhofer 2018).

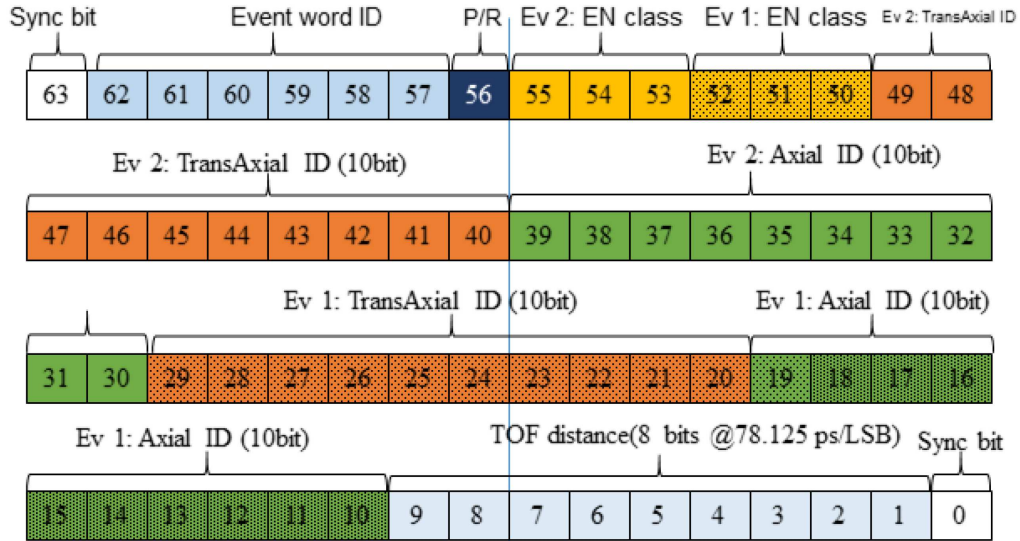


Figure 4-4. Bit assignments for a coincidence event (Judenhofer 2018).

The time value in a coarse timestamp and the fine timestamp in a single event are analogous to the minute and second hands of a clock, with bit resolutions of 20 μ s and 78.125 ps, respectively. This configuration enables the 64-bit single events to have picosecond-level time bit resolution while retaining absolute time information. It also enables the data file to be split into multiple files for batch processing with minimal losses of valid coincidences. A representation of timestamps in an EXPLORER list-mode singles file is shown in Table 4-3.

Table 4-3. A representation of timestamps in an EXPLORER list-mode singles file. Here, a fine time resolution of 80 ps was used instead of the actual 78.125 ps for ease of demonstration.

Event type	Fine time (t_{fine})	Actual time (t)
Coarse time stamp #0	0 ns	0 ns
Single event	0.080 ns	0.080 ns
Single event	0.240 ns	0.240 ns
...
Coarse time stamp #1	0 ns	20000 ns
Single event	0.160 ns	20000.160 ns
...
Coarse time stamp #2	0 ns	40000 ns
...

Design of the software-based coincidence processor

The coincidence processor we developed is command-line application (written in the C++11 standard) designed to process EXPLORER list-mode singles data files, though it can accommodate for other data formats that share similar data structures. The coincidence processor can also handle all conventional PET scanner geometries. The design overview of the coincidence processor is shown in Figure 4-5.

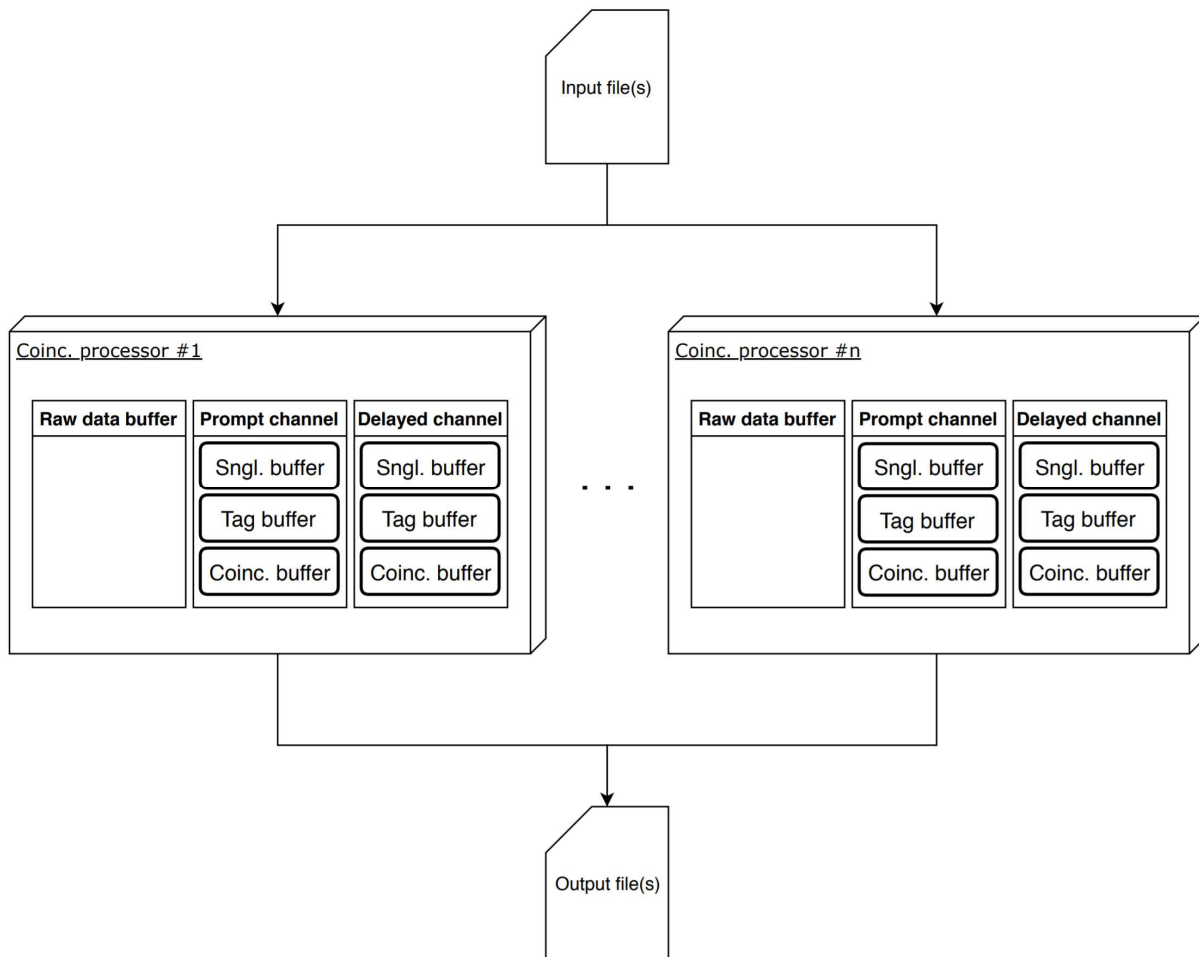


Figure 4-5. Design overview of the coincidence processor.

Our coincidence processor operates as follows: input files (i.e. a list-mode singles file and a coincidence processing parameter file) are read into multiple coincidence processor objects to generate a prompt coincidence file, a delayed coincidence file, and a log file. The number of coincidence processor

objects depends on the number of CPU threads specified in the program. Blocks of data from the list-mode singles file are read into the raw data buffer of each coincidence processor object and are processed in parallel. In each coincidence processor object, 64-bit events are extracted one at a time from the raw data buffer and are placed into appropriate buffers in both the prompt and delayed channels. Single events that fulfill the coincidence processing requirements are paired into valid coincidences and are stored into the coincidence event buffer, along with any necessary coarse timestamps. The cycle repeats until the list-mode singles file is fully processed. A command-line example of the coincidence processor is shown in Figure 4-6.

```
ekleung@explorer-r740-003: /media/ekleung/daq-003
ekleung@explorer-r740-003: /media/ekleung/daq-003$ ./singles2coincidences-20171226/
singles2coincidences --setup setup.config -i test_merge.dat --NTHREADS 48

Program singles2coincidences is starting...
SETUP_FILE_PATH command-line override detected. New value: setup.config
INPUT_FILE_PATH command-line override detected. New value: test_merge.dat
NTHREADS command-line override detected. New value: 48
PROMPT_FILE_PATH is not defined. Default value: prompt.dat
DELAY_FILE_PATH is not defined. Default value: delay.dat
STATS_FILE_PATH is not defined. Default value: stats.txt
CONVERT_ROOT_SINGLES is not defined. Default value: false
Actual time window used: 7.96875e-09 s
Actual delay time used: 5e-07 s
Actual EXPLORER_TIME_TAG_INCREMENT integer: 256000

EXPLORER 64-bit list-mode file test_merge.dat detected.
Number of threads available: 48
Number of threads used: 48
Number of data entries in this file: 19534536

Begin coincidence processing...
=====
Using solution 2
19534536 of 19534536 entries processed
=====

Singles: 19217936
Qualified Singles: 19217936
Prompt: 809485
Delay: 281198
Prompt - Delay: 528287
Multiples from Prompt: 27081
Triples from Prompt: 26380
Quadruples from Prompt: 693
Quintuples from Prompt: 8
ntuples from Prompt: 0
Multiples from Delay: 12727
Triples from Delay: 12498
Quadruples from Delay: 225
Quintuples from Delay: 4
ntuples from Delay: 0
Number of tags in prompt: 316294
Number of tags in delay: 316297
Creating/Opening stats file stats.txt...

It took 0.446676 s to complete this operation.

ekleung@explorer-r740-003: /media/ekleung/daq-003$
```

Figure 4-6. Command-line example of the coincidence processor.

The key parameters of our coincidence processor include 1) an energy window, 2) a fixed time window, 3) a coincidence policy, 4) a geometric window, and 5) a variable time window. The parameters are specified in the configuration file of the coincidence processor, as shown in Figure 4-7.

```
ekleung@explorer-r740-003: /media/ekleung/daq-003
ekleung@explorer-r740-003:/media/ekleung/daq-003$ cat setup.config
# Coincidence processing parameters
# LLD, ULD in MeV
# timeWindow, delayWindow in seconds (s)
# coincidencePolicy (takeAllGoods or killAll only)

# Scanner specifications
# TIME_TAG_INTERVAL, CFD_RESOLUTION in seconds (s)
# MIN_ENERGY, MAX_ENERGY represents the dynamic range
# All ENERGY parameters in MeV
# *XIAL_ARRAY_DIM represents the block crystal array size
# BLOCKS_PER_RING represents # block crystals per ring
# MIN_TRANSAXIAL_DIFF is based on block ring
# MAX_AXIAL_DIFF is based on crystal ring

LLD=0.430
ULD=1
TIME_WINDOW=8.0082e-9
DELAY_TIME=500e-9
MIN_TRANSAXIAL_DIFF=4
# 1023 is not the right number but should work fine
MAX_AXIAL_DIFF=1023

COINCIDENCE_POLICY=takeAllGoods

TIME_TAG_INTERVAL=20e-6
CFD_RESOLUTION=78.125e-12
MIN_ENERGY=0.2
MAX_ENERGY=0.712
ENERGY_OFFSET=0.2
ENERGY_RESOLUTION=0.002
TRANSAXIAL_ARRAY_DIM=35
# AXIAL_ARRAY_DIM should not matter FOR non-ROOT files
AXIAL_ARRAY_DIM=6
BLOCKS_PER_RING=24

# VARIABLE COINCIDENCE TIME WINDOW
TX_FOV=0.686
AXIAL_CRYSTAL_PITCH=2.85e-3
COINCIDENCE_TIMING_RESOLUTION=409e-12
ekleung@explorer-r740-003:/media/ekleung/daq-003$
```

Figure 4-7. Example of a coincidence processor configuration file.

The coincidence processing algorithm is described below. An energy window is first applied to the data to discard any single events outside the energy window. Next, a fixed time window is applied to every energy-qualified single. This procedure is typically referred to as the multiple window (MW) method ([Oliver 2009](#), [Morales 2015](#), [Strydhorst 2016](#)). Then, we used *MW*, *takeAllGoods* (i.e. accepting all valid coincidences) as our coincidence policy for this assessment. Finally, a geometric window is applied to the remaining coincidences. A geometric window limits the range of LORs accepted based on the axial acceptance angle (in the form of maximum axial crystal difference) and transaxial FOVs (in the form of

minimum and maximum transaxial crystal differences). Some of the coincidences are discarded in this step if their LORs fall outside the range of allowed axial and transaxial crystal differences. A visual example of the coincidence processor handling energy-qualified singles is shown in Figure 1-2. A pseudocode of the coincidence processing algorithm is shown in Figure 4-8.

```

// DEFINITIONS
// A qualified single is a single that is accepted by the energy window.
// A reference single is a qualified single that opens a time window.
// A non-reference single is a qualified single that is inside a reference single's time window.

for each reference_single do
  for non-reference_singles in the time window do
    if LOR(ref,non-ref) is outside the transaxial FOV then
      continue; // coincidence event is rejected
    else if LOR(ref,non-ref) is greater than the maximum crystal ring difference then
      continue; // coincidence event is rejected
    else if time_difference(ref,non-ref) is greater than the variable time window then
      continue; // coincidence event is rejected
    else
      record_coincidence_pair(ref,non-ref); // coincidence event is accepted
    end
  end
end
end

```

Figure 4-8. Pseudocode implementation of the coincidence processing algorithm.

As shown earlier in Figure 1-2, a wider, primary fixed time window is required to ensure that the more oblique LORs are considered. However, the number of random coincidences increases as a result. To reduce the number of random coincidences due to the increased axial acceptance angle, the coincidences are processed after the geometric window with a secondary, variable time window, which depends on the axial positions of the 2 crystals forming the LOR ([Poon 2012](#)). The variable time window

$\tau(R)$ is defined using $\tau(R) = \frac{\sqrt{T^2+(R \cdot W)^2}}{c} + 3 \cdot P$ (Equation 4-1:

$$\tau(R) = \frac{\sqrt{T^2+(R \cdot W)^2}}{c} + 3 \cdot P \quad (\text{Equation 4-1})$$

where R is the crystal ring difference, T is the transaxial FOV (in m), W is the axial crystal pitch (in m), P is the coincidence timing resolution (in s), and c is the speed of light (in m/s). A coincidence timing resolution of 409 ps was chosen for this assessment ([Lv 2017](#)).

As mentioned earlier, the coincidence processor utilizes multiple CPU threads to improve performance by splitting the list-mode singles file into multiple data sections and processing each section simultaneously. The coincidence processors share a common read and write thread and use synchronous file I/O. Methods that involve splitting the file typically lose some – although most likely negligible depending on the size of the coincidence processing buffer – valid coincidences since the single events at the end of one section are not paired with the single events at the beginning of the following section ([Goldschmidt 2013](#), [Strydhorst 2016](#)). Our coincidence processor ensures that all potential coincidences are considered by using a reserve buffer that overlaps with adjacent data sections without processing the same reference single (i.e. the single event that opens the primary, fixed time window) more than once. The reserve buffer is sufficiently large to ensure that every valid coincidence event is recorded. This effectively eliminated the boundaries between data sections. Table 4-4 shows a representation of the reserve buffer. Details regarding the compilation environment and specific functions used for the coincidence processor are shown in Table 4-5.

Table 4-4. A representation of the reserve buffer in the coincidence processor. The green boxes represent single events in the reserve buffer. Note: events in the reserve buffer are not treated as reference single events.

Beginning of k^{th} buffer	Beginning of $(k+1)^{\text{th}}$ buffer
...	$(m+1)^{\text{th}}$ single event
$(m-1)^{\text{th}}$ single event	$(m+2)^{\text{th}}$ single event
m^{th} single event	$(m+3)^{\text{th}}$ single event
$(m+1)^{\text{th}}$ single event	...
...	$(m+n)^{\text{th}}$ single event
$(m+n)^{\text{th}}$ single event	...
End of k^{th} buffer	End of $(k+1)^{\text{th}}$ buffer

Table 4-5. Compilation environment and major functions used for the coincidence processor.

Parameter	
Operating system	Ubuntu 16.04 LTS
Programming language	C++11
C++ compiler	GCC 5.4
Compilation flags used	--std = c++11 and -pthread
C++ library used	Standard C++ library only
C++ class used for multi-threading	std::thread
C functions used for file I/O	fread() and fwrite()
C++ class used for time measurements	std::chrono::steady_clock

Test data

List-mode PET singles data with increasing singles count rates (from 50 Mcps to 500 Mcps) were simulated using GATE v8.0. The GATE installation was checked using a Poisson validation protocol based on the χ^2 statistic ([Tries 1999](#)) for a Biograph mCT-like scanner geometry (the simulation parameters are shown in Table 4-6). Next, the simulations for the coincidence processing performance evaluation included the EXPLORER scanner geometry and a water-based cylindrical phantom (16 cm diameter x 150 cm long) with a centered line source (6 mm diameter x 150 cm long), similar to a NEMA NU 2 scatter phantom. The specifications of the LYSO crystals used in the simulations were obtained from Crystal Photonics, Inc. (Sanford, FL, United States) via private communication. The radioactive background from the LYSO crystals was also simulated and incorporated into the test data. No dead-time was simulated in the scanner. Simulation parameters of the test data are shown in Table 4-7.

Table 4-6. Simulation parameters for the Poisson validation protocol for a Biograph mCT-like scanner geometry.

Parameter	
# trials (n)	100 for each activity concentration
# mCT detectors used	48-block ring x 4 rings
Time window, delay time, energy window	4.1 ns, 500 ns, 435 – 650 keV
Transaxial FOV, axial FOV restrictions	780 mm, none
Dead time	None
Radioactive source, type, activity	¹⁸ F, NEMA NU 2 scatter phantom, 2.5 – 50 kBq/cc
Simulation time	Varies – time set until ~1 M singles acquired

Table 4-7. Simulation parameters of the test data. Note: the parameters were defined based on the expected EXPLORER scanner specifications and are not identical to the actual EXPLORER scanner specifications.

Parameter	
Crystal size	$2.76 \times 2.76 \times 18.1 \text{ mm}^3$
Crystal pitch	2.85 mm transaxial \times 2.85 mm axial
# crystals per block	7 transaxial \times 6 axial
# block detectors	120-block ring \times 112 rings
Timing resolution	409 ps
Energy range	250–712 keV
Energy resolution	11.7% @ 511 keV
Dead time	None
Phantom	Water-based cylindrical phantom (16 cm dia. \times 150 cm long) with centered line source
Radioactive source	Generic 511 keV back-to-back line source (6 mm dia. \times 150 cm long)
Source activity	40–730 MBq
Resultant incoming singles rate	49–487 Mcps (including \sim 21 Mcps LYSO background)
LYSO density	7.1 g cm^{-3}
LYSO % by mass	Lu = 71.447%, Y = 4.034%, Si = 6.371% and O = 18.148%
LYSO background	400 Bq cc^{-1}
# detected singles simulated	\sim 2 billion singles for each singles data rate

Coincidence processing performance evaluation

The singles test data generated from GATE were stored in the ROOT format ([Brun 1997](#)), then converted into the 64-bit singles format (as shown in Figure 4-3) and processed using the coincidence processing parameters shown in Table 4-8. A Dell PowerEdge R730 rack server with dual Intel Xeon E5-2650 v4 CPUs and 128 GiB memory was used for this evaluation. The coincidence processing performance was obtained by dividing the number of single events in the list-mode file by the program execution time. For each incoming singles data rate, the same list-mode singles file was repeatedly processed 10 times to obtain the mean coincidence processing performance. We reset the file cache after each run to ensure the list-mode file was loaded from the storage drive instead of the memory.

Table 4-8. Parameters used for the coincidence processor. Note: the parameters were defined based on the expected EXPLORER coincidence processor specifications and are not identical to the actual EXPLORER coincidence processor specifications.

Parameter	
Energy window	430–712 keV
Time window	Fixed (8.0 ns) followed by variable (3.5–8.0 ns)
Transaxial FOV restrictions	686 mm
Axial FOV restrictions	Restricted via the variable time window
Coincidence policy	Multiple window, takeAllGoods

The evaluation of the coincidence processor was split into the following categories: 1) storage type and 2) overall performance.

Storage type

An Intel 750 series PCIe 3.0 NVMe SSD (model SSDPEDMW012T4X1) and a high-performance Dell PERC H730 integrated RAID controller w/ 8, Seagate 8TB Enterprise HDDs (model ST8000NM0075) in a RAID 6 configuration were compared to determine if differences in performance could be observed between the 2 storage types. We opted to not evaluate a SATA SSD due to the limited physical space available on the rack server, and because a PCIe NVMe SSD significantly outperforms a SATA SSD in terms of I/O performance due to the increased bus bandwidth. This type of evaluation is useful for evaluating maximum real-world performance of the coincidence processor by accounting for potential bottlenecks caused by the storage devices. On the other hand, a RAID 6 HDD array configuration was evaluated since it is one of the more reliable, cost-effective, and physically space-efficient options when maximum performance is not the utmost priority. We also evaluated the native performance of the coincidence processor by loading the data into memory prior to coincidence processing to determine if file I/O may be the primary performance bottleneck of the software.

Overall performance

The coincidence processor was compiled and run with varying number of CPU threads (up to 48 threads) to determine if a CPU performance bottleneck can be observed in the coincidence processor. We also assessed the overall performance effects of processing multiple data files simultaneously (which is useful for batch processing) between the 48 CPU threads.

Results

Poisson validation

Figure 4-9 shows the reduced χ^2 statistics of prompt, true, scattered, and random coincidence events identified according to their annihilation event IDs from the Poisson validation test of the Biograph mCT-like scanner. For both prompt and random coincidence events, the reduced χ^2 statistic became higher as the activity concentration increased. Figure 4-10 shows the ratios of multiple coincidence events in the prompt and delayed coincidence data.

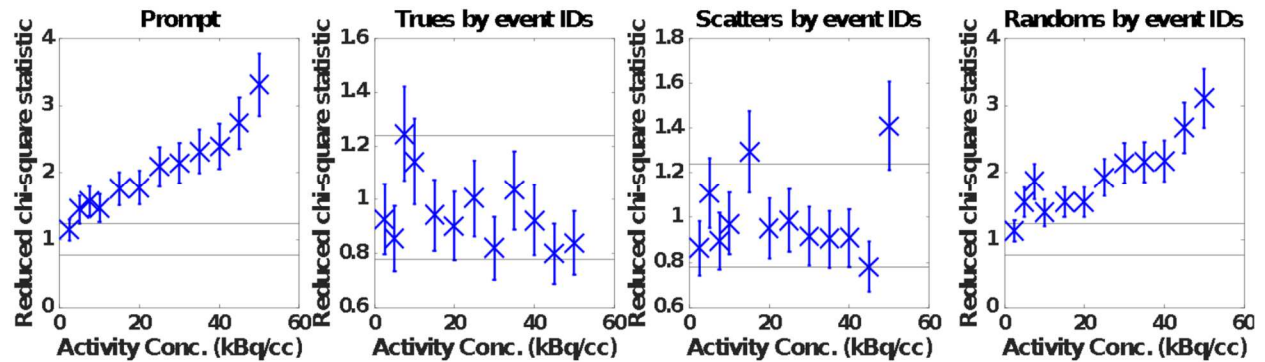


Figure 4-9. Reduced χ^2 statistics of various types of coincidences from the Biograph mCT-like simulations.

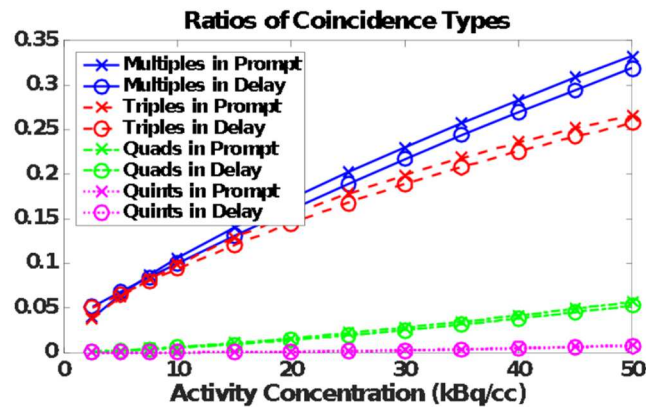


Figure 4-10. Ratios of multiple coincidences in the prompt and delayed coincidences from the Biograph mCT-like simulations.

Storage type

Figure 4-11 shows the overall coincidence processing performance of the coincidence processor using increasing number of CPU threads while processing a single file. For both the PCIe SSD and HDDs in RAID 6, the coincidence processor processed approximately 2.5 and 1.5 M singles/s at incoming singles count rates of approximately 150 and 500 Mcps when processing a single file using a single CPU thread, respectively. If the data was pre-loaded into the memory, the performance increased to 5.7 and 3.3 M singles/s, an increase of 128% and 120%, respectively.

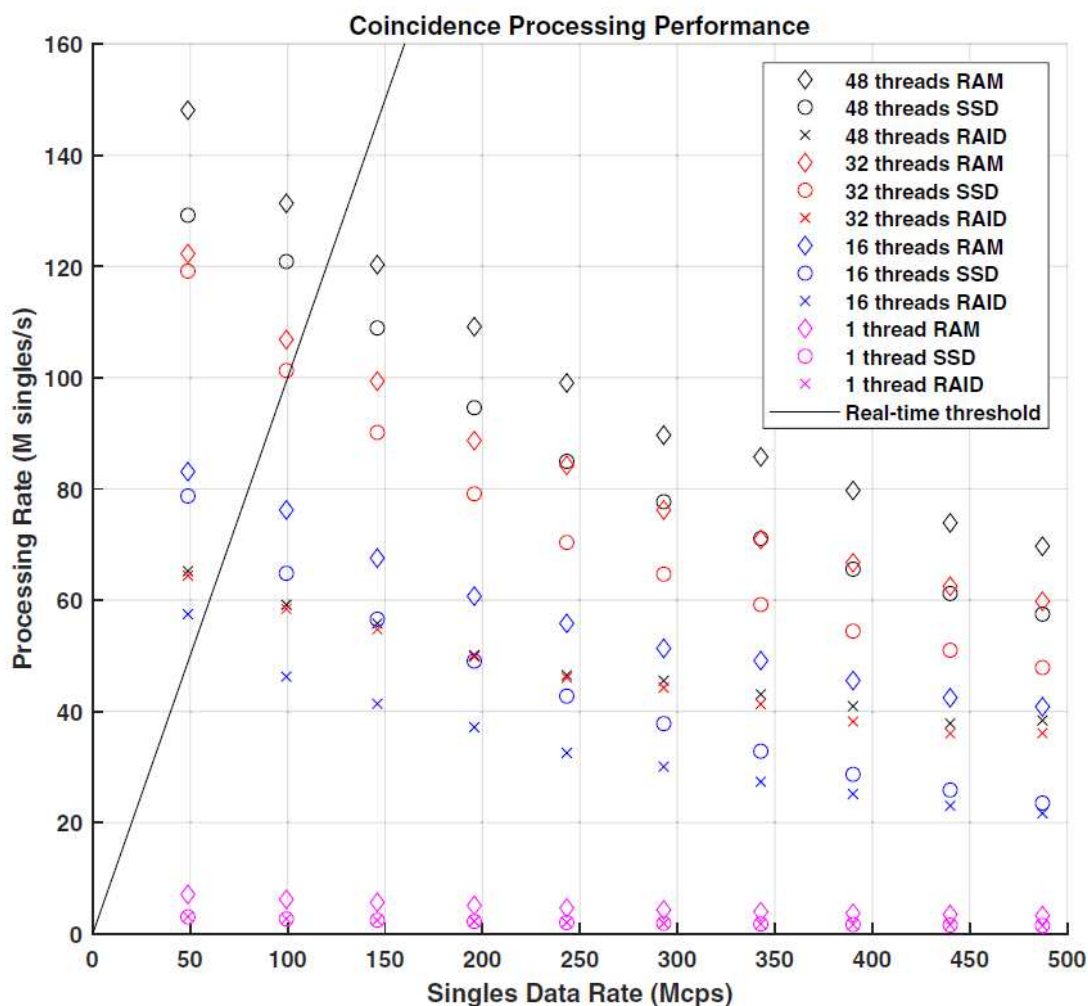


Figure 4-11. Overall coincidence processing performance of the coincidence processor using increasing number of CPU threads while processing a single file. The average coefficient of variation (CV) of the data points, calculated over 10 repetitions, was 2.0%. Data points above the

real-time threshold reflect data rates that can be processed at near real-time with 1 computer node.

When processing a single file using all 48 threads, the PCIe SSD configuration outperformed the RAID 6 HDDs configuration by 95% (at 109 M singles/s processing rate) and 50% (at 57 M singles/s processing rate) at incoming singles count rates of approximately 150 and 500 Mcps, respectively. The performance increased (with plateauing performance gain) as the number of CPU threads increased for both the PCIe SSD and the HDDs in RAID 6. Pre-loading the data into the RAM led to a performance increase of 10% and 12% over the PCIe SSD configuration, at 120 and 70 M singles/s, respectively.

Number of files

Figure 4-12 shows the coincidence processing performance of the coincidence processor with increasing number of data files. When using all 48 CPU threads, a significant difference in performance could be observed between the PCIe SSD and HDDs in RAID 6. In addition, the overall coincidence processing performance increased with increasing number of files processed in parallel with the PCIe SSD configuration, while the coincidence processing performance degraded when multiple files were processed in parallel with the HDDs in RAID 6 (especially when 3 files were processed in parallel).

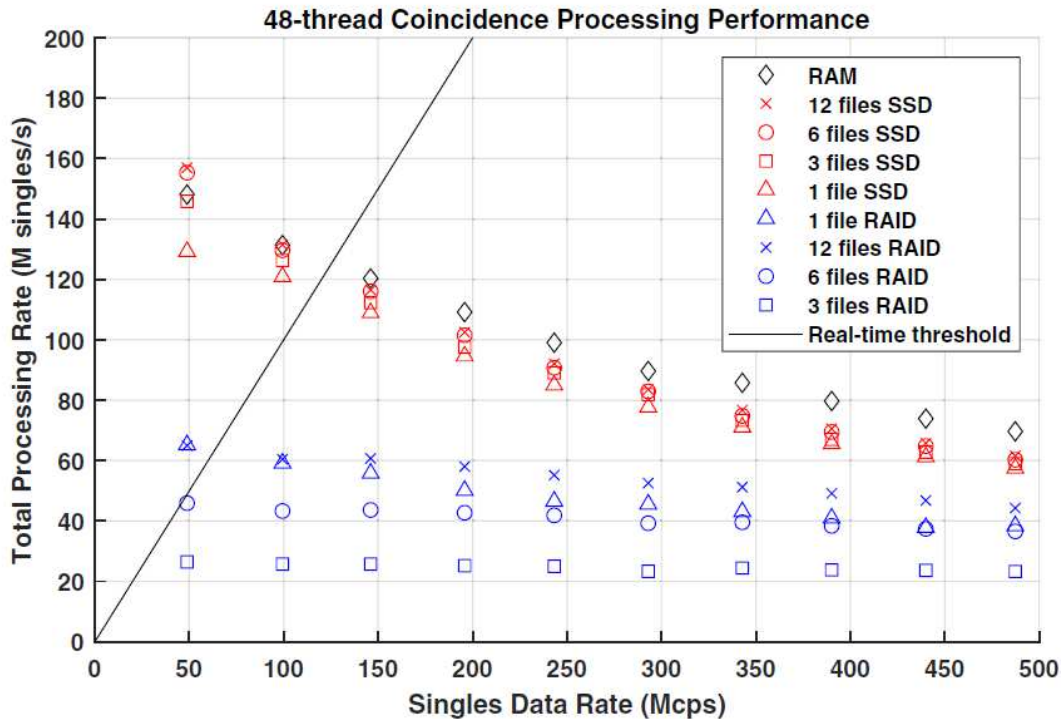


Figure 4-12. Coincidence processing performance of the coincidence processor with increasing number of files. The average coefficient of variation (CV) of the data points, calculated over 10 repetitions, was 3.2%. Data points above the real-time threshold reflect data rates that can be processed at near real-time with one computer node.

Discussion

From the Poisson validation test, the prompt and random coincidences had greater variance than would be predicted by Poisson statistics, which may be explained by the presence of multiple coincidences. This may have implications for PET data quality estimations using NECR methods which assume a Poisson distribution for random coincidences and may especially be an important consideration for long axial FOV PET scanners. However, this significance requires further investigation.

For the coincidence processing performance evaluation, we have shown that there was a noticeable performance gain by using a PCIe SSD over enterprise-grade HDDs in RAID 6. In addition, when multiple files were processed in parallel, the HDDs in RAID 6 suffered performance degradation (especially when 3 files were processed in parallel) compared to the PCIe SSD configuration. This was

likely due to the RAID controller struggling with multiple parallel and uncoordinated I/O requests from multiple independent processes. We suggest it was not an issue when processing a single file because sequential I/O requests originated from the same process. To overcome this limitation in HDDs, the I/O from all processes would need to be properly sequenced. However, this would only be possible at the expense of increased complexity of the code, which may not be justifiable especially since SSDs have become relatively affordable in recent years.

New computational hardware (including faster CPUs with more threads and higher performance storage devices) have been released into the market since our performance assessment. In particular, the next-generation PCIe 4.0 NVMe SSDs are expected to outperform the PCIe 3.0 counterpart we tested by a factor of 2 – 4. A drawback of utilizing SSDs in general, however, is that they have a limited lifespan governed by the number of write cycles that the SSD can handle, depending on the type of flash cell used ([Schroeder 2016](#)). Thus, the consumable nature of SSDs needs to be considered when estimating the total cost of the computational hardware, for example in the form of recurring cost. Alternatively, HDDs with dual actuators are also available on the market since 2021, which may outperform standard HDDs by a factor of 2, however the reliability of such drives is currently unclear. In both cases, although a noticeable performance improvement can be expected, the performance assessment is recommended to be repeated with the new hardware. Another way to further increase the I/O performance is to use a RAID 0 configuration in comparison to a RAID 6 configuration, at the expense of increased risk of data loss due to the lack of redundancy in a multi-drive configuration. The optimal storage configuration will depend on the budget, storage requirement and the level of accepted risk in the event of data loss.

With our test configuration, the most effective way to maximize the coincidence processing performance was to simultaneously process 6 or 12 files using the available 48 CPU threads for the PCIe SSD configuration. Figure 4-13 shows the number of computer nodes needed to achieve near real-time coincidence processing for a given incoming singles data rate. In practice, however, only 1 file should be processed at a time on each computer node to minimize potential complications (e.g. accidentally filling the storage space to 100% capacity and potentially leading to system crashes). The performance benefit gained by processing multiple files is relatively minimal, and in a research environment (as compared to a

production environment) the speed benefits may become practically negligible due to the lower % time utilization of computational resources.

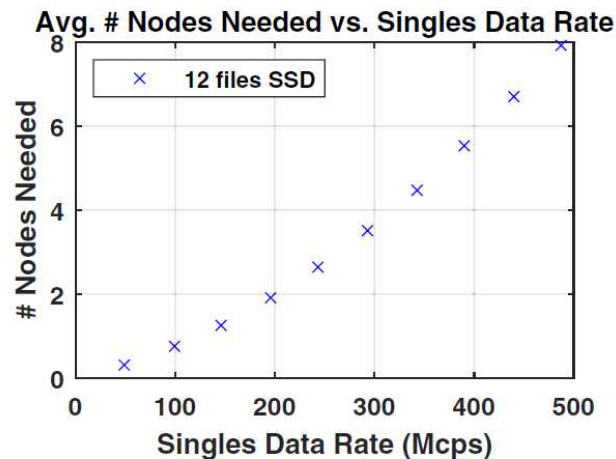


Figure 4-13. Number of computer nodes needed to achieve near real-time coincidence processing.

While it is possible to store data directly in memory and process events in real-time as an alternative to SSD storage, for larger systems (such as the EXPLORER scanner) it can lead to a less flexible software implementation depending on factors such as the pre-processing requirements of raw data (e.g. merging and sorting singles data from multiple scanner sections in chronological order). Also, with our setup we showed that the maximum performance gain over the PCIe SSD configuration (when processing 1 file) was only about 10%. At a single event count rate of 50 and 100 Mcps, the PCIe SSD configuration (when processing 6 or 12 files) marginally outperformed the RAM configuration. We suggest that this may have been due to the overhead penalty from launching multiple threads simultaneously after pre-loading the entire data file into RAM, which may not have been an issue at higher singles count rates where coincidence processing comprises the bulk of the computational time.

In cases where the data acquisition and real-time coincidence processing are performed on the same disk, we expect the PCIe SSD configuration to be better suited for handling multiple independent I/O requests when compared to the RAID HDD configuration – as we have shown that the RAID HDD configuration performed poorly when handling multiple uncoordinated I/O requests in parallel.

Although dead-time was not modeled in the simulations, we expect the presence of dead-time to improve performance at higher rates as it will reduce the number of single events for coincidence processing.

Finally, another consideration when estimating the performance of the coincidence processor for a given scanner geometry is the event count ratios of data since the contribution of multiple coincidences may reduce the coincidence processing performance. For example, Figure 4-14 shows the singles-to-qualified-singles, qualified singles-to-prompt ratios, and the prompt-to-multiples ratios of the experiment. At a singles data rate of approximately 150 Mcps, the singles-to-qualified-singles, qualified singles-to-prompt, and prompt-to-multiples ratios in our simulation setup were 2.0:1, 3.2:1 and 3.4:1, respectively.

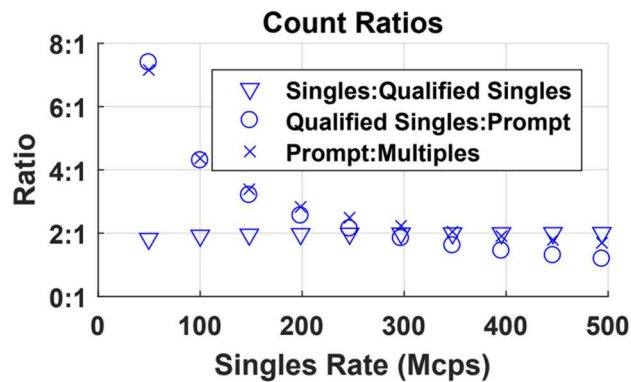


Figure 4-14. Singles-to-qualified singles, qualified singles-to-prompt, and prompt-to-multiples ratios of the test data.

Conclusion

We developed a high-performance, software-based coincidence processor for the EXPLORER total-body PET scanner to process its list-mode singles data. To process single events at an incoming single event count rate of 150 Mcps, we determined that the use of 2, 48-thread computer nodes with dual Intel Xeon E5-2650 v4 CPUs and a PCIe 3.0 NVMe SSD would enable near real-time coincidence processing.

Chapter 5 – Monte Carlo sensitivity study of the NeuroEXPLORER dedicated brain PET scanner

Introduction

The commercialization of the EXPLORER total-body PET/CT scanner has led to a resurgence of interests in a commercial, high-sensitivity, dedicated brain PET scanner. As a successor of the 20+ year-old High Resolution Research Tomograph (HRRT) brain PET scanner (the first LSO-based human PET scanner developed in the late 1990s) ([Schmand 1999](#), [de Jong 2007](#)), the NeuroEXPLORER (NX) dedicated brain PET/CT scanner aims to outperform the HRRT scanner by having 1) a 10-fold gain in effective sensitivity from both increased axial coverage and TOF capability, 2) improved spatial resolution (< 2 mm transaxial resolution), 3) integrated head motion correction, and 4) ultra-high resolution panel detectors positioned near the neck for carotid artery imaging (Carson 2021). Improvements in these areas may lead to better image quality and quantification, reduce radiation doses and motion artifacts, as well as help obtaining more quantitatively accurate carotid artery image-derived input function for kinetic modeling without the need for the more invasive arterial blood sampling methods. With the ability to quantify smaller brain structures, new opportunities to study underexplored areas such as brain development and small dynamic changes in the brain for neurodegenerative diseases may arise.

To estimate the sensitivity gains of the NX scanner over other dedicated brain and conventional PET scanners as part of the NX grant proposal ([NIH 1-U01-EB029811-01](#)), we performed a series of Monte Carlo simulations across a variety of digital phantoms.

Methods

Simulation software and data processing

Geant4 Application for Tomographic Emission (GATE) v8.2 (with the Geant4 v10.05.p01 physics engine) was used for the simulation study ([Jan 2004](#), [Strydhorst 2016](#)). Prior to the study, the simulation package was checked for known statistical bugs caused by installation parameters, using an in-house Poisson validation protocol (Leung 2016) discussed earlier in Chapter 4.

The simulation output was stored in ROOT ([Brun 1997](#)) v6.16 format and was processed to extract decay and list-mode coincidence data for further processing.

Scanner geometries

Since the NX scanner was not constructed prior to the submission of the grant proposal, effort was put into performing sensitivity simulations for existing PET scanners (e.g. the Mini EXPLORER II scanner), and then use the simulation framework to predict the sensitivity performance of the expected NX geometry.

Five scanners were simulated: 1) the Mini EXPLORER II scanner, 2) the NX scanner, 3) the HRRT scanner, 4) the Biograph Vision scanner, and 5) the CareMiBrain scanner. The geometries of the scanners are shown in Figure 5-1 and Figure 5-2.

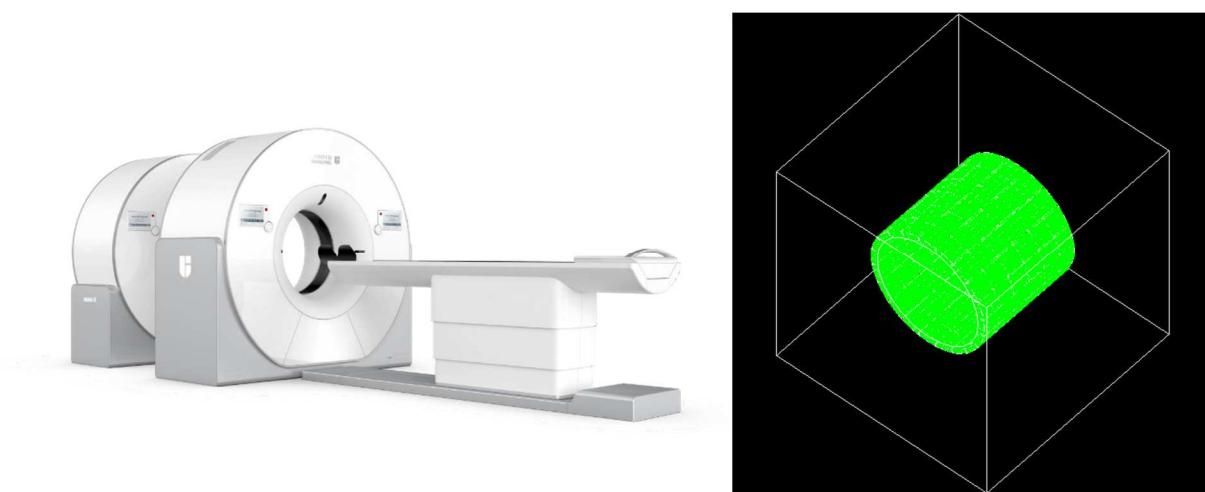
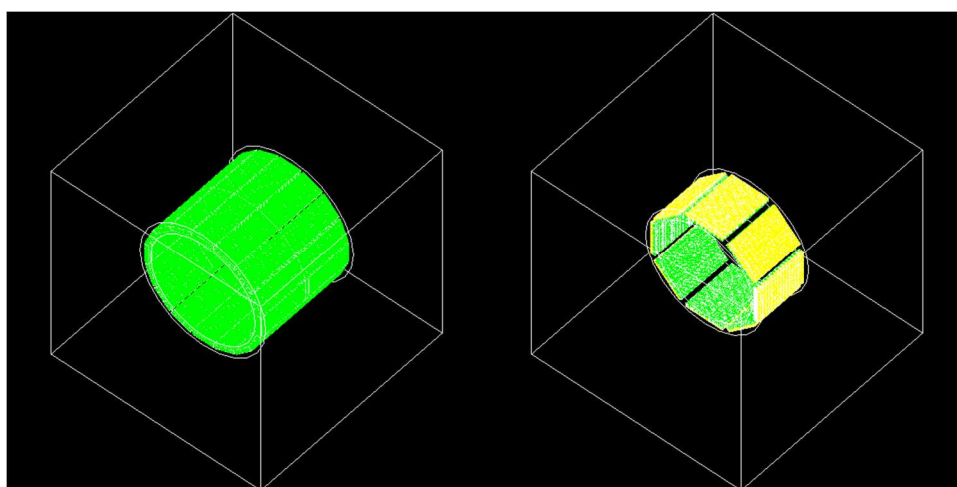


Figure 5-1. (Left) Illustration of the NX scanner. Image courtesy of Dr. Hongdi Li (UIH America).

(Right) Geometry of the NX scanner (shoulder cutouts not included).



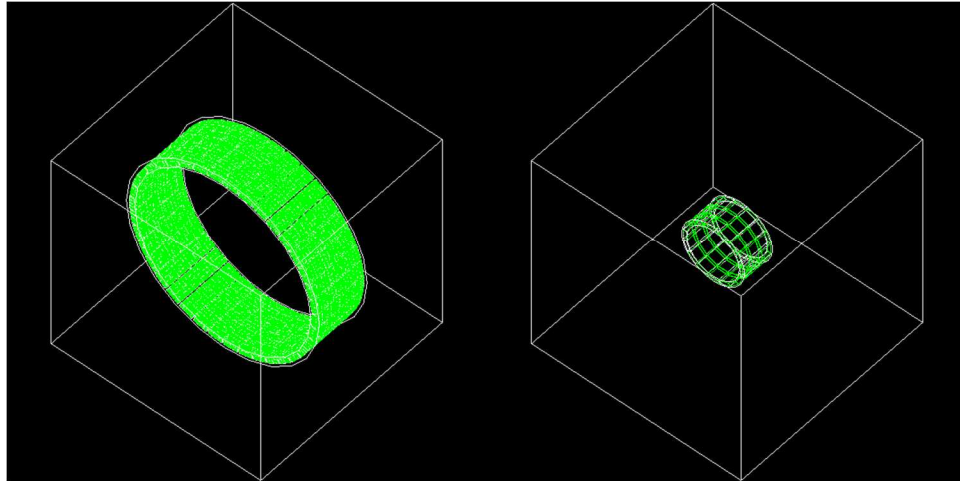


Figure 5-2. Geometry of the (Top Left) Mini EXPLORER II, (Top Right) HRRT-D, (Bottom Left) Biograph Vision, and (Bottom Right) CareMiBrain scanners, respectively.

The SiPM-based Mini EXPLORER II PET/CT scanner (which is now marketed as the [uBioEXPLORER preclinical PET/CT scanner](#)) was developed as a small-scale version of the EXPLORER scanner as a technology demonstrator ([Berg 2018](#), [Lv 2019](#)). It has an axial FOV of 483 mm and a crystal face-to-face (F2F) diameter of 520 mm. The scanner is primarily designed for use in total-body veterinary and non-human primate PET imaging.

The SiPM-based NX TOF/DOI-PET/CT scanner has an axial FOV of 495 mm and a crystal F2F diameter of 499 mm. The scanner is designed for use as a dedicated brain PET imager. Despite its similar size to the Mini EXPLORER II scanner, the NX scanner incorporates shoulder cutouts to accommodate larger human subjects and thus allow the brain to be positioned at the center FOV to maximize brain sensitivity. It also features 2, ultra-high spatial resolution panel detectors to improve quantification of the carotid arteries, as well as smaller scintillator crystals (compared to the Mini EXPLORER II scanner) for improved transaxial spatial resolution.

For the study, we also simulated the NX scanners with longer, 25 mm LYSO crystals to assess the sensitivity gain over the proposed, 18.1 mm long LYSO crystals. The 2 panel detectors were not simulated in the study.

The PMT-based HRRT PET scanner has an axial FOV of 252 mm and a crystal F2F diameter of 469 mm ([Wienhard 2002](#), [de Jong 2004](#)). The scanner was designed to be used as a dedicated brain

PET scanner; however, it is no longer being manufactured. The scanner utilizes a ^{68}Ge rotating rod source for attenuation correction.

Three versions of the HRRT scanner were built – the HRRT-DC (7.5+7.5 mm long LSO+LSO or LSO+GSO crystals), HRRT-S (7.5 mm long LSO crystals) and the HRRT-D (10+10 mm long LSO+LYSO crystals). The scanner simulated in this study is the HRRT-D scanner.

The SiPM-based Biograph Vision TOF-PET/CT scanner was cleared by the FDA in 2018 as a successor of the PMT-based Biograph mCT Flow TOF-PET/CT scanner ([van Sluis 2019](#), [press release](#)). It has an axial FOV of 263 mm and a 780 mm bore diameter. Designed to be a PET scanner for whole-body clinical imaging, the Biograph Vision has a reduced solid angle coverage, compared to other dedicated brain PET scanners.

The SiPM-based CareMiBrain DOI-PET scanner is a dedicated brain PET scanner that utilizes monolithic LYSO crystals ([Moliner 2019](#)). It has an axial FOV of 154 mm and a crystal F2F diameter of 256 mm. The attenuation correction of the CareMiBrain scanner is based on segmenting the reconstructed image volume with 3 materials considered: 1) air, 2) bone, and 3) tissue.

Table 5-1 summarizes the specifications of each scanner simulated in GATE. Some parameters may not reflect the actual scanner configuration since some of the information was not publicly available.

Table 5-1. Specifications of the simulated PET scanners.

	Mini EXPLORER II	NX	HRRT-D	Biograph Vision	CareMiBrain
F2F* diameter (mm)	520	499	469	849	256
Axial FOV (mm)	483	495	252	263	154
Crystal size (mm x mm x mm)	2.76 x 2.76 x 18.1	1.52 x 3.1 x 18.1	2.1 x 2.1 x (10+10)	3.2 x 3.2 x 20	50 x 50 x 15
Crystal pitch (mm x mm)	2.85 x 2.85	1.6 x 3.2	2.4 x 2.4	3.3 x 3.3	50 x 50
Block array size	7 x 6 (transaxial x axial)	16 x 8 (transaxial x axial)	8 x 8 (transaxial x axial)	5 x 5 (transaxial x axial)	1 x 1 (transaxial x axial)
Block pitch (mm x mm)	20.03 x 17.17	25.63 x 25.63	19.3 x 19.4	16.4 x 16.4	50 x 50
Module array size	5 x 14 (transaxial x axial)	3 x 3 (transaxial x axial)	9 x 13 (transaxial x axial)	4 x 2 (transaxial x axial)	1 x 1 (transaxial x axial)
Module pitch (mm x mm)	102 x 244	79 x 79	174 x 252	65.7 x 32.9	50 x 52

Number of modules (per ring x # rings)	16 x 2	20 x 6	8 x 1	38 x 8	16 x 3
TOF resolution (ps)	430	< 250	N/A	214	N/A
DOI bin size (mm)	N/A	4.5	10	N/A	1
Time window (ns)	2.7 – 2.9	2.9	6	4.1	5
Energy window (keV)	430 – 1000	430 – 650	400 – 650	435 – 650	355 – 664
Energy resolution (%)	11.7	11.7	11.7	11.7	17
Crystal material	LYSO	LYSO	LSO+LYSO	LSO	LYSO

*F2F: crystal face-to-face (i.e. the distance between the crystals from opposing detectors)

Digitizer parameters

In a Monte Carlo simulation, the digitizer setup can significantly alter the results by 30% or more. Care must be taken to ensure that the digitizer and readout parameters model the front-end electronics of the real-life scanners as closely as possible. For each scanner simulated in GATE, we used a digitizer level of 2 or 3 (i.e. the module or sub-module levels), whichever one is equivalent to the block detector level for the particular scanner.

To minimize sensitivity differences caused by coincidence policies, the coincidence processors for all simulated scanners were configured to be multiple window (MW), *takeAllGoods*. Also, true coincidence events that were outside the time window or outside the maximum acceptance angle (in the form of maximum ring difference) for each scanner were excluded. In addition, coincidence events that intersect the NX shoulder cutouts were excluded after the simulation. For this sensitivity study, dead-time was not modeled in the scanners and are not expected to significantly affect the results due to the low radioactivity level simulated in the study.

Sensitivity

To predict the sensitivity of each scanner, we performed simulations involving point sources, line sources, and anthropomorphic digital phantoms. Parametrized simulations were performed with the point

and line sources to reduce computational time, while voxelized simulations were performed with the anthropomorphic phantom.

Line source sensitivity

We assessed the line source sensitivity of each scanner based on the NEMA NU 2-2018 sensitivity protocol. Simulations involving a 700 mm line source enclosed in 1 – 5 aluminum sleeves of equal length were performed to mimic the real-life experimental procedure. The source was 1 MBq ^{18}F (with 0 mm radial offset), and the simulation time for each simulation was 60 s. The results were normalized to the axial slice thickness to allow for comparison between scanners.

Point source sensitivity

We also assessed the point source sensitivity of each scanner using a point source enclosed in a 10 x 10 x 10 mm³ plexiglass cube, similar to the NEMA NU 4-2008 sensitivity protocol. Plexiglass was selected in lieu of acrylic since it was not available as a material in GATE. The source was 1 MBq ^{18}F (with 0 mm radial offset), and the simulation time for each simulation was 60 s. The point source was moved along the scanner axis in 25 – 50 mm steps. The sensitivity of each scanner is defined by $S_z(\%) =$

$$\frac{n_{trues}}{n_{primaries}} \times 100\%$$

(Equation 5-1:

$$S_z(\%) = \frac{n_{trues}}{n_{primaries}} \times 100\% \quad \text{(Equation 5-1)}$$

where S_z is the sensitivity of the scanner (in %), z is the axial position of the center of the source (in mm), n_{trues} is the number of true coincidences detected by the scanner, and $n_{primaries}$ is the number of radioactive decays (i.e. annihilation events) in the simulation.

Uniform brain sensitivity

To predict the brain sensitivity of each scanner, we performed simulations involving a 4D extended cardiac-torso (XCAT) anthropomorphic phantom ([Segars 2010](#)). The XCAT software platform includes digital phantoms that contain detailed, whole-body anatomies and models for cardiac and respiratory motions derived from human imaging datasets. The XCAT phantom we used for the simulation

was the standard, vmale50 phantom. The voxel size was 3.125 x 3.125 x 3.125 mm (256 x 256 x 600 voxels) and trimmed down to ensure the image did not intersect the scanner geometry (which prevents the detection of events in overlapped areas).

For a voxelized simulation in GATE, a material map and an activity map are defined. For the material map, we condensed 112 materials in the XCAT phantom into 19 default GATE materials. To assess the sensitivity of the brain, we distributed 1 MBq ¹⁸F-FDG uniformly in the brain voxels and did not assign any activity values in the rest of the body for the activity map. The simulation time was 10 s. We then moved the XCAT phantom (using the centroid of the brain voxels as the origin) along the scanner axis in 25 – 50 mm steps to obtain the sensitivity at different positions. Similar to the point source

simulations, we used $S_z(\%) = \frac{n_{trues}}{n_{primaries}} \times 100\%$ (Equation 5-1 to assess the

brain sensitivity. Figure 5-3 shows a representation of the uniform brain simulation setup.

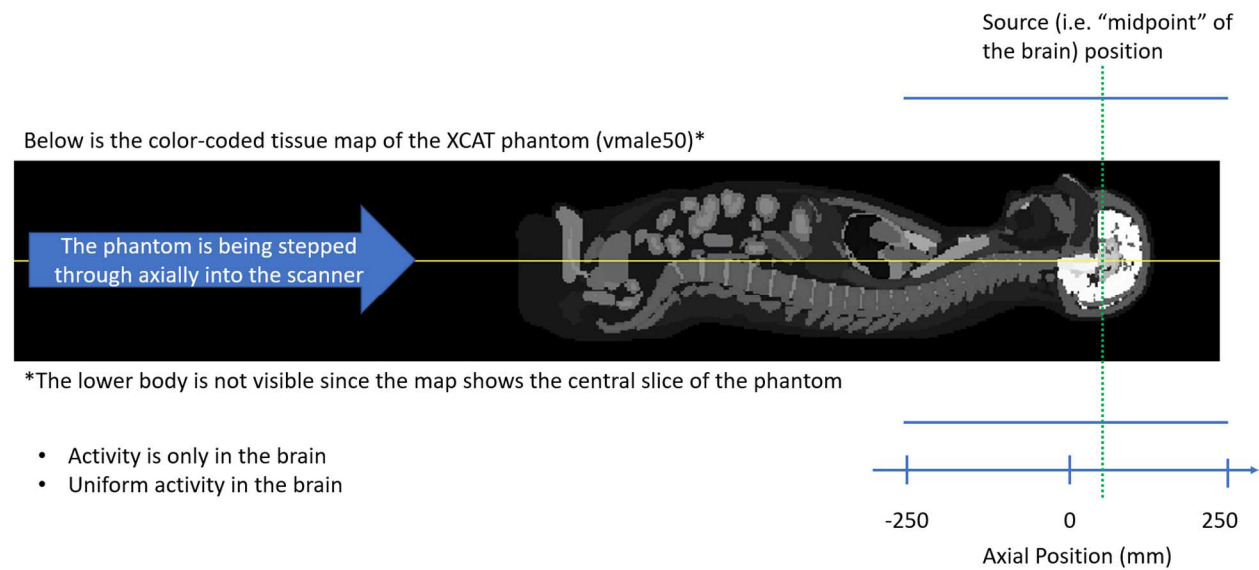


Figure 5-3. A representation of the uniform brain simulation setup.

Results

Line source sensitivity

The line source sensitivity of each scanner, plotted as a function of slice position, is shown in Figure 5-4. The peak sensitivities of the NX (with shoulder cutout), HRRT, Biograph Vision, and CareMiBrain scanners were 0.21, 0.09, 0.14, and 0.11 cps/kBq/mm, respectively. The NX peak sensitivity

results (with shoulder cutout and with 25 mm long crystals) was a factor of 1.4 higher than with the shorter, 18.1 mm long crystals, at 0.29 cps/kBq/mm. The peak sensitivity of the Mini EXPLORER II simulation results was 7.7% higher than the experimental results.

The flattened sensitivity region (in contrast to the triangular shape in other results) in the HRRT results is caused by the limited maximum acceptance angle, in the form of maximum axial crystal ring difference.

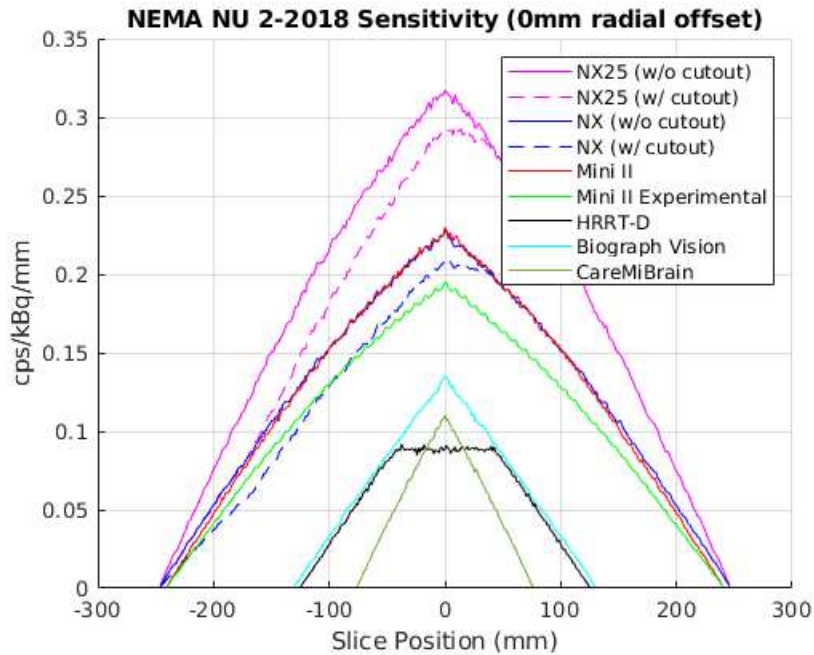


Figure 5-4. NEMA NU 2-2018 sensitivity of various scanners.

Point source sensitivity

The point source sensitivity of each scanner, plotted as a function of source axial position, is shown in Figure 5-5. The peak sensitivities of the NX (with shoulder cutout), HRRT, Biograph Vision, and CareMiBrain scanners were 14.1%, 5.9%, 8.8%, and 7.2%, respectively. The NX peak sensitivity results (with shoulder cutout and with 25 mm long crystals) was a factor of 1.4 higher than with the shorter, 18.1 mm long crystals, at 19.6%.

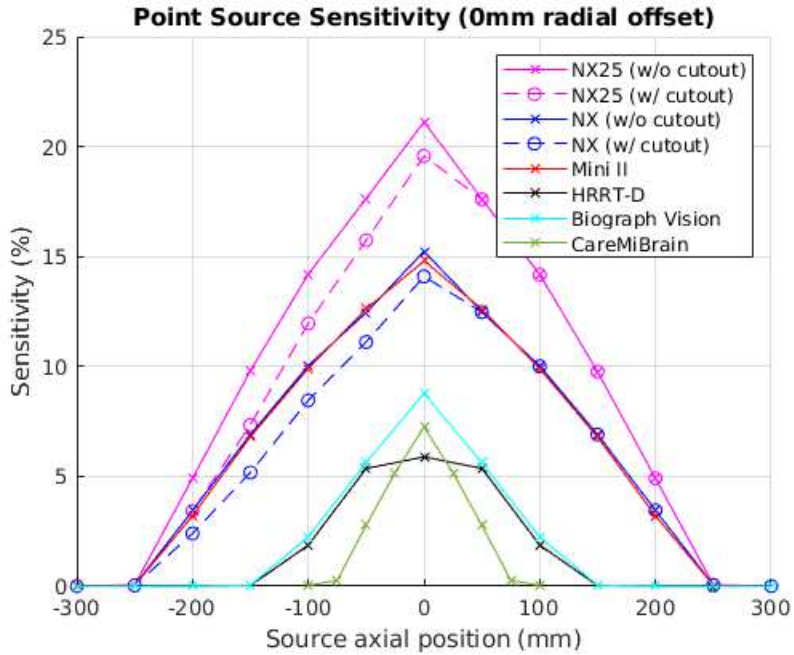


Figure 5-5. Point source sensitivity of various scanners.

Uniform brain sensitivity

The uniform brain sensitivity of each scanner, plotted as a function of source axial position, is shown in Figure 5-6. The peak sensitivities of the NX (with shoulder cutout), HRRT, Biograph Vision, and CareMiBrain scanners were 3.4%, 1.6%, 1.8%, and 2.1%, respectively. The NX peak sensitivity results (with shoulder cutout and with 25 mm long crystals) was a factor of 1.4 higher than with the shorter, 18.1 mm long crystals, at 4.8%.

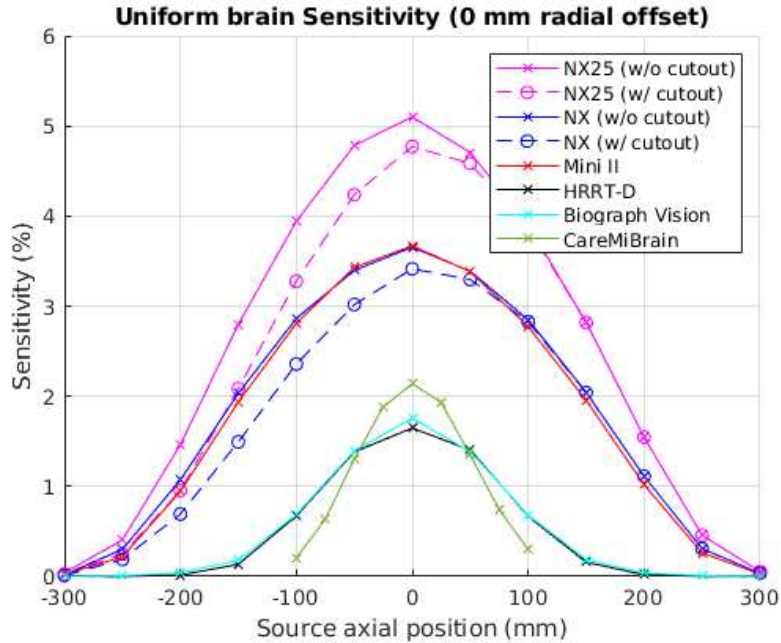


Figure 5-6. Uniform brain sensitivity of various scanners.

Discussion

The results above showed that the sensitivity of the NX scanner (without shoulder cutout) is similar to the Mini EXPLORER II scanner as expected, since the 2 PET ring geometries are similar. The spatial resolution of the NX scanner is expected to be improved, however, due to the smaller crystals and DOI-encoded detectors.

And as expected, the increase in solid angle coverage of the NX scanner over both the HRRT-D and Biograph Vision scanners lead to approximately a 2-fold increase in peak sensitivity, as well as an approximate 5-fold increase in total sensitivity. We note that the additional sensitivity gain due to TOF is expected to be ~4-fold greater than the HRRT-D scanner (Carson 2021) and are not reflected in this sensitivity assessment.

While the shoulder cutouts of the NX scanner led to a sensitivity drop on the feet side of the sensitivity profile, the benefit of being able to center the brain in the scanner for maximum brain sensitivity outweighs this small asymmetric sensitivity loss. Compared to a shorter scanner that does not image the carotid arteries, or the use of a larger ring diameter of the same axial coverage, at the expense of

increased of scanner cost and reduced sensitivity (due to the reduction of solid angle coverage), the NX cutout design optimizes sensitivity and axial coverage.

While the large increase in sensitivity using 25 mm long crystals appeared to be an attractive option, the increase in scintillator materials is a cost disadvantage. In addition, the longer crystals may degrade TOF resolution, which can reduce the effective sensitivity of the scanner due to TOF.

Conclusion

We have developed a Monte Carlo simulation framework for the NX dedicated brain PET scanner. With photon flux rate modeling for dead-time estimation completed (Li 2021), future work includes simulations for various brain PET applications. The simulation data may also be used for assessing the image quality and quantitative accuracy of images produced by the image reconstruction platform dedicated for the NX scanner (currently under development within the Yale-UC Davis partnership).

Chapter 6 – Conclusion and future work

Summary and next steps

The bulk of this work was centered upon the need to establish the quantitative accuracy baseline and computational foundation for total-body PET and its derivatives. In Chapter 2, we performed the first comprehensive, quantitative evaluation of the EXPLORER scanner, and discovered that the absolute quantitative accuracy of a total-body PET scanner can be sensitive to the exact implementations of the scanner calibration and PET data corrections (including LUTs and image inputs), as well as the image reconstruction parameters. We suggested that for clinical and research imaging studies and with static image reconstruction and longer frame duration (i.e. > 30 s), the quantification bias is expected to be within $\pm 5\%$ for both high and low injected radiotracer doses in the EXPLORER scanner.

While the quantitative performance achieved with the EXPLORER scanner has been shown to be uniform across the axial FOV and provides the accuracy necessary to support a broad range of imaging applications spanning from low-dose studies to dynamic imaging with commonly used frame lengths, there is motivation to further improve the quantitative accuracy and stability in total-body PET to maximize the benefits arose from the scanner sensitivity gain and the extended axial FOV. Larger bias changes during the bolus injection phase in humans remain a challenge in achieving accurate PET data corrections for complex activity distribution across a very large dynamic range. To fully understand the origins of all types of biases, an independent image reconstruction platform is indispensable for investigative purposes, and additional comprehensive, and quantitative assessments are essential to better characterize the biases seen thus far. These suggestions, however, massively increase the workload as well as the computational burden, but cannot be avoided if a complete characterization of each quantitative bias is required. Careful design of a computational and reconstruction infrastructure and standardization of test protocols can minimize this obstacle.

In the immediate future, some of the quantitative biases can be assessed using the reconstruction platform provided by the scanner manufacturer. For instance, to assess the quantitative effects due to the number of counts (e.g. in short frame durations or low activity imaging), a varying number of OSEM iterations, subsets (down to 1), and reconstruction voxel sizes may be used. With a more quantitatively accurate total-body PET scanner, we can better support new and existing imaging

opportunities that arose from the increase in scanner sensitivity and longer axial FOV, including more accurate extraction of PET kinetic modeling parameters across the entire human for system modeling, lesion characterization, and measuring tumor response to therapy.

In Chapter 3, we developed a Monte Carlo scatter correction implementation for total-body PET that utilizes continuous water density materials as the attenuation input. Scatter correction in total-body PET is the most difficult PET data correction of all since scattered coincidence events cannot be directly measured, and that the contribution of higher-order scattered coincidences is higher than that in conventional PET scanners due to the increased axial acceptance angle. This work has shown that the use of continuous water density materials as a surrogate for threshold-based material segmentation may be sufficiently accurate and may be used as the benchmark for future scatter correction implementations. In addition to the simulation results using the XCAT phantom, the experimental results shown in the projection domain of the 3 x 3 grid phantom surrounded with and without wax has shown promise of the continuous water density implementation.

At the same time, the need to perform scatter fitting on a per-sinogram basis (as compared to a global scaling based on total counts) suggests that further refinement of the scanner model may be beneficial. To further increase the accuracy of the scatter correction, a detailed model of the scanner electronics is required, similar to the work previously done for the Biograph mCT scanner ([Poon 2015](#)). Also, large metal implants (e.g. in shoulder and hip replacements) in the human can significantly affect the accuracy of the scatter correction due to the presence of metal artifacts in the CT image, and that a high-density water material is inappropriate to serve as a replacement for metals in the material map due to the significant difference in the effective atomic numbers, which affects the attenuation and scattering properties. Reducing the metal artifact in the CT image volume prior to converting into the material map, in addition to assigning the proper materials for orthopedic implants (e.g. titanium and steel) to the appropriate voxel locations in the material map, may further improve the accuracy of the scatter correction.

One of the greatest limitations of Monte Carlo scatter correction is its poor computational performance. Since Monte Carlo scatter correction comprises the bulk of the computational time during image reconstruction, a hardware-accelerated scatter correction implementation using GPUs and cloud

computing can alleviate the computational bottleneck. Another way to reduce the computational time is to vary the number of simulated events to achieve an optimal balance between computational performance and noise level of the scatter correction data.

In Chapter 4, we investigated the relationship between ^{18}F -FDG image SNR and NECR in total-body PET using the EXPLORER scanner. We derived the non-TOF NECR and TOF-NECR expressions for list-mode PET data and assessed the SNR of TOF-reconstructed images in both a long cylindrical water phantom and in human subjects. Our phantom NECR results showed that increasing the activity level past the activity concentration at peak non-TOF NECR may continue to improve TOF-reconstructed image SNR, since the TOF-NECR at that activity concentration continued to increase at a greater rate, suggesting that the activity concentration at peak TOF-NECR is higher than that from non-TOF NECR. In the future, performing a decay series of experiments by scanning the uniform phantom beginning at an activity level past the activity concentration at both the peak non-TOF NECR and TOF-NECR may provide more insight. The improved linear fit R^2 values for SNR^2 vs TOF-NECR over non-TOF NECR in the uniform phantom also suggested that TOF-NECR may be more appropriate, in some circumstances, for directly estimating the SNR of TOF-reconstructed images.

In human subjects, the difference in linear fit R^2 values for SNR^2 vs TOF-NECR and non-TOF NECR was statistically insignificant ($p = 0.3273$ from the paired t-test). Some of the challenges when relating the image SNR^2 to NECR in humans is that the image SNR in the liver is sensitive to motion artifacts, and that the activity redistribution (particularly in the liver) over 12 h may reduce the quality of the linear fitting. The use of radiotracers that are more stable in the liver and across the body over longer durations, such as ^{68}Ga -NEB and ^{18}F -HSA which binds to serum albumin ([Chang 2005](#), [Niu 2014](#), [Zhang 2015](#)), may further strengthen the robustness of the linear fitting. Again, the non-linear behavior was only noticeable in the uniform phantom as the activity level approached the activity concentration at peak non-TOF NECR. The non-TOF NECR in the humans continued to increase at the highest activity concentration observed. Increasing the injected dose (if permitted) past the peak NECR at scan time may help in revealing the non-linear behavior in image SNR^2 vs non-TOF NECR in humans. Alternatively, techniques such as modeling the patient-specific NECR ([Watson 2005](#)) across the entire body and/or via simulations may help provide more wisdom as well.

One of the greatest challenges when designing an optimal dosing protocol for consistent SNR across human subjects for a specific PET system is that the patient habitus may significantly affect both the NECR and image SNR, as well as the slope of the image SNR² vs NECR plot. Additional human studies are essential to improve the statistical power of the datasets for a more detailed analysis.

In Chapter 5, we developed a high-performance, software-based coincidence processing method to handle the massive singles data produced by the EXPLORER scanner. This work has demonstrated the feasibility of performing near real-time coincidence processing for long axial FOV scanners using several computational nodes. Since the performance bottleneck of the coincidence processor was found to be I/O-related, the use of faster solid-state storage devices can quickly reduce the number of computation nodes required. For instance, multiple solid-state drives can be combined into a RAID 0 array that outperforms the single PCIe 3.0 NVMe SSD that was used for the assessment. Alternatively, a faster PCIe 4.0 NVMe SSD may be used instead. The benefits of acquiring list-mode single events over coincidence events is under assessment as research interests begin to rise in this area, although it is expected that a hardware-based coincidence processor will continue to be the standard for clinical PET systems.

In Chapter 6, we developed a simulation framework for the NeuroEXPLORER (NX) scanner, the next-generation dedicated brain PET scanner since the introduction of the HRRT scanner. This work has shown that the increase in solid angle coverage of the NX scanner over both the HRRT-D and Biograph Vision scanners can lead to approximately a 2-fold increase in peak sensitivity, as well as an approximate 5-fold increase in total sensitivity. This work contributed to the NIH U01 funding approval of the NX scanner, and the simulation framework is being used by multiple researchers for additional NX simulation studies to approximate the real-life performance of the scanner in various applications.

Overall, the work described in this dissertation took a first dive into tackling new challenges in total-body PET that were not investigated in detail previously. While conceptually simple, the broad scope of this work was massive as it involved the development of several framework and infrastructure in addition to experimental validations.

The practical future of total-body PET

Prior to the introduction of the first commercial total-body PET system, it has been suggested that extending the axial FOV of a PET scanner enables improved trade-offs between 1) scan time, 2) radiation dose, and 3) image quality ([Cherry 2018](#)). Results from recent work ([Badawi 2019](#)) has demonstrated these benefits, hinting the feasibility of utilizing such devices in the clinical environment. However, total-body PET scanners have yet to be widely adopted today, as the long-term feasibility of total-body PET remains unknown, particularly in both the North American and European countries, which prevents their true potential to be realized in areas where a total-body PET scanner would be invaluable, such as in multi-center clinical trials and in pandemic situations where many scans need to be performed in a short amount of time.

A major barrier that prevents total-body PET systems to become mainstream in the clinical environment is its cost. Since the EXPLORER scanner is comprised of 8 PET scanner units, it costs approximately 8 times more compared to a conventional PET scanner using similar hardware. To reduce scanner costs today, more affordable scintillators (such as BGO) may be used in place of the more expensive ^{176}Lu -based scintillators, such as LYSO, at the expense of degraded TOF performance. However, taking advantage of event timing based on the Cherenkov effect may make BGO a suitable candidate for TOF-PET ([Brunner 2017](#)). In applications where the imaging of the entire body simultaneously is favored over TOF capability, such as in total-body dynamic imaging, the trade-off may be acceptable. Future work is needed to assess both the on-paper and real-world performance tradeoffs between solid angle coverage and TOF-capability between BGO and ^{176}Lu -based total-body PET scanners, and particularly ^{176}Lu -based conventional PET scanners that comprises many new clinical PET scanners sold today.

Aside from scanner cost, another reason that total-body PET has not immediately led to a paradigm shift in the daily clinical workflow is that its clinical utility has yet to be proven at scale. Although early studies have shown that images from reduced scan time (< 30 s) using total-body PET scanners were comparable to the ones from conventional PET scanners ([Badawi 2019](#)), current clinical imaging protocols for total-body PET (296 MBq injected dose, imaging at 2-h post-injection) is focused on improving image quality, rather than scanning more human subjects. As a result, patient throughput

remains limited, which increases the time required to demonstrate clinical usefulness of total-body PET. It may be worthwhile to transition the clinical focus from improving image quality to increasing patient throughput. This way, total-body PET can have a broader impact on the general clinical population more swiftly, which may help grow the number of total-body PET scanners in North American and European countries, ultimately enabling the assessment on the global impact of patient care in under-investigated areas such as improved PET image quality or reduced injected radiation dose.

Today, prostate cancer imaging using ^{18}F -fluciclovine is one of the areas that may receive immediate benefits from total-body PET. Current clinical guidelines for prostate cancer PET imaging using ^{18}F -fluciclovine ([Nanni 2020](#)) recommended that imaging begins at 3 – 5 min post-injection. However, early data in ^{18}F -fluciclovine total-body PET studies suggested that patient habitus can influence the tumor uptake time outside of the expected range. With conventional PET scanners, a sub-optimal combination of uptake time, scan protocol and bed position may potentially lead to false negatives. Further work is needed to demonstrate the clinical impacts of utilizing total-body PET in such scenarios.

One of the often underdiscussed topic in total-body PET is the unintended consequences from [information overload](#). As the amount of information obtained from a human subject becomes greater, it also becomes more challenging to interpret the massive amount of data. For instance, it remains unclear how system-level kinetic modeling may impact patient care in the long run. Conventional data analysis methods may prove inadequate for total-body PET data given the massive amount of information it provides. The rapid and massive gain in popularity in data science and radiomics in recent years has the potential to help us navigate in a sea of total-body PET data.

Most importantly, with the significant data size increase in total-body PET over conventional PET, the massive computational burden associated must be addressed. Standardization and streamlining of total-body PET data processing and reconstruction by utilizing a robust – while flexible – high-performance computational infrastructure (e.g. hardware-accelerated cloud computing, or a distributed computing) is essential.

The emergence of total-body PET as an imaging tool has opened many new opportunities and applications and has the potential to drive PET research into a new era. It is prudent to remember that these opportunities can only be actualized with massive supporting infrastructure to maximize the impact

of total-body PET research. The long-term potential of total-body PET is likely to heavily depend on the handling of logistical challenges, such as clinical workflow and computational load. Extreme forethought and pre-planning are vital to ensure its future success.

References

- Atav Ü, Tomak M and ŞAHİN M 2006 Applications of genetic algorithm to quantum mechanical systems *Turkish journal of physics* **30** 253-75
- Bach-Gansmo T, Nanni C, Nieh P T, Zanoni L, Bogsrud T V, Sletten H, Korsan K A, Kieboom J, Tade F I, Odewole O, Chau A, Ward P, Goodman M M, Fanti S, Schuster D M and Willoch F 2017 Multisite Experience of the Safety, Detection Rate and Diagnostic Performance of Fluciclovine (18 F) Positron Emission Tomography/Computerized Tomography Imaging in the Staging of Biochemically Recurrent Prostate Cancer *The Journal of urology* **197** 676-83
- Badawi R D 1998 *Aspects of Optimisation and Quantification in Three Dimensional Positron Emission Tomography* (London: University of London)
- Badawi R D and Marsden P K 1999 Developments in component-based normalization for 3D PET *Physics in medicine & biology* **44** 571-94
- Badawi R D, Shi H, Hu P, Chen S, Xu T, Price P M, Ding Y, Spencer B A, Nardo L, Liu W, Bao J, Jones T, Li H and Cherry S R 2019 First Human Imaging Studies with the EXPLORER Total-Body PET Scanner *The Journal of nuclear medicine (1978)* **60** 299-303
- Bailey D L 2005 *Positron emission tomography : basic sciences* (New York: Springer)
- Bailey D L and Meikle S R 1994 A convolution-subtraction scatter correction method for 3D PET *Physics in medicine & biology* **39** 411-24
- Bendriem B, Trebossen R, Frouin V and Syrota A 1993 A PET scatter correction using simultaneous acquisitions with low and high lower energy thresholds. IEEE) pp 1779-83 vol.3
- Berg E, Gill H, Marik J, Ogasawara A, Williams S, van Dongen G, Vugts D, Cherry S R and Tarantal A F 2020 Total-Body PET and Highly Stable Chelators Together Enable Meaningful 89Zr-Antibody PET Studies up to 30 Days After Injection *The Journal of nuclear medicine (1978)* **61** 453-60
- Berg E, Zhang X, Bec J, Judenhofer M S, Patel B, Peng Q, Kapusta M, Schmand M, Casey M E, Tarantal A F, Qi J, Badawi R D and Cherry S R 2018 Development and Evaluation of mini-EXPLORER: A Long Axial Field-of-View PET Scanner for Nonhuman Primate Imaging *The Journal of nuclear medicine (1978)* **59** 993-8
- Bettinardi V, Danna M, Savi A, Lecchi M, Castiglioni I, Gilardi M C, Bammer H, Lucignani G and Fazio F 2004 Performance evaluation of the new whole-body PET/CT scanner: Discovery ST *European journal of nuclear medicine and molecular imaging* **31** 867-81
- Bettinardi V, Presotto L, Rapisarda E, Picchio M, Gianolli L and Gilardi M C 2011 Physical Performance of the new hybrid PET/CT Discovery-690 *Medical physics (Lancaster)* **38** 5394-411
- Boellaard R 2009 Standards for PET Image Acquisition and Quantitative Data Analysis *The Journal of nuclear medicine (1978)* **50** 11S-20S
- Boland G W L, Blake M A, Holalkere N S and Hahn P F 2009 PET/CT for the Characterization of Adrenal Masses in Patients with Cancer: Qualitative Versus Quantitative Accuracy in 150 Consecutive Patients *American journal of roentgenology (1976)* **192** 956-62

- Brasse D, Kinahan P E, Lartzien C, Comtat C, Casey M and Michel C 2005 Correction Methods for Random Coincidences in Fully 3D Whole-Body PET: Impact on Data and Image Quality *The Journal of nuclear medicine (1978)* **46** 859-67
- Brownell G L, Correia J A and Zamenhof R G 1979 "Positron Instrumentation" in *Recent Advances in Nuclear Medicine* (New York: Grune & Stratton)
- Brun R and Rademakers F 1997 ROOT — An object oriented data analysis framework *Nuclear instruments & methods in physics research. Section A, Accelerators, spectrometers, detectors and associated equipment* **389** 81-6
- Brunner S E and Schaart D R 2017 BGO as a hybrid scintillator / Cherenkov radiator for cost-effective time-of-flight PET *Physics in medicine & biology* **62** 4421-39
- Budinger T F 1983 Time-of-Flight Positron Emission Tomography: Status Relative to Conventional PET *The Journal of nuclear medicine (1978)* **24** 73-8
- Carlier T, Ferrer L, Necib H, Bodet-Milin C, Rousseau C and Kraeber-Bodéré F 2014 Clinical NECR in 18F-FDG PET scans: optimization of injected activity and variable acquisition time. Relationship with SNR *Physics in medicine & biology* **59** 6417-30
- Carney J P J, Townsend D W, Rappoport V and Bendriem B 2006 Method for transforming CT images for attenuation correction in PET/CT imaging *Medical physics (Lancaster)* **33** 976-83
- Casey M E and Nutt R 1986 A Multicrystal Two Dimensional BGO Detector System for Positron Emission Tomography *IEEE transactions on nuclear science* **33** 460-3
- Chang T, Chang G, Kohlmyer S, Clark J W, Rohren E and Mawlawi O R 2011 Effects of injected dose, BMI and scanner type on NECR and image noise in PET imaging *Physics in medicine & biology* **56** 5275-85
- Chang Y S, Jeong J M, Lee Y-S, Kim H W, Rai G B, Lee S J, Lee D S, Chung J-K and Lee M C 2005 Preparation of 18F-Human Serum Albumin: A Simple and Efficient Protein Labeling Method with 18F Using a Hydrazone-Formation Method *Bioconjugate chemistry* **16** 1329-33
- Cherry S R, Jones T, Karp J S, Qi J, Moses W W and Badawi R D 2018 Total-Body PET: Maximizing Sensitivity to Create New Opportunities for Clinical Research and Patient Care *The Journal of nuclear medicine (1978)* **59** 3-12
- Cherry S R, Sorenson J A and Phelps M E 2012 *Physics in nuclear medicine* (Philadelphia: Elsevier/Saunders)
- Cherry S R and Sung-Cheng H 1995 Effects of scatter on model parameter estimates in 3D PET studies of the human brain *IEEE transactions on nuclear science* **42** 1174-9
- Conti M 2006 Effect of randoms on signal-to-noise ratio in TOF PET *IEEE transactions on nuclear science* **53** 1188-93
- Conti M, Eriksson L, Rothfuss H, Sjoeholm T, Townsend D, Rosenqvist G and Carlier T 2017 Characterization of 176Lu background in LSO-based PET scanners *Physics in medicine & biology* **62** 3700-11

- Dahlbom M, Schiepers C and Czernin J 2005 Comparison of noise equivalent count rates and image noise *IEEE transactions on nuclear science* **52** 1386-90
- Danna M, Lecchi M, Bettinardi V, Gilardi M, Stearns C, Lucignani G and Fazio F 2006 Generation of the Acquisition-Specific NEC (AS-NEC) Curves to Optimize the Injected Dose in 3D ¹⁸F-FDG Whole Body PET Studies *IEEE transactions on nuclear science* **53** 86-92
- Daube-Witherspoon M E and Muehllehner G 1987 Treatment of Axial Data in Three-Dimensional PET *The Journal of nuclear medicine (1978)* **28** 1717-24
- de Jong H W A M, Knoess C, Lammertsma A A, Lenox M, Vollmar S, Casey M, Wienhard K, Heiss W D and Boellaard R 2004 Performance characteristics of the high resolution research tomograph comparison of three prototypes. *IEEE) pp 3437-9 Vol. 6*
- de Jong H W A M, van Velden F H P, Kloet R W, Buijs F L, Boellaard R and Lammertsma A A 2007 Performance evaluation of the ECAT HRRT: an LSO-LYSO double layer high resolution, high sensitivity scanner *Physics in medicine & biology* **52** 1505-26
- Defrise M, Kinahan P E, Townsend D W, Michel C, Sibomana M and Newport D F 1997 Exact and approximate rebinning algorithms for 3-D PET data *IEEE transactions on medical imaging* **16** 145-58
- El Fakhri G, Kardan A, Sitek A, Dorbala S, Abi-Hatem N, Lahoud Y, Fischman A, Coughlan M, Yasuda T and Di Carli M F 2009 Reproducibility and Accuracy of Quantitative Myocardial Blood Flow Assessment with ⁸²Rb PET: Comparison with ¹³N-Ammonia PET *The Journal of nuclear medicine (1978)* **50** 1062-71
- Fahey F H 2002 Data Acquisition in PET Imaging *The Journal of nuclear medicine (1978)* **30** 39-49
- Feng T, Zhao Y, Shi H, Li H, Zhang X, Wang G, Price P M, Badawi R D, Cherry S R and Jones T 2021 Total-Body Quantitative Parametric Imaging of Early Kinetics of ¹⁸F-FDG *Journal of Nuclear Medicine* **62** 738-44
- Frach T, Prescher G, Degenhardt C, de Gruyter R, Schmitz A and Ballizany R 2009 The digital silicon photomultiplier - Principle of operation and intrinsic detector performance. *IEEE) pp 1959-65*
- Goldschmidt B, Lerche C W, Solf T, Salomon A, Kiessling F and Schulz V 2013 Towards Software-Based Real-Time Singles and Coincidence Processing of Digital PET Detector Raw Data *IEEE transactions on nuclear science* **60** 1550-9
- Grootoink S, Spinks T J, Sashin D, Spyrou N M and Jones T 1996 Correction for scatter in 3D brain PET using a dual energy window method *Physics in medicine & biology* **41** 2757-74
- Hoffman E J, Guerrero T M, Germano G, Digby W M and Dahlbom M 1989 PET system calibrations and corrections for quantitative and spatially accurate images *IEEE transactions on nuclear science* **36** 1108-12
- Holdsworth C H, Levin C S, Janecek M, Dahlbom M and Hoffman E J 2002 Performance analysis of an improved 3-D PET Monte Carlo simulation and scatter correction *IEEE transactions on nuclear science* **49** 83-9
- Huang S-C 1999 Image oscillation reduction and convergence acceleration for OS-EM reconstruction [PET imaging] *IEEE transactions on nuclear science* **46** 603-7

Hudson H M and Larkin R S 1994 Accelerated image reconstruction using ordered subsets of projection data *IEEE transactions on medical imaging* **13** 601-9

Jakoby B W, Bercier Y, Conti M, Casey M E, Bendriem B and Townsend D W 2011 Physical and clinical performance of the mCT time-of-flight PET/CT scanner *Physics in medicine & biology* **56** 2375-89

Jan S, Santin G, Strul D, Staelens S, Assié K, Autret D, Avner S, Barbier R, Bardiès M, Bloomfield P M, Brasse D, Breton V, Bruyndonckx P, Buvat I, Chatziioannou A F, Choi Y, Chung Y H, Comtat C, Donnarieix D, Ferrer L, Glick S J, Groiselle C J, Guez D, Honore P F, Kerhoas-Cavata S, Kirov A S, Kohli V, Koole M, Krieguer M, Laan D J v d, Lamare F, Largeron G, Lartizien C, Lazaro D, Maas M C, Maigne L, Mayet F, Melot F, Merheb C, Pennacchio E, Perez J, Pietrzyk U, Rannou F R, Rey M, Schaart D R, Schmidlein C R, Simon L, Song T Y, Vieira J M, Visvikis D, Walle R V d, Wieërs E and Morel C 2004 GATE: a simulation toolkit for PET and SPECT *Physics in medicine & biology* **49** 4543-61

Jian Y, Planeta B and Carson R E 2014 Evaluation of bias and variance in low-count OSEM list mode reconstruction *Physics in medicine & biology* **60** 15-29

Johansson J, Oikonen V and Teras M 2007 Quantitative brain imaging using the new, fast iterative histogram-mode reconstruction for the HRRT PET scanner. *IEEE* pp 3463-7

Judenhofer M S 2018 EXPLORER Singles Processing Framework (v1.0) *Unpublished*

Karakatsanis N A, Lodge M A, Tahari A K, Zhou Y, Wahl R L and Rahmim A 2013 Dynamic whole-body PET parametric imaging: I. Concept, acquisition protocol optimization and clinical application *Physics in medicine & biology* **58** 7391-418

Kemp B J, Kim C, Williams J J, Ganin A and Lowe V J 2006 NEMA NU 2-2001 Performance Measurements of an LYSO-Based PET/CT System in 2D and 3D Acquisition Modes *The Journal of nuclear medicine (1978)* **47** 1960-7

Knoll G F 2010 *Radiation detection and measurement* (New York: Wiley)

Lai Y, Zhong Y, Chalise A, Shao Y, Jin M, Jia X and Chi Y 2019 gPET: a GPU-based, accurate and efficient Monte Carlo simulation tool for PET *Physics in medicine & biology* **64** 245002-

Lartizien C, Comtat C, Kinahan P E, Ferreira N, Bendriem B and Trebossen R 2002 Optimization of Injected Dose Based on Noise Equivalent Count Rates for 2- and 3-Dimensional Whole-Body PET *The Journal of nuclear medicine (1978)* **43** 1268-78

Leo W R 1994 *Techniques for nuclear and particle physics experiments : a how-to approach* (Berlin: Springer)

Lercher M J and Wienhard K 1994 Scatter correction in 3-D PET *IEEE transactions on medical imaging* **13** 649-57

Leung E, Revilla E, Spencer B, Xie Z, Zhang X, Omidvari N, Badawi R, Cherry S, Lu Y and Berg E 2021a A quantitative image reconstruction platform with integrated motion detection for total-body PET. *Soc Nuclear Med*)

Leung E K, Berg E, Omidvari N, Spencer B A, Li E, Abdelhafez Y G, Schmall J P, Liu W, He L, Tang S, Liu Y, Dong Y, Jones T, Cherry S R and Badawi R D 2021b Quantitative accuracy in total-body imaging using the uEXPLORER PET/CT scanner *Physics in medicine & biology* **66**

- Levin C S, Dahlbom M and Hoffman E J 1995 A Monte Carlo correction for the effect of Compton scattering in 3-D PET brain imaging *IEEE transactions on nuclear science* **42** 1181-5
- Lewitt R M, Muehllehner G and Karp J S 1994 Three-dimensional image reconstruction for PET by multi-slice rebinning and axial image filtering *Physics in medicine & biology* **39** 321-39
- Lingxiong S, Freifelder R and Karp J S 1994 Triple energy window scatter correction technique in PET *IEEE transactions on medical imaging* **13** 641-8
- Liu G, Hu P, Yu H, Tan H, Zhang Y, Yin H, Hu Y, Gu J and Shi H 2021 Ultra-low-activity total-body dynamic PET imaging allows equal performance to full-activity PET imaging for investigating kinetic metrics of 18 F-FDG in healthy volunteers *European Journal of Nuclear Medicine and Molecular Imaging* 1-11
- Lockhart C M, MacDonald L R, Alessio A M, McDougald W A, Doot R K and Kinahan P E 2011 Quantifying and reducing the effect of calibration error on variability of PET/CT standardized uptake value measurements *The Journal of nuclear medicine (1978)* **52** 218-24
- Lodge M A, Lesniak W, Gorin M A, Pienta K J, Rowe S P and Pomper M G 2021 Measurement of PET Quantitative Bias In Vivo *The Journal of nuclear medicine (1978)* **62** 732-7
- Lv Y, Lv X, Liu W, Judenhofer M S, Zwingenberger A, Wisner E, Berg E, McKenney S, Leung E, Spencer B A, Cherry S R and Badawi R D 2019 Mini EXPLORER II: a prototype high-sensitivity PET/CT scanner for companion animal whole body and human brain scanning *Physics in medicine & biology* **64** 075004-
- McElroy D P, Hoose M, Pimpl W, Spanoudaki V, Schüler T and Ziegler S I 2005 A true singles list-mode data acquisition system for a small animal PET scanner with independent crystal readout *Physics in medicine & biology* **50** 3323-35
- McKee B T A, Gurvey A T, Harvey P J and Howse D C 1992 A deconvolution scatter correction for a 3-D PET system *IEEE transactions on medical imaging* **11** 560-9
- Melcher C L 2000 Scintillation Crystals for PET *The Journal of nuclear medicine (1978)* **41** 1051-5
- Miller M, Zhang J, Binzel K, Griesmer J, Laurence T, Narayanan M, Natarajamani D, Wang S and Knopp M 2015 Characterization of the vereos digital photon counting PET system. Soc Nuclear Med)
- Moliner L, Rodríguez-Alvarez M J, Catret J V, González A, Ilisie V and Benlloch J M 2019 NEMA Performance Evaluation of CareMiBrain dedicated brain PET and Comparison with the whole-body and dedicated brain PET systems *Scientific reports* **9** 15484-10
- Moraes E R, Poon J K, Balakrishnan K, Wang W and Badawi R D 2015 Towards component-based validation of GATE: Aspects of the coincidence processor *Physica Medica* **31** 43-8
- Moses W W 2003 Time of flight in PET revisited *IEEE transactions on nuclear science* **50** 1325-30
- Mullani N, Wong W, Hartz P, Philippe E and Yerian K 1982 Sensitivity Improvement of TOFPET by the Utilization of the Inter-Slice Coincidences *IEEE transactions on nuclear science* **29** 479-83
- Nabulsi N B, Mercier J, Holden D, Carré S, Najafzadeh S, Vandergeten M-C, Lin S-F, Deo A, Price N, Wood M, Lara-Jaime T, Montel F, Laruelle M, Carson R E, Hannestad J and Huang Y 2016 Synthesis and Preclinical Evaluation of ¹¹C-UCB-J as a PET Tracer for Imaging the Synaptic Vesicle Glycoprotein 2A in the Brain *The Journal of nuclear medicine (1978)* **57** 777-84

- Nanni C, Zanoni L, Bach-Gansmo T, Minn H, Willoch F, Bogsrud T V, Edward E P, Savir-Baruch B, Teoh E, Ingram F, Fanti S and Schuster D M 2020 [18 F]Fluciclovine PET/CT: joint EANM and SNMMI procedure guideline for prostate cancer imaging-version 1.0 *European journal of nuclear medicine and molecular imaging* **47** 579-91
- Nassalski A, Kapusta M, Batsch T, Wolski D, Mockel D, Enghardt W and Moszynski M 2007 Comparative Study of Scintillators for PET/CT Detectors *IEEE transactions on nuclear science* **54** 3-10
- Niu G, Lang L, Kiesewetter D O, Ma Y, Sun Z, Guo N, Guo J, Wu C and Chen X 2014 In Vivo Labeling of Serum Albumin for PET *The Journal of nuclear medicine (1978)* **55** 1150-6
- Oliver J F, Torres-Espallardo I, Fontaine R, Ziegler S I and Rafecas M 2008 Comparison of coincidence identification techniques for high resolution PET. *IEEE* pp 4732-5
- Ollinger J M 1996 Model-based scatter correction for fully 3D PET *Physics in medicine & biology* **41** 153-76
- Otte N 2006 The silicon photomultiplier-a new device for high energy physics, astroparticle physics, industrial and medical applications *Proceedings of the IX International Symposium on Detectors for Particle, Astroparticle and Synchrotron Radiation Experiments* 1-9
- Phelps M E 2006 *PET: physics, instrumentation, and scanners* (New York: Springer)
- Poon J K 2013 *The performance limits of long axial field of view PET scanners* (Davis, Calif: University of California, Davis)
- Poon J K, Dahlbom M L, Casey M E, Qi J, Cherry S R and Badawi R D 2015 Validation of the SimSET simulation package for modeling the Siemens Biograph mCT PET scanner *Physics in medicine & biology* **60** N35-N45
- Poon J K, Dahlbom M L, Moses W W, Balakrishnan K, Wang W, Cherry S R and Badawi R D 2012 Optimal whole-body PET scanner configurations for different volumes of LSO scintillator: a simulation study *Physics in medicine & biology* **57** 4077-94
- Rausch I, Ruiz A, Valverde-Pascual I, Cal-González J, Beyer T and Carrio I 2019 Performance Evaluation of the Vereos PET/CT System According to the NEMA NU2-2012 Standard *The Journal of nuclear medicine (1978)* **60** 561-7
- Schmand M, Wienhard K, Casey M E, Eriksson L, Jones W F, Reed J H, Treffert J, Lenox M, Luk P, Bao J, Young J W, Baker K, Miller S D, Knoess C, Vollmar S, Richerzhagen N, Flugge G, Heiss W D and Nutt R 1999 Performance evaluation of a new LSO high resolution research tomograph-HRRT. *IEEE* pp 1067-71 vol.2
- Schroeder B, Lagisetty R and Merchant A 2016 Flash Reliability in Production: The Expected and the Unexpected *14th USENIX Conference on File and Storage Technologies (Fast '16)* 67-80
- Segars W P, Sturgeon G, Mendonca S, Grimes J and Tsui B M W 2010 4D XCAT phantom for multimodality imaging research *Medical physics (Lancaster)* **37** 4902-15
- Shao L and Karp J S 1991 Cross-plane scattering correction-point source deconvolution in PET *IEEE transactions on medical imaging* **10** 234-9

Snyder D L, Thomas L J and Ter-Pogossian M M 1981 A Mathematical Model for Positron-Emission Tomography Systems Having Time-of-Flight Measurements *IEEE transactions on nuclear science* **28** 3575-83

Spencer B A, Berg E, Schmall J P, Omidvari N, Leung E K, Abdelhafez Y G, Tang S, Deng Z, Dong Y, Lv Y, Bao J, Liu W, Li H, Jones T, Badawi R D and Cherry S R 2021 Performance Evaluation of the uEXPLORER Total-Body PET/CT Scanner Based on NEMA NU 2-2018 with Additional Tests to Characterize PET Scanners with a Long Axial Field of View *Journal of Nuclear Medicine* **62** 861-70

Stearns C 1995 Scatter correction method for 3D PET using 2D fitted Gaussian functions *J Nucl Med* **36** 105P

Streun M, Brandenburg G, Larue H, Parl C and Ziemons K 2006 The data acquisition system of ClearPET neuro - a small animal PET scanner *IEEE transactions on nuclear science* **53** 700-3

Strother S C, Casey M E and Hoffman E J 1990 Measuring PET scanner sensitivity: relating countrates to image signal-to-noise ratios using noise equivalents counts *IEEE transactions on nuclear science* **37** 783-8

Strydhorst J and Buvat I 2016 Redesign of the GATE PET coincidence sorter *Physics in medicine & biology* **61** N522-N31

Teräs M, Tolvanen T, Johansson J J, Williams J J and Knuuti J 2007 Performance of the new generation of whole-body PET/CT scanners: Discovery STE and Discovery VCT *European journal of nuclear medicine and molecular imaging* **34** 1683-92

Tries M A, Skrable K W, French C S and Chabot G E 1999 Basic Applications of the Chi-Square Statistic Using Counting Data *Health physics (1958)* **77** 441-54

van Sluis J J, de Jong J R, Schaar J, Noordzij W, van Snick P, Dierckx R, Borra R, Willemsen A and Boellaard R 2019 Performance Characteristics of the Digital Biograph Vision PET/CT System *The Journal of nuclear medicine (1978)* **60** 1031-6

van Velden F H P, Kloet R W, van Berckel B N M, Lammertsma A A and Boellaard R 2009 Accuracy of 3-Dimensional Reconstruction Algorithms for the High-Resolution Research Tomograph *The Journal of nuclear medicine (1978)* **50** 72-80

Vera D B, Schulte B, Henrich T, Flavell R, Seo Y, Abdelhafez Y, Badawi R, Cherry S and VanBrocklin H 2020 First-in-human total-body PET imaging of HIV with 89Zr-VRC01 on the EXPLORER. Soc Nuclear Med)

Wahl R L, Jacene H, Kasamon Y and Lodge M A 2009 From RECIST to PERCIST: Evolving Considerations for PET Response Criteria in Solid Tumors *The Journal of nuclear medicine (1978)* **50** 122S-50S

Walker M D, Asselin M C, Julyan P J, Feldmann M, Talbot P S, Jones T and Matthews J C 2011 Bias in iterative reconstruction of low-statistics PET data: benefits of a resolution model *Physics in medicine & biology* **56** 931-49

Wang G, Parikh M, Nardo L, Zuo Y, Abdelhafez Y, Qi J, Jones T, Price P, Cherry S and Pan C-X 2020 Total-body dynamic PET of metastatic cancer: first patient results. Soc Nuclear Med)

Warburg O, Wind F and Negelein E 1927 The metabolism of tumors in the body *Journal of General Physiology* **8** 519-30

Watson C C 2000 New, faster, image-based scatter correction for 3D PET *IEEE transactions on nuclear science* **47** 1587-94

Watson C C, Casey M E, Bendriem B, Carney J P, Townsend D W, Eberl S, Meikle S and DiFilippo F P 2005 Optimizing Injected Dose in Clinical PET by Accurately Modeling the Counting-Rate Response Functions Specific to Individual Patient Scans *The Journal of nuclear medicine (1978)* **46** 1825-34

Wienhard K, Schmand M, Casey M E, Baker K, Bao J, Eriksson L, Jones W F, Knoess C, Lenox M, Lercher M, Luk P, Michel C, Reed J H, Richerzhagen N, Treffert J, Vollmar S, Young J W, Heiss W D and Nutt R 2002 The ECAT HRRT: performance and first clinical application of the new high resolution research tomograph *IEEE transactions on nuclear science* **49** 104-10

Zaidi H and Montandon M-L 2007 Scatter compensation techniques in PET *PET clinics* **2** 219-34

Zhang J, Lang L, Zhu Z, Li F, Niu G and Chen X 2015 Clinical Translation of an Albumin-Binding PET Radiotracer ⁶⁸Ga-NEB *The Journal of nuclear medicine (1978)* **56** 1609-14

Zhang X, Cherry S R, Xie Z, Shi H, Badawi R D and Qi J 2020a Subsecond total-body imaging using ultrasensitive positron emission tomography *Proceedings of the National Academy of Sciences - PNAS* **117** 2265-7

Zhang X, Xie Z, Berg E, Judenhofer M S, Liu W, Xu T, Ding Y, Lv Y, Dong Y, Deng Z, Tang S, Shi H, Hu P, Chen S, Bao J, Li H, Zhou J, Wang G, Cherry S R, Badawi R D and Qi J 2020b Total-Body Dynamic Reconstruction and Parametric Imaging on the uEXPLORER *The Journal of nuclear medicine (1978)* **61** 285-91